UNIVERSITÀ
DEGLI STUDI
DI PADOVA

Sede Amministrativa: Università degli Studi di Padova

Centro di Ateneo di Studi e Attività Spaziali, CISAS "G. Colombo"

CORSO DI DOTTORATO DI RICERCA IN: Scienze Tecnologie e Misure Spaziali

CURRICULUM: Scienze e Tecnologie per Applicazioni Satellitari ed Aeronautiche

CICLO: XXXI

NUMERICAL AND EXPERIMENTAL INVESTIGATION INTO THE PERFORMANCE OF PLASMA-BASED THRUSTER FOR SPACE PROPULSION

Coordinatore: Ch.mo Prof. Giampiero Naletto

Supervisore: Dr. Davide Melazzi

Co-supervisore: Ch.mo Prof. Daniele Pavarin

Dottorando: Mirko Magarotto

Contents

Abstract

A Helicon Plasma Thruster is an electric propulsion system in which the thrust is attained accelerating the plasma produced in a Helicon source with a magnetic nozzle. The main components of a Helicon Plasma Thruster are (i) a dielectric tube inside which the plasma is produced from a neutral gas propellant, (ii) a radio frequency antenna working in the MHz range which drives the discharge, and (iii) magnets which generate a magneto-static field (up to 0.2 T) for plasma confinement and acceleration. The principal features which make Helicon Plasma Thrusters appealing for space applications are the simple geometry and in turn the relatively low cost, the long life due to the absence of grids or electrodes in contact with the plasma, and no need for a neutraliser being the ejected beam globally neutral. The propulsive performances (e.g., thrust and specific impulse) of Helicon Plasma Thrusters are strictly related to both the plasma generation and the plasma acceleration mechanisms, therefore a numerical tool capable of resolving both the Helicon source and the plume has been implemented. Specifically, the 3D-VIRTUS code has been developed to solve self-consistently the plasma transport and the wave propagation inside the source, while an analytical model of the plume has been adopted to obtain preliminary estimations of the propulsive performances. In particular, 3D-VIRTUS can handle sources of arbitrary three-dimensional geometries, driven by an arbitrary-shaped conductive antenna, and magnetized by coils or permanent magnets. Moreover, 3D-VIRTUS has been verified against both numerical and experimental benchmarks. The new code has been exploited in a parametric analysis conducted on a simplified configuration of Helicon Plasma Thruster. The parameters of the system (e.g., initial neutral density, along with intensity and topology of the magneto-static field) and the geometry (e.g., discharge radius and length, along with antenna shape) have been varied in typical operational ranges in order to assess their influence on (i) the equilibrium plasma profiles (e.g., plasma density and electron temperature), (ii) the electrical response of the discharge (e.g., antenna impedance), and (iii) the preliminary estimations of the propulsive performances. Moreover, a counterbalanced pendulum thrust stand specifically conceived for testing Helicon Plasma Thrusters has been characterised and exploited. The stand can handle prototypes producing thrust from tens of μNewton up to tens of milliNewton, operated with an electrical power lower than 1 kW, and whose weight envelope (i.e., thruster integrated with other subsystems such as the PPU) is up to 10 kg. Tens of measurements per day can be accomplished with a 2-σ uncertainty in the order of 15%. Preliminary tests have been conducted in order to characterise of the mechanical response of the stand (e.g., sensibility, linearity range and noise), and to develop a correction procedure for the zero-position drift. Subsequently the thrust stand has been exploited to test a medium power (200-300 W)

Helicon Plasma Thruster operated with xenon and carbon dioxide propellants. Finally, a combined numerical-experimental campaign has been conducted on a low power (50 W) prototype operated with argon propellant in order to verify the reliability of the numerical model when handling a real-life thruster.

Abstract Italiano

Un Helicon Plasma Thruster è un propulsore elettrico in cui la spinta è ottenuta accelerando, attraverso un ugello magnetico, il plasma prodotto in una sorgente Helicon. I componenti principali di un Helicon Plasma Thruster sono (i) un condotto in materiale dielettrico all'interno del quale il plasma viene prodotto a partire da un propellente gassoso, (ii) un'antenna eccitata in radio frequenza (alcuni MHz) che sostiene la scarica, e (iii) magneti che generano un campo magnetostatico, di intensità solitamente inferiore a 0.2 T, il quale viene impiegato sia per migliorare il confinamento del plasma che per favorirne l'accelerazione. La tecnologia Helicon risulta particolarmente adatta ad applicazioni spazio, infatti propulsori di questo tipo hanno una geometria molto semplice e quindi sono relativamente poco costosi, hanno una vita operativa molto lunga perché non ci sono griglie o elettrodi a contatto con il plasma, e non servono neutralizzatori perché il flusso di particelle eiettato è globalmente neutro. Dato che le prestazioni di un Helicon Plasma Thruster (spinta ed impulso specifico) sono intimamente legate a come il plasma è prodotto ed accelerato, si è ritenuto opportuno sviluppare un codice numerico in grado di simulare sia la sorgente Helicon che il fascio di plasma (chiamato plume). Nello specifico, il codice 3D-VIRTUS è stato sviluppato per risolvere l'accoppiamento fra la propagazione di onde elettromagnetiche ed il trasporto di plasma nella sorgente, mentre un modello analitico è stato adottato per simulare il plume e quindi ottenere una stima preliminare delle prestazioni. In particolare con 3D-VIRTUS si possono simulare sorgenti di forma generica, sostenute da antenne di geometria qualsiasi, e circondate da campi magnetostatici generati sia da elettromagneti che da magneti permanenti. Inoltre, 3D-VIRTUS è stato verificato sia contro altri modelli numerici che contro misure sperimentali. Il nuovo codice è stato quindi impiegato per l'analisi di una configurazione semplificata di Helicon Plasma Thruster. I parametri del sistema (cioè densità iniziale dei neutri, intensità e topologia del campo magnetostatico) e la geometria (cioè diametro e lunghezza della scarica, forma dell'antenna) sono stati analizzati in un intervallo tipico per un'applicazione spazio, in particolare si è valutato il loro impatto su (i) profili di plasma all'equilibrio all'interno della sorgente (cioè densità e temperatura), (ii) comportamento elettrico della scarica (cioè impedenza dell'antenna), e (iii) stime preliminari delle prestazioni del motore. In aggiunta, una bilancia di spinta di tipo counterbalanced pendulum, progettata per testare Helicon Plamsa Thruster, è stata caratterizzata ed utilizzata. La bilancia può lavorare con prototipi che producono una spinta fra le decine di μN e le decine di mN, alimentati da una potenza inferiore a 1 kW, ed il cui inviluppo di massa (cioè motore più eventuali sottosistemi come una PPU) sia inferiore a 10 kg. Si possono effettuare decine di misure al giorno con un'incertezza di 2-σ nell'ordine del 15%. Alcuni test preliminari sono

stati condotti per caratterizzare la risposta meccanica della bilancia (cioè sensibilità, intervallo di linearità, e rumore), e per elaborare una procedura per correggere lo zero-position drift. Successivamente la bilancia di spinta è stata utilizzata per valutare le prestazioni di un Helicon Plasma Thruster di media taglia (200-300 W) fatto lavorare con xeno ed anidride carbonica. In fine, una campagna numerico-sperimentale è stata condotta su di un prototipo di taglia piccola (50 W) alimentato ad argon per verificare l'attendibilità delle simulazioni effettuate su motori reali.

Acknowledgements

I would like to thank everyone who supported me during this PhD programme, above all my supervisor Davide, and prof. Daniele, without whom this work would not have been possible. I am also grateful to all the guys from the lab, Marco, Fabio, and Paola: their help, and advice were precious, and valuable. A special thanks is due to my family, and Elena, who have always been there for me.

List of Symbols

T	Thrust	[N]
I_{sp}	Specific Impulse	[s]
Pw	Electrical Power	[W]
η	Efficiency of Thrust Power Conversion	[#]
m_P	Mass of the Power Supply	[kg]
α_P	Proportionality Constant	[kg W^{-1}]
n_e	Electrons Number Density	[m^{-3}]
$\mathbf{\Gamma}_e$	Electrons Flux	[$m^{-2}s^{-1}$]
R_e	Electrons Production/Loss Term	[$m^{-3}s^{-1}$]
n_i	Ions Number Density	[m^{-3}]
$\mathbf{\Gamma}_i$	Ions Flux	[$m^{-2}s^{-1}$]
R_i	Ions Production/Loss Term	[$m^{-3}s^{-1}$]
n_0	Neutrals Number Density	[m^{-3}]
$\mathbf{\Gamma}_0$	Neutrals Flux	[$m^{-2}s^{-1}$]
R_0	Neutrals Production/Loss Term	[$m^{-3}s^{-1}$]
n_s	Excited Number Density	[m^{-3}]
$\mathbf{\Gamma}_s$	Excited Flux	[$m^{-2}s^{-1}$]
R_s	Excited Production/Loss Term	[$m^{-3}s^{-1}$]
ε_n	Electron Energy Density	[Vm^{-3}]
$\mathbf{\Gamma}_\varepsilon$	Electron Energy Flux	[$Vm^{-2}s^{-1}$]
R_ε	Electron Energy Production/Loss Term	[$Vm^{-3}s^{-1}$]
T_e	Electron Temperature	[V]
$\mathbf{E}_{DC}$	Electrostatic Field for Charge Imbalance	[Vm^{-1}]
ϕ	Plasma Potential	[V]
q	Elementary Charge	[C]
ε_0	Vacuum Permittivity	[Fm^{-1}]
μ_k	Mobility of the k-th Species	[$m^2s^{-1}V^{-1}$]
D_k	Diffusivity of the k-th Species	[m^2s^{-1}]
μ_ε	Electron Energy Mobility	[$m^2s^{-1}V^{-1}$]
D_ε	Electron Energy Diffusivity	[m^2s^{-1}]
$\mathcal{E}_{chem}$	Reactions Production/Loss Term	[$Vm^{-3}s^{-1}$]
$\mathcal{E}_{pow}$	RF Power Deposited into the Discharge	[$Vm^{-3}s^{-1}$]
k_{el}	Elastic Scattering Reaction Rate	[m^3s^{-1}]
k_{iz}	Neutrals Ionization Reaction Rate	[m^3s^{-1}]
k_{ex}	Excitation Reaction Rate	[m^3s^{-1}]

k_{siz}	Excited Ionization Reaction Rate	$[m^3s^{-1}]$
$\mathcal{E}_{el}$	Elastic Scattering Production/Loss	$[Vm^{-3}s^{-1}]$
$\mathcal{E}_{iz}$	Neutrals Ionization Production/Loss	$[Vm^{-3}s^{-1}]$
$\mathcal{E}_{ex}$	Excitation Production/Loss	$[Vm^{-3}s^{-1}]$
$\mathcal{E}_{siz}$	Excited Ionization Production/Loss	$[Vm^{-3}s^{-1}]$
m	Electrons Mass	[kg]
M	Heavy Species Mass	[kg]
Δ_{iz}	First Ionization Energy	[V]
Δ_{ex}	Excitation Energy	[V]
Δ_{siz}	Energy for Ionizing an Excited	[V]
$\mathbf{B}_0$	Magneto-static field	[T]
$\tilde{\mu_e}$	Scalar Electron Mobility	$[m^2s^{-1}V^{-1}]$
k_B	Boltzmann constant	$[J\ K^{-1}]$
T_0	Heavy species temperature	[K]
σ_D	Cross Section parameter	[m]
Ω_D	Collision Integral	[#]
$\hat{\mathbf{k}}$	Unit Vector at the Boundary	[#]
$\Gamma_\perp$	Particles Flux at the Boundary	$[m^{-2}s^{-1}]$
$v_{th,0}$	Heavy Particles Thermal Speed	$[m\ s^{-1}]$
Δt	Time Step	[s]
$\epsilon_{F,max}$	Relative Error of the Fluid Model	[#]
R	Discharge Radius	[m]
L	Discharge Length	[m]
r	Radial Coordinate	[m]
z	Axial Coordinate	[m]
$\mathcal{E}^0_{pow}$	Scale Power Deposition	$[Wm^{-3}]$
N_r	Number of Radial Nodes	[#]
N_z	Number of Axial Nodes	[#]
Δt_{max}	Maximum Time Step	[s]
$\mathbf{D}_\mathrm{p}$	Electric Flux Density	$[Cm^{-2}]$
$\mathbf{J}_\mathrm{p}$	Plasma Polarization Current	$[Am^{-2}]$
ϵ_{max}	Relative Error of the Iteration Loop	[#]
F_0	Upstream Plasma Thrust	[N]
F_{mag}	Thrust due to Magnetic Nozzle Acceleration	[N]
$\mathcal{M}$	Magnetic Mach Number	[N]
F_p	Thrust Provided by the Plasma	[N]
$\mathcal{M}_{det}$	Magnetic Mach Number at the Detachment	[N]
F_{gas}	Thrust Provided by the Neutral Gas	[N]
v_g	Speed of Sound	$[m\ s^{-1}]$
Z	Antenna Impedance	[Ω]
R_A	Antenna Radius	[m]
w	Antenna Width	[m]
L_A	Antenna Length	[m]
f	Excitation Frequency	[Hz]
K	Pivot Torsional Stiffness	$[Nm\ rad^{-1}]$

m_t	Thruster Mass	[kg]
b_t	Thruster Arm	[m]
m_c	Counterweights Mass	[kg]
b_c	Counterweights Arm	[m]
g_0	Gravitational Acceleration at Sea Level	[m s^{-2}]
α	Rotational Angle of the Pendulum Arm	[rad]
m_r	Pendulum Arm Mass	[kg]
b_r	Position of the Pendulum Arm Baricenter	[m]
Δ_x	Displacement of the Pendulum Arm	[m]
R_T	Sensibility of the Thrust Stand	[m N^{-1}]
m_m	Calibration Mass	[kg]
b_m	Calibration Mass Arm	[m]
T_{eq}	Equivalent Calibration Thrust	[m]
I	Calibration Current	[A]
R_I	Current Displacement Ratio	[m A^{-1}]
m_{red}	Reduced Mass of the Thrust Stand	[kg]
Δ_{max}	Maximum Displacement	[m]
T_{max}	Maximum Thrust for Linearity	[N]
σ	Standard Deviation of the Displacement	[m]
T_σ	Sensitivity of the Thrust Stand	[N]
Δ_{eq}	Corrected Displacement	[m]
T_{FP}	Thrust Measured by the Faraday Probe	[N]
T_s	Thrust Measured by the Thrust Stand	[N]
ε_{rel}	Difference on the Thrust Measurements	[%]
$\dot{m}_0$	Propellant Mass Flow Rate	[kg s^{-1}]

List of Acronyms

EM	Electro-Magnetic
HPT	Helicon PLasma Thruster
RF	Radio Frequency
ICP	Inductively Coupled Plasma
CCP	Capacitively Coupled Plasma
TG	Trivelpiece-Gould
PIC	Particel In Cell
MCC	Monte Carlo Collisons
1D	one-dimensional
2D	two-dimensional
3D	three-dimensional
PPT	Pulsed Plasma Thruster
3D-VIRTUS	3-Dimensional adVanced fluId dRifT diffUsion plaSma
Ar	neutral argon
Ar^*	excited argon
Ar^+	ionized argon
e	electron
FV	Finite Volume
PEC	Perfectly Electric Conductor
PPU	Power Processing Unit
PCU	Power Control Unit
IR	Infrared Radiation
Xe	xenon
CO_2	carbon dioxide
hBN	hexagonal Boron Nitride
SmCo	Samarium Cobalt

List of Figures

List of Tables

Chapter 1

Introduction

From the beginning of the Space Age (i.e., '50s), electric thrusters for the propulsion of spacecrafts have been studied and developed due to their high specific impulse (up to 10000 s [1]) and, in turn, efficient utilization of propellant mass. The reduction of propellant to be embarked in a spacecraft allows for both increasing the amount of useful payload, accomplishing missions otherwise unaffordable with chemical rockets, and reducing the mission's costs.

In conventional chemical rockets, thrust is obtained heating a working fluid by means of a dedicated chemical reaction (usually combustion but also decomposition [2]) and than expanding this very fluid through a nozzle. Therefore, in a chemical rocket the main constraints which limit the velocity of the exhaust fluid, and in turn the specific impulse, are:

- the maximum amount of heat that can be provided to the fluid without damaging the walls of the combustion chamber and of the nozzle
- the energy that the chemical reaction can provide

In electric thrusters these limitations does not hold true because:

- the working fluid is constrained away from the thruster's solid walls by electric means (e.g., magnetostatic fields [1, Chap. 5])
- the upper values of specific impulses attainable with electric propulsion (up to 10000 s), are obtained accelerating the working fluid with the aid of Electro-Magnetic (EM) body-forces (e.g., Lorentz force [1, Chap. 8.1])

In literature, electric propulsion concepts have often been divided into three categories depending on the means in which the working fluid is accelerated: (i) *electrothermal propulsion*, if the propellant is heated with electric means and then accelerated with a nozzle; (ii) *electrostatic propulsion*, if an electric body-force is applied for accelerating and ionizing particles; (iii) *electromagnetic propulsion*, if an ionized propellant stream is accelerated by means of the interaction of magnetic fields and currents (the former can be both internal or external to the stream [1, Chap. 8.1]). Table 1.1 provides the typical performances (thrust T and specific impulse I_{sp}) of the most diffused electric, and chemical, thruster concepts.

Propulsion concept	T [N]	I_{sp} [s]
Electric		
Electrothermal	10^{-3} - 10	
- Resistojet		≤ 500
- Arcjet		≤ 1000
Electrostatic	10^{-6} - 1	
- Ion		200 - 10000
- Hall effect		300 - 6000
- FEEP		≤ 10000
Electromagnetic	10^{-6} - 1	
- Magnetoplasmadynamic		2000 - 5000
- PPT		1000
- Cathodeless		≤ 2000
Chemical		
Liquid monopropellant	10^{-1} - 10^{3}	≤ 300
Liquid bipropellant	1 - 10^{6}	≤ 450
Solid	10^{2} - 10^{7}	≤ 350

Table 1.1: Summary of the performances (thrust T and specific impulse I_{sp}) of the most diffused electrical and chemical thruster concepts [1, 3, 4, 5].

Clearly, in order to provide electric heating or EM body-forces, electric thrusters require dedicated power supplies. The amount of electrical power Pw required for achieving certain thruster performances (i.e., thrust T and a specific impulse I_{sp}) is given by

$$Pw = \frac{1}{2}\eta T I_{sp} \tag{1.1}$$

where η is the efficiency of thrust power conversion. The mass of the power supply m_P depends principally on Pw, therefore it can be assumed that

$$m_P = \alpha_P \; Pw \tag{1.2}$$

where α_P is a proportionality constant. Combining Eq. 1.1 and Eq. 1.2 it can be easily shown that [1, Chap. 1.4]:

- for a certain mission profile, increasing I_{sp} above a certain threshold value is no more convenient in terms of the total spacecraft mass, because the increase of the power supplies mass m_P overcomes the saving up of propellant mass
- for a certain amount of electrical power Pw available, increasing I_{sp} results in a reduction of T

Therefore, due to the m_p constraint: (i) the thruster with the highest specific impulse is not always the most suited for a certain mission scenario; (ii) as shown in Table 1.1, electric thrusters are usually characterized by higher specific impulses than chemical rockets but also by significantly lower thrust attainable. Moreover, an electric propulsion system is in general more complex than a chemical one because extra components are required. Typically, the power is supplied to the thruster by means of a Power Processing Unit (PPU) which processes the DC electric power provided from the satellite into the specific form required by the thruster (e.g., increasing the voltage or DC/AC conversion). In order to guarantee a high electrical efficiency and a reduced mass and volume, the PPU is usually one of the most complex and challenging components of an electric propulsion system [4]. At the same time, a fluidic line is in general required to provide the propellant to the thruster. Even though the latter is not much more complex than for a mono-propellant or a cold gas thruster, the flows to be handled are usually very small and occur for very prolonged periods of time (months), therefore special challenges arise for the design of precise flow controllers and leak-free valving [4]. Therefore, the main disadvantages of an electric thruster in respect to a chemical one are:

- a lower thrust attainable due to the limited power available on a satellite (i.e., the m_p constraint)
- the more complex and expensive process required to integrate the thruster into a satellite

Because of the substantial differences between chemical and electric thrusters, the mission scenarios in which two typologies of space propulsion concepts can be applied are significantly different

- Electric propulsion is particularly suited for interplanetary orbit transfers or station keeping corrections, where the required high total impulses can be provided with low-thrust and long-time manoeuvres
- Chemical propulsion instead is the only option now available for launchers which require very high thrusts (up to tens of mega-Newton) in order to overcome the Earth's gravity force

A fairly complete list of space missions employing electric thruster can be found in [6]; it can be easily noted that the most widely employed electric propulsion concepts are Ion and Hall-effect thrusters [7].

1.1 Helicon Plasma Thruster

The research activity in the electric propulsion field is today very active even though mature technologies as Ion and Hall-effect thrusters have been employed in space missions for years [8]. In the last decade, particular effort has been paid in the development and study of a new concept of plasma-based propulsion system called Helicon Plasma Thruster (HPT) [9]. A HPT is composed of a Helicon plasma source at its core for the plasma generation [10], and a magnetic nozzle which accelerates the exhaust stream and,

ultimately, produce thrust [11]. A schematic of a HPT has been reported in Fig. 1.1, that encompasses:

- the dielectric tube inside which the neutral gas is ionized
- the Radio Frequency (RF) antenna that works in the MHz range, and produces the EM fields for plasma generation and heating
- the magnets (permanent or electromagnets) that generate a magneto-static field with divergent field lines in the magnetic nozzle region

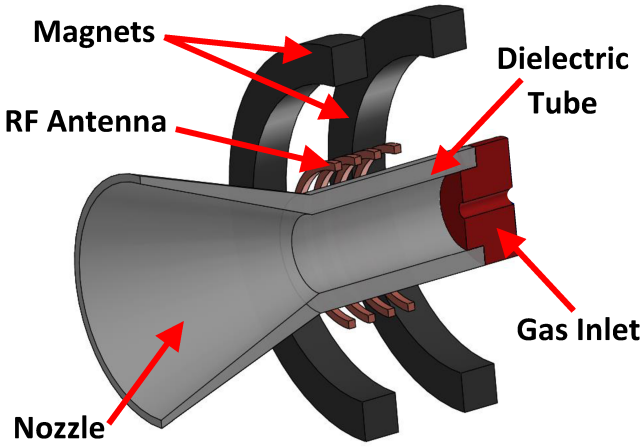

Figure 1.1: Schematic of a HPT.

The purpose of the magneto-static field is three-fold: (i) to enhance the plasma confinement, (ii) to allow for the propagation of whistler waves [12, 13] within the source, and (iii) to provide the magnetic nozzle effect that guides, expands and accelerates a plasma jet into vacuum.

HPTs present a number of interesting features, namely:

- a very simple structure and, in turn, a low cost
- absence of electrodes immersed in the plasma, with consequently limited erosion and long life
- no need for a neutralizer [7, Chap. 6] because the ejected stream is a globally neutral plasma and not an ion beam
- good power scalability [14, 15]
- good adaptability to different propellants without geometric reconfiguration [15]

HPTs have been studied, and developed in many international projects by both research centres and companies. At Astra Rocket Company has been involved in the VASIMR project, which aims at the development of an high-power (200 kW) HPT for

Institution	Pw [W]	T [mN]	Propellant	$L \times \Phi$ [mm]
Ad Astra	$\approx 2 \times 10^5$	$\approx 10^3$	H/Ar/Kr	1000×100
ANU	≤ 900	$1 - 3$	Ar	300×10
UNIPD	≤ 50		Ar	200×40
T4i	≈ 50	≤ 1	Xe	100×20
UC3M	$\leq 10^3$		Ar/Xe	200×30
Todai	$\leq 3 \times 10^3$	≤ 6	Ar	1000×100
Tohokudai	$800 - 6000$	$10 - 60$	Ar	200×100
MIT	$\approx 10^3$	≈ 10	Ar/N_2	200×40
UMich	≤ 200		Xe	
UW	$\leq 5 \times 10^4$		Ar	200×20

Table 1.2: Summary of the performances of the most relevant HPTs found in literature: institution which developed the HPT under consideration, input power Pw, produced thrust T (reported only if measured directly), propellant gas adopted, rough estimation of the discharge chamber envelope (length L × diameter Φ).

interplanetary missions [16, 17]. In 2003, the Double Layer phenomena has been investigated at the Australian National University (ANU) as the principal acceleration mechanism of HPTs [18]; more recently [19, 20] medium power (up to 1 kW) HPTs have been developed and tested at the same institution. At the University of Padova (UNIPD), a 50 W HPT has been designed, developed, and tested during the HPH.COM project [9], a 1 kW thruster is under development in the frame of the SAPERE-STRONG project [14], while a propulsion platform for CubeSats [15] is currently in progress in collaboration with Technology for Propulsion and Innovation Srl (T4i) [21], a spin-off of the above-mentioned university. At the Carlo III University of Madrid (UC3M) a medium power (up to 1 kW) has been developed and characterized with the collaboration of the European Space Agency (ESA) and the Sener company [22]. An additional acceleration mechanism based on polarized electrodes have been investigated at the Tokyo University (Todai) in order to enhance the performances of medium-high power (up to 3 kW) HPTs [23, 24]. At the Tohoku University (Tohokudai) a deep experimental investigation on medium up

to high power (up to 6 kW) HPTs has been undertook in order to optimize the geometry of the plasma discharge [25]. At the Massachusetts Institute of Technology (MIT) [26] a medium power (1 kW) HPT relying on a very simple magnetic configuration (a single electro-magnet) has show a significant capability of varying the specific impulse (namely from 1000 s up to 4000 s) modifying the propellant mass flow rate and the antenna input power. Recently, a HPT devoted to the CubeSat application (up to 200 W of input power) is under development at the Michigan Institute of Technology (UMich) [27]. Finally, at the Washington University (UW) [28] relatively small prototypes (discharge chamber with length and diameter of some centimetres) have been operated with high powers (up to 50 kW) in order to achieve very high specific impulses, namely up to 5000 s.

1.1.1 Helicon plasma source

We mention in passing that the key aspect of the HPT is the Helicon plasma source. The principal components of a Helicon source are a dielectric tube, magnets which produce a moderate quasi-axial magneto-static field (up to 0.20 T), and an RF antenna working in the MHz regime (see Fig. 1.2). Compared to Inductively Coupled Plasma (ICP) and Capacitively Coupled Plasma (CCP) [29], Helicon sources are characterized by a very efficient plasma production: high plasma densities ($\geq 10^{19}$ m^{-3}) can be reached with simple antenna geometry (e.g. single loop, helix, and Nagoya Type-III [30]) and moderate RF power [10]. The first experiments on Helicon sources date back to '60s when Lehane and Thonemann [31] measured EM waves propagating in a cylindrical source at about 15 MHz: a very low frequency rage for the waves known to propagate in plasma at that time. Since 80's, Helicon discharges have become a very intense field of research, both from a theoretical and a technological standpoint, in particular thanks to the contributions of Chen and Boswell [10, 32, 33]. The applications in which Helicon sources have been principally employed are: enhanced plasma processing [34], material surface modification [35], semiconductor manufacturing processes [36], and space propulsion.

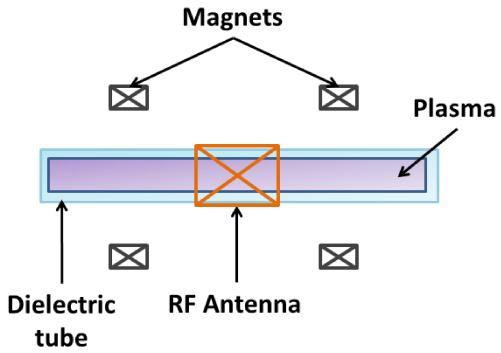

Figure 1.2: Schematic of a Helicon plasma source.

1.2 Prediction of HPT performances

In order to optimize the propulsive figures of merit (e.g. specific impulse, thrust/mass ratio, and efficiency) of a HPT, a deep physical insight has to be gained into both the plasma generation and plasma acceleration mechanisms.

1.2.1 Phenomena governing the HPT dynamics

The dense plasma ($\geq 10^{19}$ m^{-3}) production is governed by the propagation of whistler waves in the discharge region (identified as *Production Stage* in Fig. 1.3). In general, in a uniform Helicon source, the dispersion relation can present two branches which describe the propagation of a faster and a lower wave; the former has been classically referred as Helicon wave and the latter as Trivelpiece-Gould (TG) [12]. Specifically, the power deposition phenomena comes from the dumping of such waves by means of collisional processes and Landau damping [37, Chap. 7.4]. In particular, due to the motion of charged particles and the diffusion processes that contribute to the achievement of a stable discharge, the density production in Helicon sources is non-uniform [38]. The resulting density gradient greatly modifies the wave structure so that non uniform plasma profiles can induce cut-offs at certain radial positions of the cylindrical Helicon source [39]. Moreover, if also the non-uniformity of the actual magneto-static field is accounted, cut-offs, resonances, radial reflections and mode conversions of the excited waves might arise. In turn, the latter can result in power deposition profiles peaked in the central core region of the discharge rather than at the edge as expected in ICPs [29]. Therefore, the key physical phenomena that govern the Helicon source are the EM wave propagation, the plasma transport, and their mutual coupling.

The acceleration and detachment phenomena take place principally downstream the Helicon source (identified as *Acceleration Stage* in Fig. 1.3). The *Acceleration Stage* is characterized by the formation of a plume where the plasma is more rarefied than in the *Production Stage* (density in the range 10^{16} – 10^{18} m^{-3}) [40]. The plume can be divided into two separate regions, respectively near region and far region, depending on the phenomena which govern the plasma dynamics [41]. In the near region, particle collisions and the geometry of the applied magneto-static field drive the plasma behaviour. Instead in the far region, the expansion of the plasma is mainly governed by the thermal pressure, and the ambipolar diffusion.

1.2.2 Theoretical and numerical approaches

Provided the complexity and the variety of the phenomena involved in the dynamics of a HPT, several theoretical and numerical strategies have been adopted to predict the performances of such a thruster. Three analytical models have been developed respectively by Lafleur [42], Ahedo [43], and Fruchtmann [44]. These very tools are particularly useful in the preliminary design of the thruster, when a quick estimation of the performances (e.g., thrust and specific impulse), and of the plasma properties inside the source (e.g., plasma density and electron temperature) is required. Nonetheless, for the optimization of the thruster more advanced numerical instruments must be adopted.

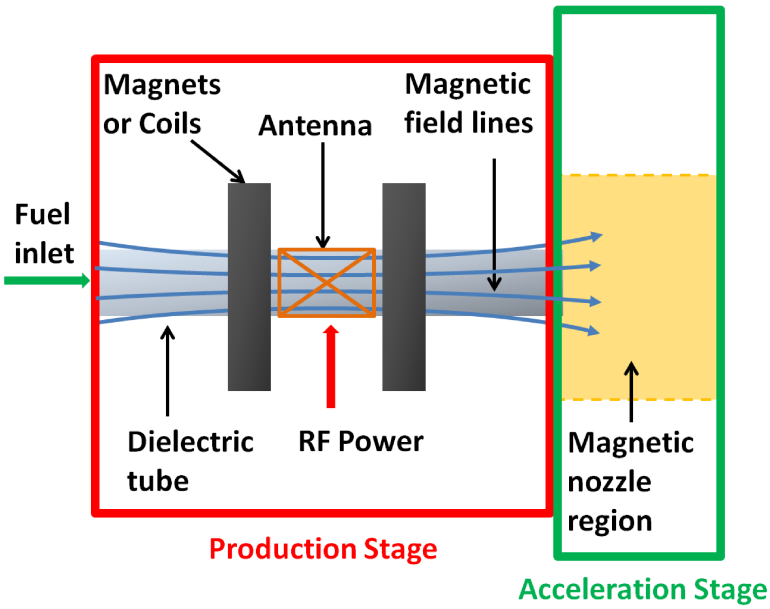

Figure 1.3: Schematic of a HPT which highlights the separation between *Production Stage* and *Acceleration Stage*.

Several numerical approaches have been pursued in literature for modelling both the *Production Stage* and the *Acceleration Stage*; the most relevant are: fluid, kinetic, Particle-In-Cell with Monte-Carlo Collisions (PIC-MCC), and hybrid. First, the fluid approach assumes the particle distribution function, and describes the plasma in terms of continuity, momentum, and energy equations [45]; this method is less demanding in terms of computational resources than the other approaches, and thus has been widely employed [46]. Clearly, the fluid approach fails if the particle distribution function departs significantly from Maxwellian, as it can happen in rarefied and weakly collisional plasmas [40]. Second, the kinetic model is based on the solution of Maxwell equations together with the integro-differential Boltzmann equation [45], and allows determining uniquely the self-consistent particle distribution function. From the knowledge of the latter, particle density, mean velocity, and other macroscopic quantities are determined by averaging the distribution function. Since it is complex and extremely computationally demanding, this approach has been mostly applied under simplifying hypotheses, e.g. mono-dimensional simulations [47, 48]. Third, the PIC-MCC approach integrates in time the trajectory of computational particles (i.e. a cloud of physical charged particles) under the effect of EM fields [49], and thus it is capable of accurately describing also non-local effects, and non-equilibrium situations. Though very accurate, this method is computationally intensive, and this is especially true for high density plasmas ($\geq 10^{19}$ m^{-3}); even with good parallelisation, a PIC-MCC code could require weeks or months to simulate a plasma thruster [40]. Lastly, to preserve the accuracy of kinetic and PIC-MCC simulations, while reducing the computational burden, the afore-mentioned approaches have been combined in hybrid solvers [40, 47, 50]; however, the resulting algorithms can be quite cumbersome.

For what concerns the simulation of the *Production Stage*, despite the huge amount of codes that solves for the EM wave propagation [39, 51, 52, 53, 54, 55], there are few examples of numerical models that solve self-consistently the Helicon discharge by accounting for both the power deposition, and the transport phenomena. In this regard, a one-dimensional (1D) radial fluid model [56] has been adopted to study cylindrical Helicon sources; the main limitation of this formulation relies on the assumption of semi-empirical relations to estimate the plasma profiles along the axis of the discharge. A much more accurate two-dimensional (2D) axisymmetric model of a Helicon material processing reactor has been solved by means of both fluid, and hybrid approaches [57, 58]. In the latter the electron distribution function has been calculated with a PIC-MCC strategy, and then exploited for the evaluation of the transport coefficients in the fluid equations. The power deposited by the TG wave has been neglected both in the fluid and hybrid model. Similarly, a 2D-axisymmetric fluid model has been exploited to simulate a Helicon reactor for plasma etching[59]. A cylindrical Helicon source has been studied with an hybrid code where the PIC-MCC approach for ion simulation has been coupled to a fluid formulation of electrons motion [50]. Though only ions have been solved by PIC-MCC, and the geometry is 2D-axisimmetric, the computational cost of this approach can be considerably high for plasma density values higher than $\geq 10^{19}$ m^{-3}.

Finally, if the analysis of the *Acceleration Stage* is considered both fluid [11], kinetic [48], PIC-MCC [60], and hybrid [61] approaches have been followed. Nonetheless, particular care must be adopted if fluid or hybrid codes are employed because, in the plume, the particles distribution function can significantly depart from Maxwellian [60], in particular if double layer arises [62, 63]. In conclusion, it is worth recalling that if two different simulation strategies are adopted to simulate the *Production Stage* and the *Acceleration Stage*, the boundary conditions at the source outlet and at the plume inlet must be chosen carefully in order to avoid mismatching between the two solvers [43].

1.3 Measurement of HPT performances

In order to verify the actual performances of a HPT prototype, and to validate the predictions of theoretical and numerical tools, reliable and accurate measurements of the thrust are needed.

In literature, different methods has been pursued to measure the force produced by an electric thruster; the two most widely used rely on electrostatic probes and thrust stands respectively. In the first method, a Faraday cup [64] and a retarding potential analyser [65] are employed for measuring the flux of ions ejected from the thruster and the ion energy distribution in the plume; from these data, thrust and specific impulse can be deduced [66]. This method, even if simple to implement, leads to not very accurate results, in particular if dealing with RF based plasma systems [67] (the error can be between 30-40%). The other method is based on the measurement of mechanical displacements produced on a sensitive thrust stand or a pendulum, on which the thruster is fastened. This second method is more reliable but even the simplest concepts of thrust stand (e.g. simple pendulum configuration [68]) require bulky hardware inside the vacuum chamber and several expedients to reduce mechanical vibrations and interferences. The most commonly

employed thrust stand concepts are:

- Conventional hanging pendulum [69, 70], which is the simplest solution but could be some meters tall if designed to detect micro-Newton level forces, or involves original mechanisms for motion amplification [71]
- Double pendulum [20, 72] which has similar features of the conventional hanging pendulum but is particularly robust against disturbances.
- Inverted pendulum [73, 74, 75], which can be very accurate depending on the feedback control employed, but can hardly be adjusted to cover a wide range of thrust and weight due to its intrinsic instability.
- Torsional pendulum [76, 77, 78, 79], which allows for an accurate thrust measurement but the horizontal axisymmetric arrangement can be difficult to configure.
- Null-displacement systems, involving a feedback control loop [80, 81], which allows for accurate measurements but may be prone to RF disturbance effects.

Other thrust stand concepts have been adopted in order to meet specific requirements, e.g. measuring thrust in the nano-Newton range [82] or in the tens of Newton range [83], measuring the thrust in two directions [84], measuring the performances of hollow cathodes [85] or Pulsed Plasma Thrusters (PPTs) [86]. Different stand concepts can be adopted in order to measure a wide range of thrust: at the ESA propulsion lab of ESTEC [87] motors which produce thrust from 1 μN up to 20 N can be tested relying on inverted pendulum, load cells, and null-force pendulum.

1.4 Outline

This work is devoted to the presentation and discussion of:

- a numerical model for the optimization of the discharge chamber of a HPT which relies on: (i) the 3-Dimensional adVanced fluId dRifT diffUsion plaSma solver (3D-VIRTUS) [88] for the simulation of the *Production Stage*, and (ii) an analytical model of the plume [42] for the solution of the *Acceleration Stage*, and in turn for the preliminary estimation of the propulsive performances (i.e., thrust and specific impulse)
- the characterization and exploitation of a counterbalanced pendulum thrust stand [89] specifically developed for measuring the force generated by HPTs

The numerical model solves the two stages of the thruster in separate steps: (i) first the *Production Stage* is solved, (ii) second the *Acceleration Stage* is simulated with a simplified plume model which takes in input the plasma parameters (e.g., plasma density and electron temperature) calculated in the previous step. The 3D-VIRTUS code [88] has been employed for the solution of the *Production Stage*, and a quasi one-dimensional analytical plume model [42] has been adopted for the *Acceleration Stage*, and in turn the preliminary estimation of the propulsive performances. In particular, the 3D-VIRTUS code has been

developed to solve self-consistently Helicon plasma sources; namely to simulate the mutual coupling between the EM wave propagation into the discharge, and the macroscopic plasma transport. To this end, the two problems are treated by two distinct modules, that have been iteratively run up to the convergence. The first problem has been solved with the well-established numerical tool ADAMANT [53], while for the second problem, a fluid model has been implemented in OpenFOAM [90]; the latter can be easily reconfigured to treat either 1D, or 2D, or 3D problems depending on the specific analysis. It is worth recalling that in literature, among the few codes which solve self-consistently Helicon sources (i.e., both the EM wave propagation and the plasma transport) [50, 56, 57, 58, 59], no other numerical tool has been found which can (i) treat discharges with a generic 3D geometry, and (ii) model the actual RF antenna, solving the current distribution thereof. As a result, it is possible to accurately simulate the *Production Stage* of a HPT that has arbitrary geometry, is driven by arbitrary-shaped conductive RF antennas, and is magnetized by realistic coils or permanent magnets. Moreover, the code provides a preliminary estimation of the propulsive performances which can be adopted as target parameters in an optimization process of the plasma discharge. Finally, it is worth highlighting that this work is focused on the presentation of the code (i.e., model implemented, numerical accuracy, verification and validation) and not on its exploitation on a realistic optimization process.

The thrust stand is intended to test small-medium size HPTs (i.e., up to 1 kW input power) at the high vacuum facility of the University of Padova [66, 91, 92]. In particular, the counterbalanced pendulum concept [89] is an evolution of the hanging pendulum which allows enhancing the range of thrusters which can be handled; in fact the sensibility of the instrument can be adjusted simply reconfiguring the position and mass of the counterweights. Consequently, this very instrument allows for testing prototypes which produce a thrust in the range from tens of μNewton up to tens of milliNewton. Moreover, tens of tests per day can be accomplished and the data attained are rather accurate (2-σ uncertainty in the range of 15%).

The rest of the work is organised as follows:

Chapter 2 First, the numerical model implemented in OpenFOAM for the solution of plasma transport is presented and validated. Second, the physical assumptions and the numerical scheme of 3D-VIRTUS are discussed; moreover, the code is validated against the self-consistent solver SEMS [59] and against experimental data [93]. Finally, the coupling between 3D-VIRTUS and the analytical model of the *Acceleration Stage* is presented.

Chapter 3 The numerical model is exploited in the analysis of some simplified HPT configurations.

Chapter 4 The characterization of the reconfigurable counterbalanced pendulum thrust stand is presented. Subsequently, the reliability of the stand inside its operational range is verified testing a non-optimized medium-power (i.e., 200-300 W) HPT.

Chapter 5 The results of the numerical model are compared against the experimental data retrieved with the reconfigurable counterbalanced pendulum thrust stand.

Chapter 6 The principal findings of the research activity are discussed, future work is illustrated and the novelty made by this work highlighted.

Chapter 2

Numerical approach

2.1 Plasma fluid model

The estimation of the equilibrium condition of a Helicon plasma source requires the solution of the plasma-wave coupling, and the charged/neutral particles transport inside the discharge. For what concerns the plasma transport, a discharge filled with an inhomogeneous weakly-ionized argon plasma has been studied. Specifically, the plasma has been assumed as a multi-species mixture of electrons, and heavy species (i.e., ions, and neutral particles); notably, each species has been assumed with a Maxwellian distribution function so that a fluid treatment of the transport problem is justified. In early experiments on Helicon sources [33], high energy tails of electrons distribution function have been observed. Nonetheless in [94], by means of a careful interpretation of previous results and relying on more accurate measurements, Chen stated that deviations from Maxwellian are not so intense to have strong effects on the dynamics of a generic Helicon discharge. On the contrary, assuming a Maxwellian distribution for ions is not in general correct. Measurement performed by Scime *et al.*, [95] highlighted: (i) a strong anisotropy between the ion temperature perpendicular and parallel to the magnetic field lines, being the former up to an order of magnitude higher than the latter, (ii) perpendicular ion temperature up to 1 eV. Nonetheless, this effect is particularly intense in correspondence of the lower hybrid frequency [96]; therefore assuming a Maxwellian distribution also for ions is not expected to affect badly the results of the simulation apart from in the lower hybrid frequency range. Moreover, the reasonableness of the assumption is enforced by the good agreement, reported in [97], between the experimental results and a simplified fluid model that neglect the anisotropy of ions temperature.

Finally, it is worth to justify why this work is focused on argon discharges. In fact in space applications the majority of the electric propulsion devices is propelled with xenon gas rather than argon [6]. Nonetheless, in literature many experiments on HPTs operated with argon are reported (see Table 1.2); in fact HPTs are based on Helicon sources which are derived from industrial applications where the adoption of argon gas is predominant [10]. Consequently: (i) HPTs have been very often operated with argon to exploit the know-how on Helicon sources matured in other technological fields, and (ii) the few numerical models which solves self-consistently the Helicon sources have been

developed for argon discharges [50, 56, 57, 58, 59]. Therefore, the adoption of argon gas is forced by the necessity of comparing the actual code against well established numerical and experimental results.

2.1.1 Governing equations

In order to evaluate the species densities, fluxes, and temperatures, a set of continuity, momentum, and energy transport equations is necessary. The principal assumptions done in modelling the plasma discharge for typical dimension, magneto-static field, and neutral pressure values in Helicon sources on-board of HPTs [9, 26], are: (i) the ions are unmagnetised since the gyroradius is large compared to the characteristic scale-length of the discharge, (ii) the heavy species temperature is constant in time, homogeneous, and equal to the initial neutral gas temperature T_0, since the ions kinetics is dominated by collisions with neutral particles [29] apart from in the lower hybrid frequency range [95]. In addition, drift-diffusion approximation [98] for plasma species instead of the full momentum equation has been considered since the diffusion speed is of the same order or lower than thermal speed [99]; this description might fail in the sheath region, whose resolution has been avoided from the discharge model. Rather than, the sheath at the discharge walls has been modelled by means of appropriate boundary conditions to keep the numerical treatment efficient. As a result, the set of governing fluid equations reads

$$\frac{\partial n_k}{\partial t} + \nabla \cdot \mathbf{\Gamma}_k = R_k \tag{2.1a}$$

$$\frac{\partial \varepsilon_n}{\partial t} + \nabla \cdot \mathbf{\Gamma}_\varepsilon + \mathbf{E}_{DC} \cdot \mathbf{\Gamma}_e = R_\varepsilon \tag{2.1b}$$

$$\nabla^2 \phi = -q \left(\frac{n_i - n_e}{\varepsilon_0} \right) \tag{2.1c}$$

In general, the plasma is a mixture of different particles, therefore the mass conservation of each species is described by a dedicated continuity equation (Eq. 2.1a). From the latter, the number density of each species n_k (expressed in m^{-3}) is calculated. In the following, four species have been considered, namely: electrons (identified with the subscript e), single ionized particles (i), neutrals at the ground state (0), and neutrals at the excited state (s). In particular, R_k is a production/loss term which depends on the reactions which involve the k-th species; whereas the particles flux Γ_k is given from the drift-diffusion expression of the momentum equation

$$\mathbf{\Gamma}_k = n_k \mathbf{v}_k = \pm \mu_k n_k \mathbf{E}_{DC} - D_k \nabla n_k \tag{2.2}$$

where $\mathbf{v}_k$ is the species velocity, D_k is the species diffusivity (expressed in $\mathrm{m}^2\mathrm{s}^{-1}$), $\mathbf{E}_{DC}$ is the electrostatic field due to local imbalance of net space charge, and μ_k is the species mobility (expressed in $\mathrm{m}^2\mathrm{V}^{-1}\mathrm{s}^{-1}$), which is non-zero for charged species only, and it has positive (negative) values for ions (electrons).

At the same time, the electron energy density ε_n (expressed in Vm^{-3}) is calculated from the energy equation (Eq. 2.1b) [100]. In particular $\varepsilon_n = 3/2 T_e n_e$, where T_e is the electrons temperature (expressed in eV), and n_e the electrons number density. Moreover,

Γ_e is the electrons flux, and Γ_ε the electron energy flux which, according to the drift diffusion-approximation, reads

$$\mathbf{\Gamma}_\varepsilon = -\mu_\varepsilon \varepsilon_n \mathbf{E}_{DC} - D_\varepsilon \nabla \varepsilon_n \tag{2.3}$$

where μ_ε is the electron energy mobility (expressed in $\mathrm{m^2V^{-1}s^{-1}}$), and D_ε is the electron energy diffusivity (expressed in $\mathrm{m^2s^{-1}}$). Furthermore, $R_\varepsilon = \mathcal{E}_{chem} + \mathcal{E}_{pow}$ is the local source/sink term of energy, that is due to chemical reactions ($\mathcal{E}_{chem}$), and the RF power deposited by the antenna ($\mathcal{E}_{pow}$).

The plasma potential ϕ (expressed in V), which is associated to the $\mathbf{E}_{DC}$ field, is given by the Poisson equation (Eq. 2.1c), where n_e and n_i are respectively the electrons and ions number densities, q is the elementary charge, and ε_0 is the vacuum permittivity.

It is worth recalling that $\mathbf{E}_{DC}$ is not related to the electrostatic component of the EM waves excited by the RF antenna; the contribution of the latter to the discharge dynamics is accounted in the $\mathcal{E}_{pow}$ term. Specifically, $\mathbf{E}_{DC}$ accounts for the steady state electric field due to plasma diffusion and not to the oscillating electric field due to the RF power coupling [101]. Finally, it must be pointed out that the $\mathcal{E}_{pow}$ term, considered as an input parameter for this model, must be calculated by a dedicated tool capable of describing the EM wave propagation in a magnetized and non-uniform plasma. Moreover, provided that the non uniformity of the the plasma profile can drastically influence the power deposition (i.e., the $\mathcal{E}_{pow}$ term) [39], a self consistent model of the Helicon discharge is obtained iterating the fluid model here described and an EM solver [53] devoted to the calculation of $\mathcal{E}_{pow}$ (see Sec. 2.2).

Plasma Chemistry

The production and loss terms in the continuity equations of the charged particles include different reactions. Argon discharges have been studied, and thus the chemical reactions considered are the elastic scattering, the neutrals ionization, the excitation, and the excited ionization (see Tab. 2.1) for the neutral (Ar), the excited ($\mathrm{Ar^*}$), the single-ionized ($\mathrm{Ar^+}$), and the electron (e) species. Since plasma species have been assumed with Maxwellian distribution function, the reaction rate constants (i.e., k_{el}, k_{iz}, k_{ex}, k_{siz}, for elastic scattering, neutrals ionization, excitation, and excited ionization, respectively) can be expressed as a function of the electron temperature by means of empirical relations [29, Eqs.(5.3.16,17)]. As a result

$$R_e = R_i = k_{iz} n_e n_0 + k_{siz} n_e n_s \tag{2.4}$$

for the electrons (ions) production/loss term, i.e., R_e (R_i), while for the neutral

$$R_0 = -k_{iz} n_e n_0 - k_{ex} n_e n_0 \tag{2.5}$$

and for the excited production/loss term (R_s)

$$R_s = k_{ex} n_e n_0 - k_{siz} n_e n_s \tag{2.6}$$

The chemical contribution in the electron energy equation (see Eq. 2.1b) reads

$$\mathcal{E}_{chem} = \mathcal{E}_{el} + \mathcal{E}_{iz} + \mathcal{E}_{ex} + \mathcal{E}_{siz} \tag{2.7}$$

$Ar + e \longrightarrow Ar + e$	Elastic Scattering
$Ar + e \longrightarrow Ar^+ + 2e$	Neutrals Ionization
$Ar + e \longrightarrow Ar^* + e$	Excitation
$Ar^* + e \longrightarrow Ar^+ + 2e$	Excited Ionization

Table 2.1: Summary of the chemical reactions in an argon plasma discharge.

in which the four contributions are: (i) $\mathcal{E}_{el} = -3m/MT_e(k_{el}n_en_0)$, for the elastic loss; (ii) $\mathcal{E}_{iz} = -\Delta_{iz}(k_{el}n_en_0)$ for the neutral-ionization loss; (iii) $\mathcal{E}_{ex} = -\Delta_{ex}(k_{ex}n_en_0)$ for the excitation loss; (iv) $\mathcal{E}_{siz} = -\Delta_{siz}(k_{siz}n_en_s)$ for the excited-ionization loss. In particular, m (M) is the electron (ion) mass, $\Delta_{iz} = 15.80$ V is the first ionization energy, $\Delta_{ex} = 12.14$ V is the excitation energy, while $\Delta_{siz} = 4.427$ V is the energy required to ionize an excited particle [29, Tab.(3.3)]. Finally, it is worth to point out that, in order to ease the numerical treatment, the Ar^* species comprises the particles at all the different excitation levels. Therefore k_{ex} and k_{siz} are derived summing the contributions due to each excitation level, as long as Δ_{ex} and Δ_{siz} averaging the energy losses weighted for the rate constants [102]. Moreover, this approach has been previously adopted in literature for studying Helicon discharges without undermine the accuracy of the results [29, 50, 57, 58].

The electron mobility, in the presence of a magneto-static field $\mathbf{B}_0 = (B_{0x}, B_{0y}, B_{0z})$ in a system of Cartesian coordinates, reads [103]

$$\mu_e = \frac{\tilde{\mu_e}}{\tilde{\mu_e}^{-2} + |\mathbf{B}_0|^2} \begin{pmatrix} \tilde{\mu_e}^{-2} + B_{0x}^2 & -B_{0z}/\tilde{\mu_e} + B_{0x}B_{0y} & B_{0y}/\tilde{\mu_e} + B_{0z}B_{0x} \\ B_{0z}/\tilde{\mu_e} + B_{0x}B_{0y} & \tilde{\mu_e}^{-2} + B_{0y}^2 & -B_{0x}/\tilde{\mu_e} + B_{0y}B_{0z} \\ -B_{0y}/\tilde{\mu_e} + B_{0z}B_{0x} & B_{0x}/\tilde{\mu_e} + B_{0y}B_{0z} & \tilde{\mu_e}^{-2} + B_{0z}^2 \end{pmatrix} \tag{2.8}$$

with $\tilde{\mu_e}$ the scalar electron mobility in absence of any magneto-static field

$$\tilde{\mu_e} = \frac{q}{m\ (n_0\ k_{el} + n_0\ k_{iz} + n_0\ k_{ex} + n_s\ k_{siz})} \tag{2.9}$$

The other transport coefficients follow from the Einstein's relations, namely: $D_e = \mu_e T_e$, $\mu_\varepsilon = 5/3\mu_e$, and $D_\varepsilon = \mu_\varepsilon T_e$. In regards to the heavy species (i.e., neutrals, excited, and ions), the diffusion coefficient can be expressed as [104]

$$D_k = \frac{3}{8}\frac{\sqrt{\pi k_B T_0/M}}{\pi\sigma_D^2\Omega_D}\frac{1}{n_0 + n_s + n_i} \quad , \quad k = 0, s, i \tag{2.10}$$

in which k_B is the Boltzmann's constant, whereas σ_D, and Ω_D depend on Lennard-Jones parameters that can be inferred from [105], while the mobility follows form the Einstein's relation $\mu_i = D_i/T_0$.

Boundary Conditions

Assuming that $\hat{\mathbf{k}}$ is the unit vector perpendicular to the domain boundary, and it is directed outward from the domain; the boundary conditions for the continuity equation (Eq. 2.1a) for charged species are given through a Robin boundary condition that enforces the Bohm sheath criterion [29], and that reads

$$\pm \left(\mu_k \mathbf{E}_{DC}\right) \cdot \hat{\mathbf{k}}\, n_k - \left(D_k \nabla n_k\right) \cdot \hat{\mathbf{k}} = \Gamma_\perp \tag{2.11}$$

in which $\Gamma_\perp = \Gamma_e = \Gamma_i = \sqrt{qT_e/M}n_i$ for ion, and electron fluxes.

In regards to the continuity of excited and neutral species, a Neumann boundary condition has been imposed, that reads

$$\frac{\partial n_k}{\partial x_\perp} = -\frac{\Gamma_\perp}{D_k} \tag{2.12}$$

in which $\frac{\partial}{\partial x_\perp}$ is the derivative along the $\hat{\mathbf{k}}$ direction. For the excited species, the boundary condition depends on the particles thermal flux [106], and $\Gamma_\perp = \Gamma_s = \frac{1}{2} v_{th,0} n_s$ in which $v_{th,0} = \sqrt{8k_B T_0/(\pi M)}$ is the average thermal speed of the heavy particles. As for the neutral species boundary condition, all the ions and the excited particles which collide against the wall have been assumed to recombine [101] in accordance with the wall reactions $Ar^+ \longrightarrow Ar$, and $Ar^* \longrightarrow Ar$; so that $\Gamma_\perp = \Gamma_0 = -(\Gamma_i + \Gamma_s)$. Similarly, for the energy equation (Eq. 2.1b), Bhom sheath criterion [100] has been imposed through a Robin boundary condition that reads

$$-\left(\mu_\varepsilon \mathbf{E}_{DC}\right) \cdot \hat{\mathbf{k}}\, \varepsilon_n - \left(D_\varepsilon \nabla \varepsilon_n\right) \cdot \hat{\mathbf{k}} = \Gamma_{\varepsilon,\perp} \tag{2.13}$$

in which $\Gamma_{\varepsilon,\perp} = \left[\frac{T_e}{2}\left(1 + \ln\frac{M}{2\pi m}\right) + 2T_e\right]\Gamma_e$.

As for the Poisson equation (Eq. 2.1c), the boundary value of the electric potential is defined by using a Dirichlet boundary condition as follows [101]

$$\phi = 0 \tag{2.14}$$

2.1.2 Implementation

The system of equations that describes the plasma transport have been resolved with OpenFOAM that solves differential problems with the Finite-Volume (FV) approach [90]. The Poisson, continuity, and electron energy equations have been time integrated in this specific order, and have been spatially discretised on a 3D structured (hexahedral) mesh.

The time discretisation and the approach to advance the solutions in time have been decided to avoid severe time step restriction, which may lead to prohibitive computational run time, while allowing for stable and accurate solutions. In regards to the Poisson equation, the electrostatic potential has been obtained from a semi-implicit solution of the equation that gives the potential ϕ at the time instant $t+1$ by means of

$$\varepsilon_0 \nabla^2 \phi^{t+1} = -q(n_i^{t+1} - n_e^{t+1}) = -q\left(n_i^t + \Delta t \frac{\partial n_i^t}{\partial t} - n_e^t - \Delta t \frac{\partial n_e^t}{\partial t}\right) \tag{2.15}$$

in which Δt is the time step; the electron (n_i^{t+1}), and ion (n_e^{t+1}) densities at the $(t+1)$-th time step have been linearised by substituting $n_k^{t+1} = n_k^t + \Delta t \frac{\partial n_k^t}{\partial t}$ (with $k = i, e$), in which $\frac{\partial n_k^t}{\partial t}$ comes from Eq. 2.1a at the t-th time step [107]. Thanks to this approach, the Poisson's equation is not affected by the dielectric relaxation constraint, which can severely limit the maximum time step [107, 108]. The continuity equation has been treated with an implicit scheme, and reads

$$\frac{n_k^{t+1} - n_k^t}{\Delta t} + \nabla \cdot \mathbf{\Gamma}_k^{t+1} = \frac{n_k^{t+1} - n_k^t}{\Delta t} + \nabla \cdot \left(\pm \mu_k^t n_k^{t+1} \mathbf{E}^{t+1} - D_k^t \nabla n_k^{t+1} \right) = R_k^t \tag{2.16}$$

Such a formulation avoids the Courant-Friedrichs-Lewy (CFL) constraint [107, 108]. Finally, the energy equation has been discretised as

$$\frac{\varepsilon_n^{t+1} - \varepsilon_n^t}{\Delta t} + \nabla \cdot \mathbf{\Gamma}_\varepsilon^{t+1} + \mathbf{E}^{t+1} \cdot \mathbf{\Gamma}_e^{t+1} = R_\varepsilon^t \tag{2.17}$$

The time derivatives have been discretised with the first order implicit Euler scheme [109, Chap. 13.3]. Differential operators have been discretised in space in accordance with: the classical combination of the divergence theorem and the gradient discretisation for the laplacian [109, Chap. 8.1], the Green-Gauss method for the gradient [109, Chap. 9.2], the central-difference scheme for the divergence [109, Chap. 11.2]. The boundary conditions are treated according to the classical schemes for Dirichlet, Neumann, and Robin conditions [109, Chap. 8.3]; notably, 1D and 2D (e.g., axisymmetric) problems can be handled by means of special boundary conditions [110].

The above-mentioned system of equations is solved until the achievement of the steady state which is identified, by means of the SIMPLE residual control algorithm [110] on the electron density, when the relative difference between the electron density at two consecutive time steps is lower than a given threshold ($\epsilon_{F,max}$). Clearly, the value imposed for $\epsilon_{F,max}$ affects both the accuracy of the results and the computational time.

2.1.3 Numerical accuracy

A detailed analysis on the numerical accuracy of the plasma fluid model has been performed as the grid refinement, and the integration time step are varied. To this end, a cylindrical Helicon plasma source has been considered which has radius $R = 0.01$ m, length $L = 0.10$ m, and whose axis is aligned with the z direction of a cylindrical coordinate system (r, θ, z). Provided that this analysis is focused only on the numerical accuracy of the plasma fluid model, a power deposition profile has been assumed in the form $\mathcal{E}_{pow}(r, z) = \mathcal{E}_{pow}^0 \left[1 + (1 - r/R)^2 + 0.25\,(1 - 2z/L)\ \ (1 + 2z/L)\right]$ with $\mathcal{E}_{pow}^0 = 10^6$ W/m^3. Three cases have been analysed: initial neutral number density $n_0 = 3 \times 10^{20}$ m^{-3} and uniform axial magneto-static field $B_0 = 1000$ G (hereinafter referred as *high magnetization*), $n_0 = 10^{21}$ m^{-3} and $B_0 = 750$ G (*medium magnetization*), and $n_0 = 10^{22}$ m^{-3} and $B_0 = 0$ G (*low magnetization*). Higher (lower) values of magneto-static field have been associated to lower (higher) values of initial neutral density in order to amplify (reduce) the anisotropy induced on the diffusion parameters. Due to the inherent symmetry of the case at hand, and to keep the analysis lucid, a 2D axisymmetric problem has been solved

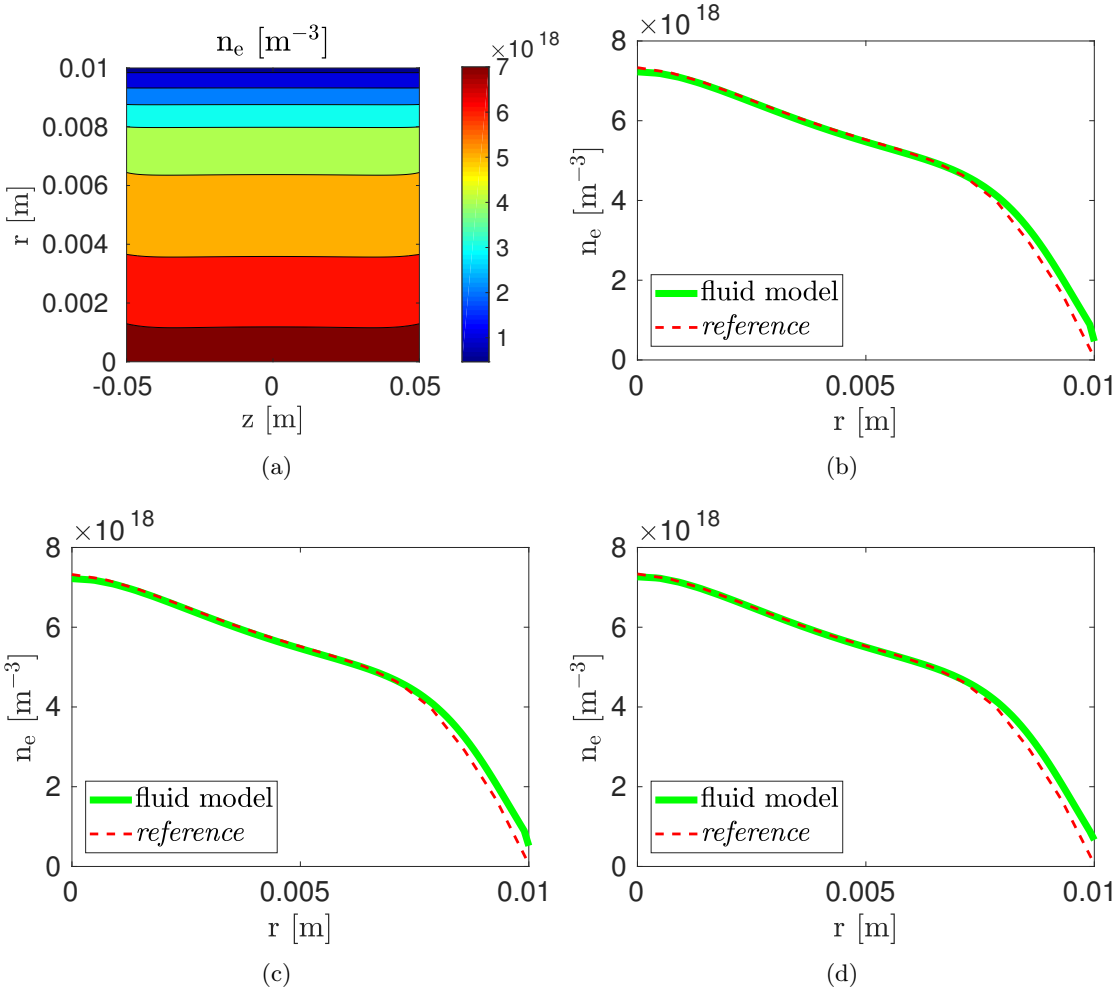

Figure 2.1: *High magnetization* case, initial neutral plasma density $n_0 = 3 \times 10^{20}$ m^{-3}, axial magneto-static field $B_0 = 1000$ G. (a) The *reference* electron density distribution within the Helicon discharge; comparison between the *reference* (dashed line), and the fluid model (solid line) solution for the electron density profile along the radius of the discharge at (b) $z = 0$ m, (c) $z = 0.25$ m, (d) $z = 0.05$ m.

by the fluid model with $\epsilon_{F,max} = 10^{-5}$, and the results of the electron density have been compared against those obtained by COMSOL Multiphysics ® [111], hereinafter referred to as *reference*. The simulations have been performed on a machine equipped with Intel ®Core i7-6700HQ CPU @ 2.60GHz × 8, and 16 Gb of RAM.

First, the effect of the grid refinement have been analysed by solving the 2D transport problem with different mesh configurations, that can be uniquely identified by the number of radial (N_r), and axial (N_z) nodes as follows $(N_r, N_z) \in \{(10, 100), (25, 250), (50, 500), (100, 1000), (200, 2000)\}$. The comparison between the *reference* electron density and the results of the fluid model have been reported respectively in Fig. 2.1 for the *high magnetization*, in Fig. 2.2 for the *medium magnetization*, and in Fig. 2.3 for the *low magnetization*.

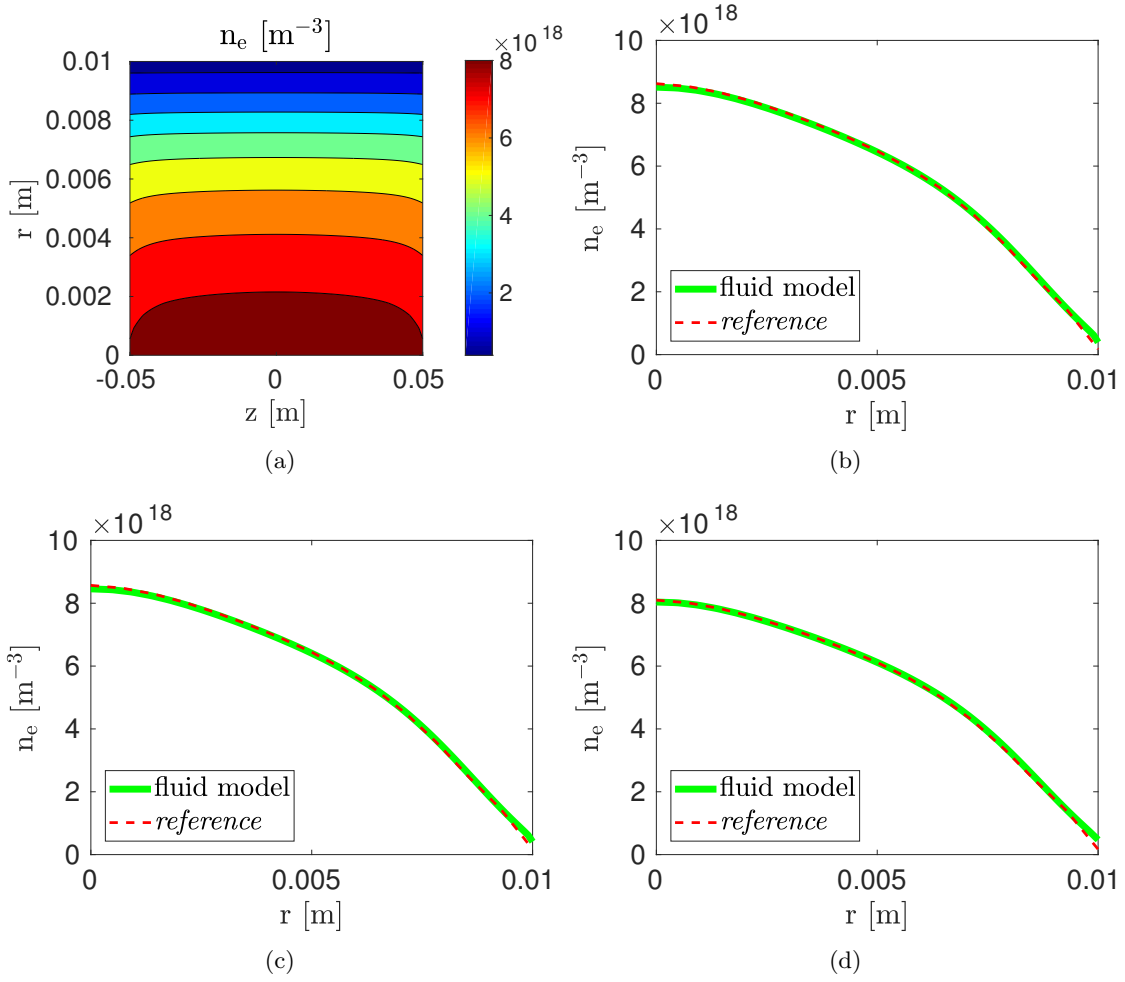

Figure 2.2: *Medium magnetization* case, initial neutral plasma density $n_0 = 10^{21}$ m^{-3}, axial magneto-static field $B_0 = 750$ G. (a) The *reference* electron density distribution within the Helicon discharge; comparison between the *reference* (dashed line), and the fluid model (solid line) solution for the electron density profile along the radius of the discharge at (b) $z = 0$ m, (c) $z = 0.25$ m, (d) $z = 0.05$ m.

Specifically, Figs. 2.1-2.3 depict the *reference* electron density (see Figs. 2.1(a)-2.3(a)) and the comparison against the solution of fluid model along the radius of the discharge at three different axial sections. For the sake of brevity, only the solution for $N_r = 50$ and $N_z = 500$ have been reported. Notably, the results of the two codes show an excellent agreement for all the three *magnetization* cases considered, which allows concluding that the fluid model has been correctly implemented. It is worth recalling that similar results hold true for the other plasma species densities, and electron temperature. As the mesh gets finer and finer, the percent error, which has been evaluated between the *reference* electron density and the solution of the fluid model at the bulk of the discharge, decreases below $< 1\%$ for all the *magnetization* cases (see Fig. 2.4(a)). As the number of nodes

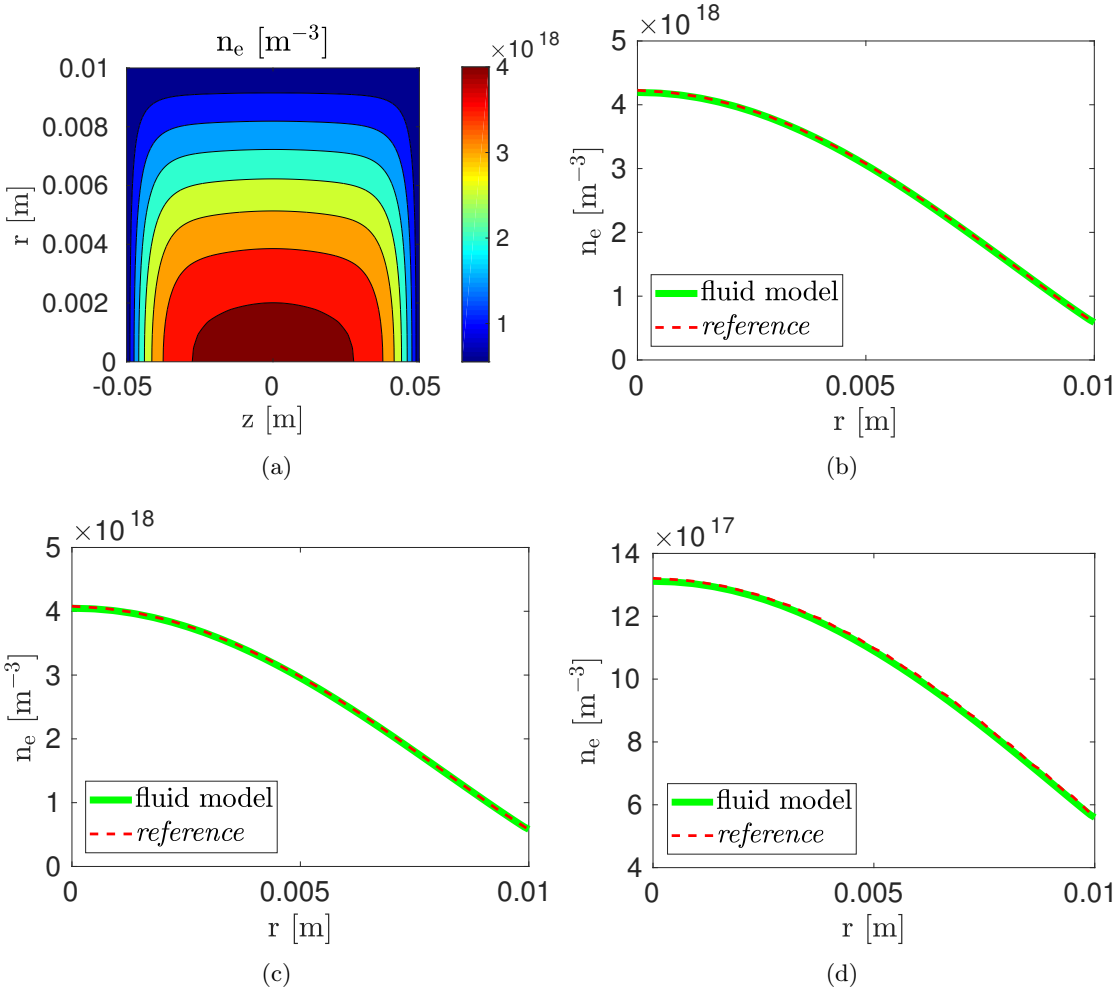

Figure 2.3: *Low magnetization* case, initial neutral plasma density $n_0 = 10^{22}$ m^{-3}, axial magneto-static field $B_0 = 0$ G. (a) The *reference* electron density distribution within the Helicon discharge; comparison between the *reference* (dashed line), and the fluid model (solid line) solution for the electron density profile along the radius of the discharge at (b) $z = 0$ m, (c) $z = 0.25$ m, (d) $z = 0.05$ m.

increases, the computational cost of the fluid model grows as evidenced by the increase of the simulation run time (see Fig. 2.4(b)), and the memory consumption (see Tab. 2.2). Therefore, as a rule of thumb, the number of mesh nodes should be decided according to the steepness of the gradients of the plasma parameters, while keeping in mind that the computational burden increases as the grid refinement does so.

In regards to the time discretization, the effect of the integration time step on the transport solution of the above-mentioned Helicon discharge have been studied for the three *magnetization* cases, keeping the same mesh configuration with $N_r = 50$, and $N_z = 500$. The percent error (between the *reference*, and the fluid model solutions) of the electron density at the bulk of the discharge remains almost constant as the time step

configuration	N_r	N_z	memory usage [Gb]
1	10	100	0.0468
2	25	250	0.1092
3	50	500	0.1560
4	100	1000	0.4524
5	200	2000	1.6540

Table 2.2: Memory usage for distinct mesh configurations with different radial (N_r), and axial (N_z) node numbers.

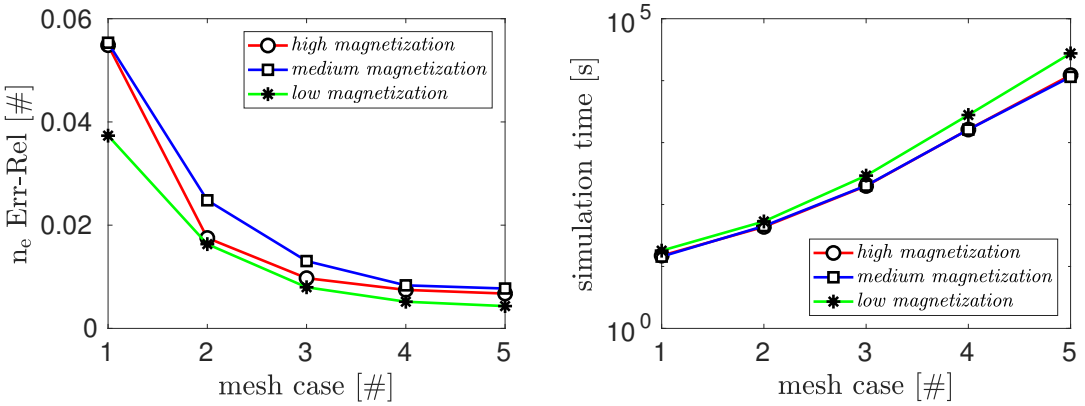

Figure 2.4: (a) Percent error between the *reference* and the fluid model solutions of the electron density at the bulk of the discharge; (b) simulation time. Different mesh configurations (see Tab. 2.2) and magnetization degrees (see Figs. 2.3-2.1) analysed.

increases (see Tab. 2.3). These results confirm that the semi-implicit treatment of the transport equations allows larger time steps, while providing stable solutions for typical dimension, magneto-static field, and neutral pressure values in Helicon sources on-board of HPTs. Nonetheless, the time step has to be lower than a threshold value (Δt_{max}) [112, Thm. 9] to guarantee the convergence of the continuity, and energy equations. In general, the plasma parameters have a marked influence on this threshold value, which in this specific cases is 2.5×10^{-7} s for *high magnetization* and *medium magnetization*, and 5.0×10^{-8} s for *low magnetization* case.

2.2 Helicon plasma source model

In order to describe a Helicon discharge realistically, the RF antenna, the plasma discharge, along with any additional component (e.g., dielectric vessel, electromagnets, conducting shields), either metallic or dielectric have been modelled. The confinement magneto-static field can be either uniform, and aligned with the discharge axis, as it is usually assumed

magnetization	Δt [s]	percent error [%]	simulation time [s]
high	1×10^{-9}	0.937	1.716×10^{4}
	1×10^{-8}	0.934	1.736×10^{3}
	1×10^{-7}	0.935	2.061×10^{2}
	2.5×10^{-7}	0.938	9.428×10^{1}
medium	1×10^{-9}	1.320	1.595×10^{4}
	1×10^{-8}	1.315	1.700×10^{3}
	1×10^{-7}	1.316	2.016×10^{2}
	2.5×10^{-7}	1.317	9.190×10^{1}
low	1×10^{-9}	0.733	1.877×10^{4}
	1×10^{-8}	0.589	2.320×10^{3}
	5×10^{-8}	0.539	5.553×10^{2}

Table 2.3: Simulation time and percent error between the electron density at the bulk of the discharge calculated by the *reference* and the fluid model. Results are expressed as function of the integration time step (Δt), and for three different *magnetization* degrees.

in Helicon investigations, or can be the actual confinement field that is generated by a realistic arrangement of electromagnets (or permanent magnets). The formulation does not rely on any specific shape of both the antenna, and the plasma regions; besides, the RF antenna like any other metallic part has been assumed as Perfectly Electric Conductor (PEC). The discharge is filled with an inhomogeneous weakly-ionized argon plasma, that is modelled as multi-fluid mixture of electrons, and heavy species (i.e., ions, and neutral particles).

In order to obtain a self-consistent estimation of the equilibrium condition of the Helicon plasma source, both the plasma-wave coupling and the charged/neutral particles transport inside the discharge have to be resolved. Specifically, the RF antenna, which is fed with a voltage in the range of tens of MHz (e.g. 1 - 30 MHz), launches EM waves that propagate into the plasma, and are ultimately absorbed by the latter; such phenomena have time scales in the order of 10^{-6} s. Consequently, the plasma configures itself under the forcing action of the RF deposited power, with characteristic times of approximately 10^{-3} s [50, Tab.(2.1)]. From a physical standpoint, the independent solution of the plasma-wave coupling, and the transport phenomena is justified since the two physical processes are well separated.

The electromagnetic fields propagating inside the plasma cylinder has been calculated in the frequency domain with ADAMANT code [53], that provides the local values of the electric flux density ($\mathbf{D}_\mathrm{p}$), and polarization currents ($\mathbf{J}_\mathrm{p}$) inside the plasma. From the knowledge of the local value of the fields and currents, the local RF power coupled into

the plasma ($\mathcal{E}_{pow}$) has been calculated by integrating the electrical work [53, Eq.(12)]. The calculated RF power delivered to the plasma is then used as an input in the problem of the macroscopic transport. It is worth recalling that in ADAMANT the plasma discharge is treated as an inhomogeneous, lossy, and anisotropic medium characterized by a relative permittivity dielectric tensor [113]. This formulation gives a reasonable description of the electrical behaviour of a magnetized plasma, and in turn of the RF power deposition, only if non-linear and non-local effects of wave-particle interaction are negligible [52]. Therefore waves are assumed to be dumped only by collisional effects [37, Chap. 4], and channels of RF power deposition as (i) Landau dumping [94], and (ii) parametric decay instabilities [96] have been neglected. Notably, the former has been proved to play a minor role in a typical Helicon discharge [94], while the latter is the responsible of the anisotropy on ion temperature measured in the range of the lower hybrid frequency [96].

2.2.1 Implementation

To numerically evaluate the equilibrium conditions of the Helicon plasma discharge, 3D-VIRTUS has been employed; the code is comprised of two distinct modules (see Fig. 2.5), namely: the EM module, and the FLUID module. The former relies on the ADAMANT code [53] to solve for the EM fields that propagate inside the discharge, and the power deposition therein for a given distribution of the density, and temperature of the plasma species. The latter is charged with the solution of the transport problem in the plasma for a given RF power deposition distribution, and provides the local plasma parameters (i.e., plasma species density, and electron temperature) within the discharge. After being initialized with uniform values of the plasma parameters, the two modules have been coupled by means of an iterative procedure until convergence of the plasma parameters to find out the equilibrium conditions. From the numerical standpoint, the EM (FLUID) module relies on an unstructured (structured) mesh; therefore, the power deposition that is computed by the EM module is interpolated on the structured mesh of the FLUID module,

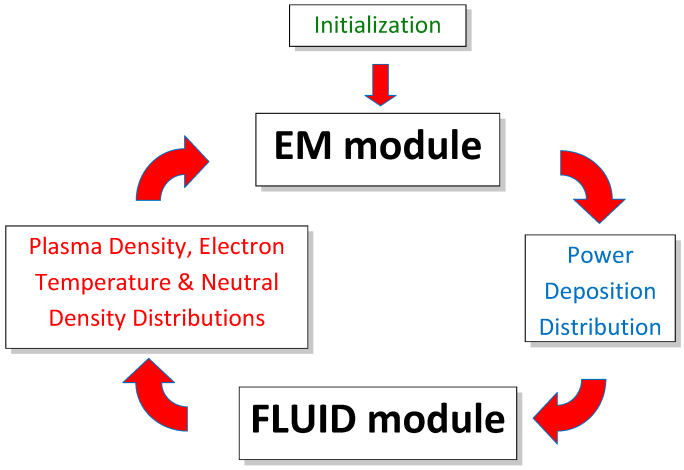

Figure 2.5: Schematic of the iterative loop that has been implemented in 3D-VIRTUS.

while the plasma parameters that are evaluated by the FLUID module are interpolated on the unstructured mesh of the EM module. To verify that a converged solution has been found, the code checks that the residual of the electron density of two consecutive iterations is lower that a prescribed threshold ($\epsilon_{\max}$)

$$\max_j \left(\frac{n_{e,j}^{i+1} - n_{e,j}^{i}}{n_{e,j}^{i}} \right) \leq \epsilon_{\max} \quad , \quad j = 1, \ldots, N_F \tag{2.18}$$

in which j, and N_F are the node index, and the number of nodes, respectively, in the structured mesh, whereas i indicates the iteration step.

2.2.2 Numerical accuracy

The accuracy of the numerical solution provided by 3D-VIRTUS depends on: (i) the mesh of the EM module, (ii) the mesh of the FLUID module, (iii) the interpolation procedure. The relation between the accuracy of the FLUID module and the mesh has been discussed in Sec. 2.1.3; while a sensibility analysis on the mesh of the EM module can be found in [53]. In the following, the interpolation procedure has been discussed.

In order to accomplish the iteration process of 3D-VIRTUS, the output of the EM module, provided in an unstructured mesh, has to be interpolated in the structured mesh of the FLUID module and vice-versa. In particular, the interpolation of the power deposition on the structured mesh of the FLUID module is a critic operation because numerical noise can be introduced. In order to overcome this problem, an auxiliary structured interpolation grid, hereinafter referred as *samplig grid*, has been introduced; the latter is usually coarser than the mesh of the FLUID model. The power is distributed in the *samplig grid* in accordance with the following procedure: (i) the power deposited in each tetrahedron of the unstructured mesh is provided in output of the EM module; (ii) the power associated to a tetrahedron is distributed among the nodes of the element of the *samplig grid* which contains the baricenter of this very tetrahedron (see Fig. 2.6(a)); (iii) the total power associated to each node of the *samplig grid* is divided by a proper co-volume [49] in order to obtain a map of the RF power deposited by the antenna $\mathcal{E}_{pow}$. Finally, $\mathcal{E}_{pow}$ is interpolated from the *samplig grid* to the mesh of the FLUID module. A particular advantage derived from the introduction of the sampling grid is that the 3D output of the EM module can be easily interpolated in a 1D or 2D mesh: e.g., if the plasma transport is treated as a 1D-radial problem in a cylindrical plasma discharge, the *samplig grid* consists of coaxial cylindrical shells (see Fig. 2.6(b)).

A sensibility analysis is required to select a *sampling grid* which provides an accurate description of the power deposition profile without introducing numerical noise. An example is presented in Fig. 2.7 for a cylindrical plasma source of length $L = 0.10$ m, and radius $R = 0.01$ m. The discharge is driven by a single loop antenna in presence of an axial magneto-static field $B_0 = 350$ G. The plasma is uniform with density $n = 1 \times 10^{18}$ m^{-3}, electron temperature $T_e = 3$ eV, and neutral pressure $p_n = 30$ mTorr. The unstructured plasma mesh is composed of 8743 tetrahedra. Because of the symmetry of the problem, the output of the interpolation is a 2D-axisymmetric power deposition profile $\mathcal{E}_{pow}$. Specifically, three interpolation grids have been analysed, namely: radial nodes $N_r = 6$ and axial nodes $N_z = 4$ (hereinafter referred as grid A), $N_r = 20$ and $N_z = 7$ (grid B),

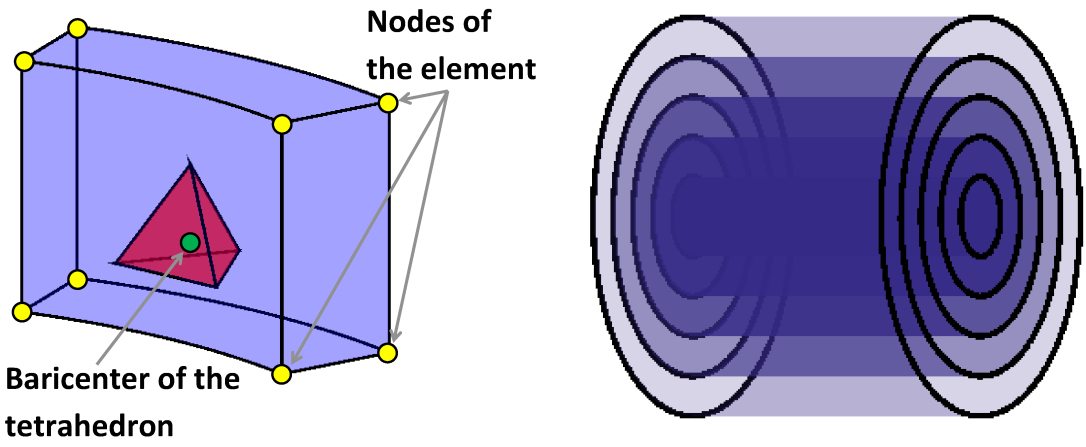

(a) (b)

Figure 2.6: (a) Element of the *sampling grid* (represented with blue faces), and a tetrahedron of the unstructured mesh whose baricenter is included inside the element (represented with red faces). (b) Example of *sampling grid* if the discharge has a cylindrical geometry, and a 1D-radial problem is solved in the FLUID module.

$N_r = 20$ and $N_z = 20$ (grid C). The power profile associated to the grid A is quite coarse (see Fig. 2.7(a)), while the grid C provide noisy results (see Fig. 2.7(c)); the best power deposition profile is obtained with the grid B (see Fig. 2.7(b)). A rule of thumb to select properly the *sampling grid* is: the distance between two consecutive nodes should be in the same range of the average side of the tetrahedra which constitute the unstructured mesh.

2.2.3 Verification

In order to verify the correct implementation of the numerical model and to check the reliability of the new code when handling real-life plasma discharges, the results of 3D-VIRTUS has been compared against the published results of: (i) a self-consistent numerical model of a Helicon source [59], (ii) the measurements performed on a Helicon reactor [93]. It is worth to point out that the EM module (i.e., the ADAMANT code) has been previously validated against both analytical, numerical and experimental data on Helicon sources [53], therefore further analyses seem not necessary. On the contrary, the FLUID module has been verified only against another numerical code (see Sec. 2.1.3); nonetheless it seems more convenient to proceed directly to the comparison of the self-consistent code (i.e. 3D-VIRTUS) against experimental data provided the difficulty of measuring accurately $\mathcal{E}_{pow}$ (necessary to run the FLUID module) in a geometry relevant for the HPT application.

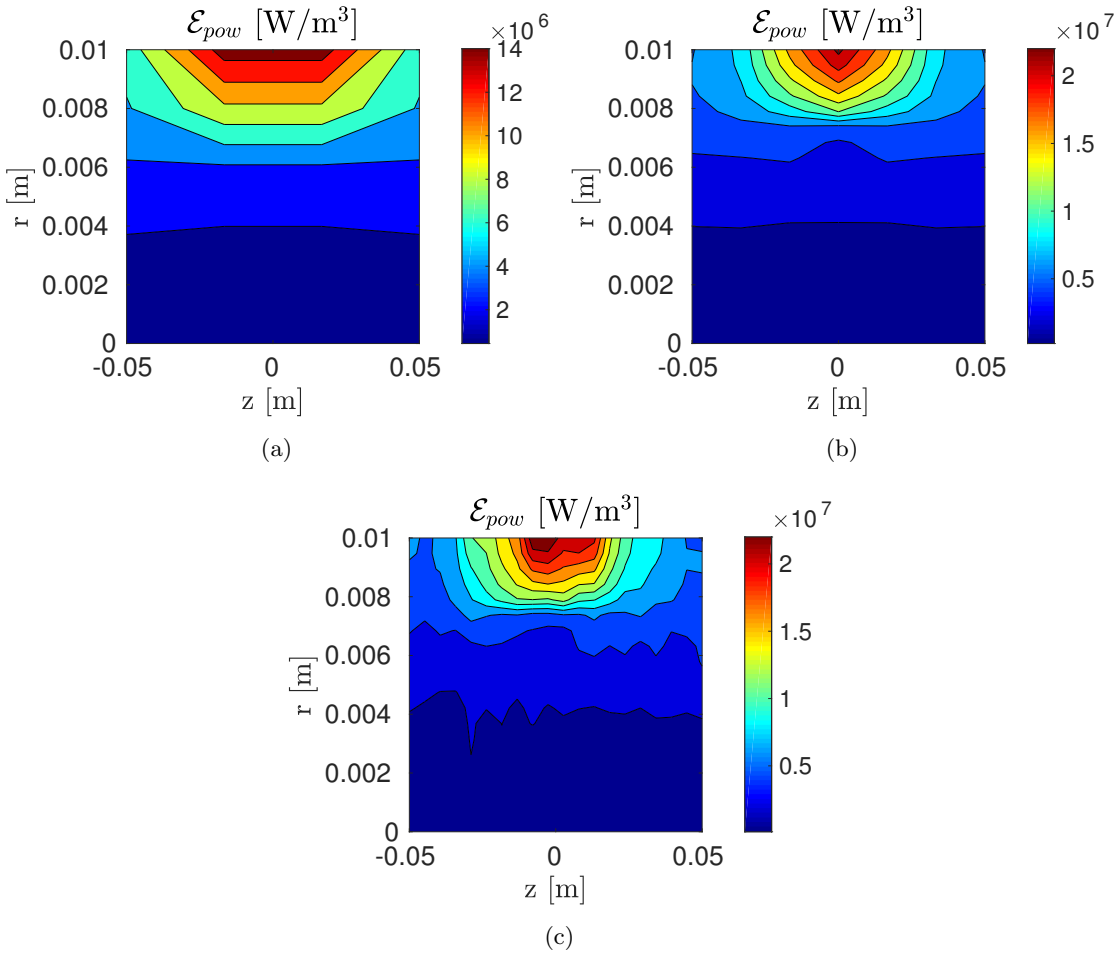

Figure 2.7: Power deposition profile $\mathcal{E}_{pow}$ for a discharge driven by a single loop antenna, axial magneto-static field $B_0 = 350$ G, uniform plasma density $n = 1 \times 10^{18}$ m^{-3}, electron temperature $T_e = 3$ eV, and neutral pressure $p_n = 30$ mTorr. Three *sampling grid* tested: (a) radial nodes $N_r = 6$ and axial nodes $N_z = 4$, (b) $N_r = 20$ and $N_z = 7$, (c) $N_r = 20$ and $N_z = 20$.

Verification against a well established numerical code

To provide an independent benchmarking of the new code with another well-established code, 3D-VIRTUS has been compared against SEMS. The latter solves plasma transport and wave differential equations in 2D axisymmetric problems by means of a finite-difference method using a fully coupled implicit scheme; the propagation is driven by a RF antenna, which is modelled as an assumed current distribution. Specifically, 3D-VIRTUS has been benchmarked against the equilibrium power deposition, and plasma parameters profiles calculated by SEMS in a Helicon reactor filled with argon gas [59].

For this test, the Helicon discharge of [59, Fig. 2] has been considered in two configurations, namely unmagnetised (i.e., $B_0 = 0$ G), and magnetised (i.e., $B_0 = 100$ G);

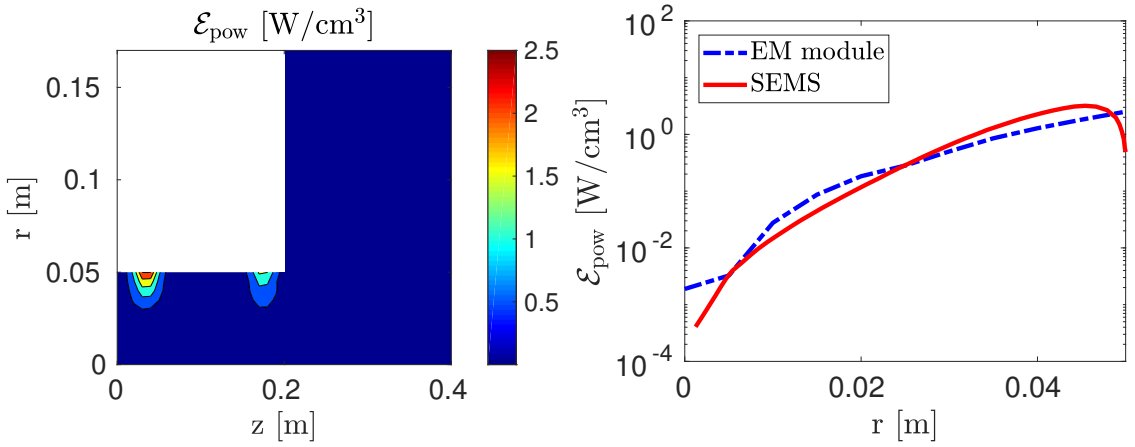

(a) (b)

Figure 2.8: (a) The power deposition distribution ($\mathcal{E}_{pow}$), and (b) the radial power deposition profile ($\mathcal{E}_{pow}$) as in [59, Figs. (7),(8)] for $B_0 = 0$ G. EM module (dashed line), SEMS (solid line).

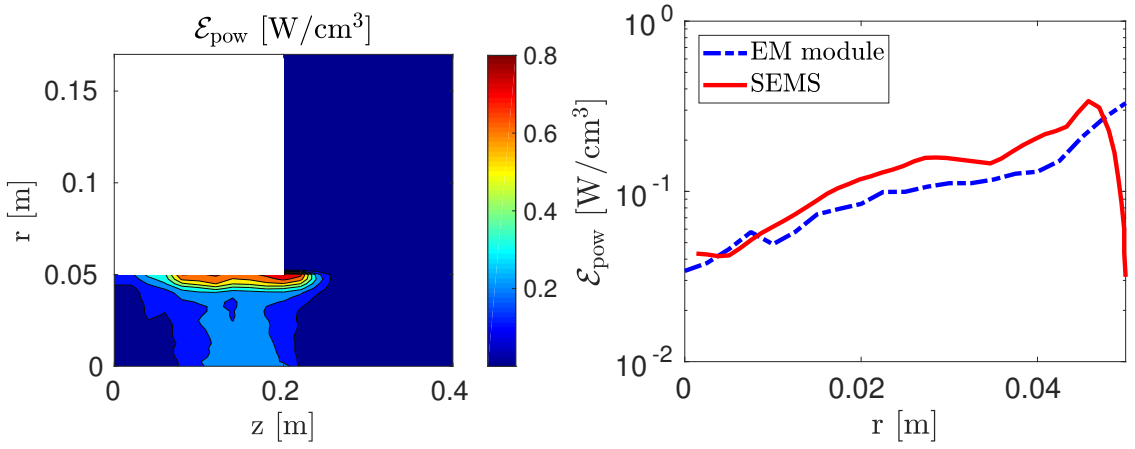

(a) (b)

Figure 2.9: (a) The power deposition distribution ($\mathcal{E}_{pow}$), and (b) the radial power deposition profile ($\mathcal{E}_{pow}$) as in [59, Fig. (7),(8)] for $B_0 = 100$ G. EM module (dashed line), SEMS (solid line).

whereas the RF antenna is made of two circular coils 180° out of phase. The number of coils of the electromagnets have been decided to get the same magnetic field lines of [59, Fig. 2]; similarly, the current of the coils has been tuned to obtain the same magneto-static field magnitude that has been specified in [59, Sec.III], which has been assumed to be the maximum value realized on the axis of the discharge. The equilibrium power deposition $\mathcal{E}_{pow}$, electron density n_e, and electron temperature T_e distribution have been solved by 3D-VIRTUS with prescribed threshold values $\epsilon_{F,max} = 10^{-5}$, and $\epsilon_{\rm max} = 10^{-1}$; besides,

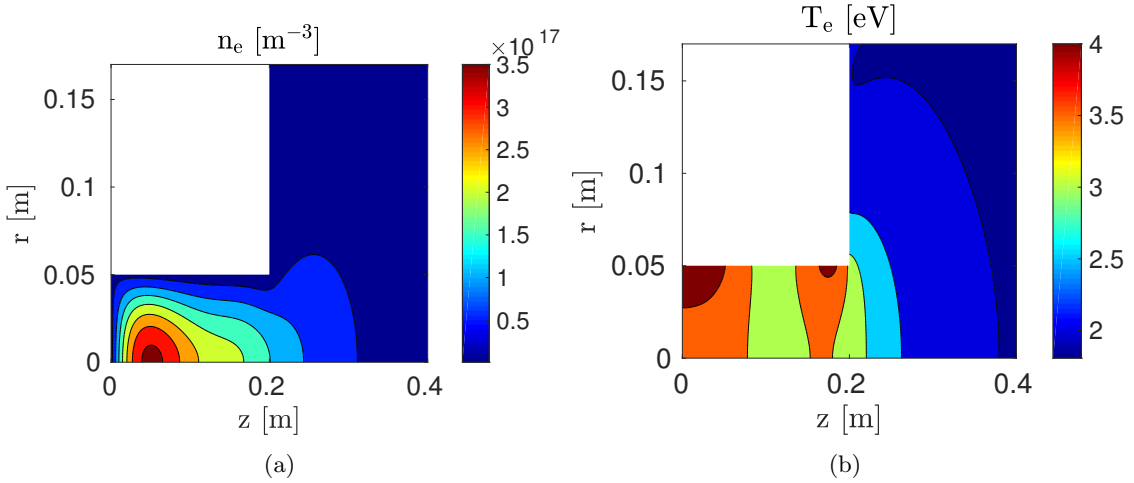

(a) (b)

Figure 2.10: The distribution of (a) the electron density (n_e), and (b) the electron temperature (T_e) computed by 3D-VIRTUS in the unmagnetised ($B_0 = 0$ G) configuration.

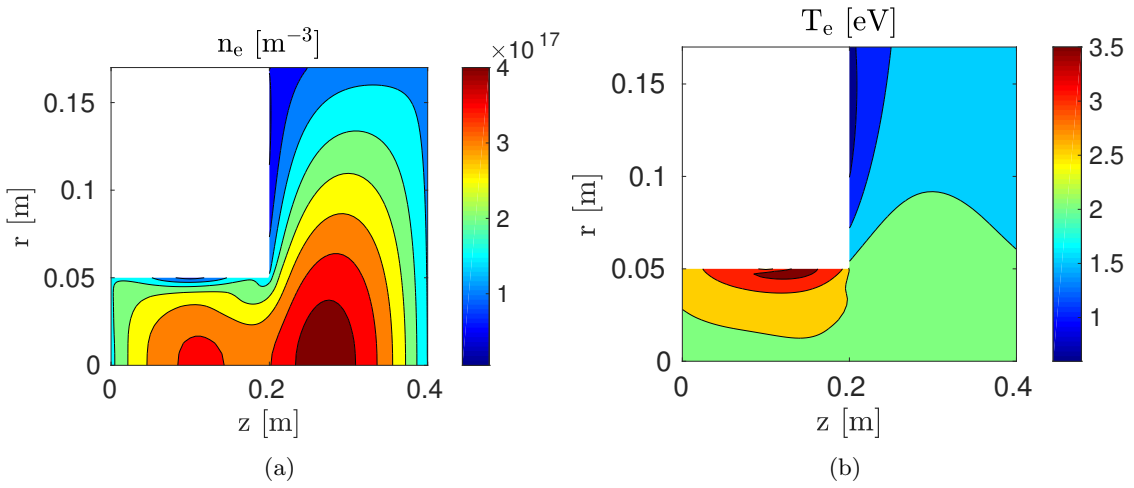

(a) (b)

Figure 2.11: The distribution of (a) the electron density (n_e), and (b) the electron temperature (T_e) computed by 3D-VIRTUS in the magnetised ($B_0 = 100$ G) configuration.

the mesh of the EM module is made of 11350 tetrahedra, while the FLUID module mesh has 44000 hexahedra ($N_r = 170$, $N_z = 200$).

The power deposition distribution calculated by 3D-VIRTUS in the $B_0 = 0$ G configuration (see Fig. 2.8(a)) resembles the distribution of SEMS (see [59, Fig. 7]), in which the power deposition is localized under the the two antenna coils, and close to the edge of the discharge. In Fig. 2.8(b), the radial power deposition at the lower coil axial location has been depicted; the trend predicted by the two codes is the same, while the peak of the deposited power is exactly at the edge for 3D-VIRTUS, and close to the edge for SEMS. As for the $B_0 = 100$ G configuration, there is still a good agreement between 3D-VIRTUS

(see Fig. 2.9(a)) and SEMS for the power deposition distribution, though SEMS predict a weaker increase in the power deposition near the bulk of the discharge (see [59, Fig. 7]); in regards to the radial power deposition profile (see Fig. 2.9(b)), similar considerations as in the unmagnetised configurations hold true.

The density, and temperature distribution of the electron species as computed by 3D-VIRTUS in the unmagnetised (magnetised) case have been reported in Fig. 2.10 (Fig. 2.11). There is a good matching with the distribution evaluated by SEMS for the electron density (see [59, Figs.(9)]), and the electron temperature (see [59, Figs.(10)]). In the unmagnetised configuration, the density is peaked near the axis of the cylindrical source, whereas the maximum temperature is close to the edge of the discharge, and below the antenna coils; the maximum density (temperature) is 3.5×10^{17} m^{-3} (4 eV) in 3D-VIRTUS, while it can be inferred that the peak density (temperature) is approximately around 8.0×10^{17} m^{-3} (4 eV) in SEMS. In the magnetised configuration, the electron density, and electron temperature distributions of the two codes still show a good agreement; specifically, both codes predict two distinct density peaks in the cylindrical source, and the expansion chamber regions, respectively (see Fig. 2.11(a), and [59, Figs. (9)]), and an intense temperature region near the edge of the source, and between the two antenna coils (see Fig. 2.11(b), and [59, Figs. (10)]). The density (temperature) peak value is $n_e = 4.3 \times\ 10^{17}$ m^{-3} ($T_e = 3.6$ eV) in 3D-VIRTUS, while in SEMS around 8.0×10^{17} m^{-3} (4 eV). The differences in the power deposition, the electron density, and temperature between the two codes can be ascribed to: (i) the lack of information about the boundary conditions, and the plasma chemistry reactions that have been implemented in SEMS, (ii) the modelling of the RF antenna as an *assumed* current distribution in SEMS, while it is self-consistently *computed* in the EM module, and, ultimately, (iii) the numerical approaches the two codes resort on. Moreover, being the magneto-static field produced by electromagnets, namely assumed axisymmetric both in both codes, it does not seem that the differences in the power deposition distributions can be attributed to the 3D formulation of the EM problem in 3D-VIRTUS rather than the 2D formulation of SEMS. Despite the differences, both SEMS and 3D-VIRTUS predict similar distributions as the magneto-static field increases.

Validation against experimental measurements

To provide an independent validation of the new code against experimental data, 3D-VIRTUS has been compared against the measurement performed on a Piglet Helicon reactor [93]. Specifically, 3D-VIRTUS has been benchmarked against the electron density profiles measured on the axis of the Helicon discharge filled with argon gas. Measurements have been performed with a Langmuir probe aligned with the axis of the reactor which can be manoeuvred in order to sample the electron density in several axial positions.

The Helicon discharge has been produced by a Double Saddle antenna [114] driven at a 13.56 MHz frequency. A pair of electro-magnet coils surrounds the RF antenna and is employed to generate the confining magneto-static field; more specifically two configurations have been considered, namely magneto static field generated by *Source Coil* and *Exhaust Coil* (see [93, Fig. 1] for further details). The maximum intensity of the magneto-static field in both cases is $B_0 = 21$ G, the antenna input power $Pw = 250$ W, and the neutral background pressure $p_0 = 0.36$ Pa. The equilibrium electron density n_e, power depo-

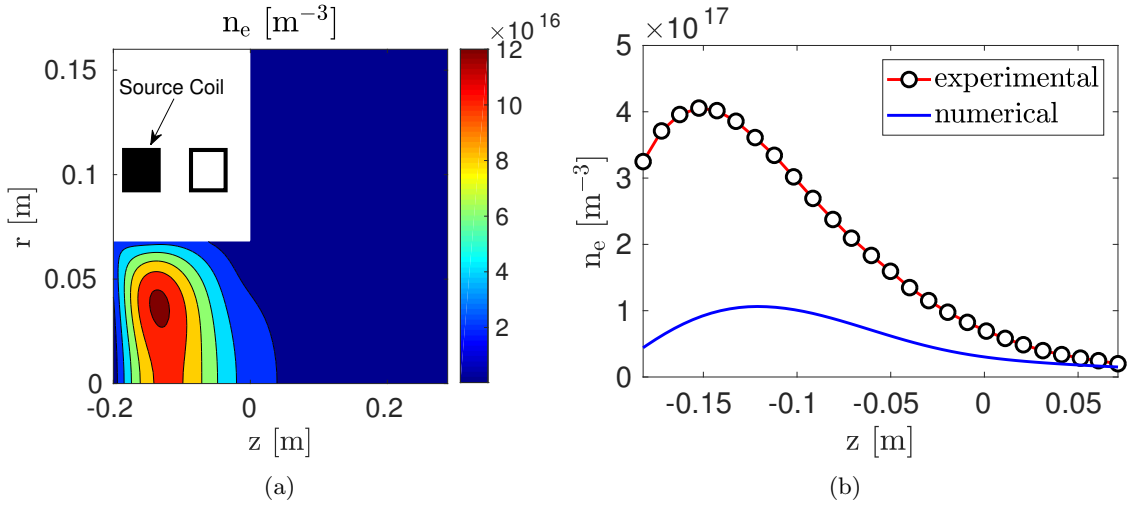

Figure 2.12: (a) The electron density distribution (n_e) calculated with 3D-VIRTUS, and (b) the electron density on the axis of the discharge, when the magneto-static field is generated by the *Source Coil*. Experimental data (open circles), 3D-VIRTUS output (solid line).

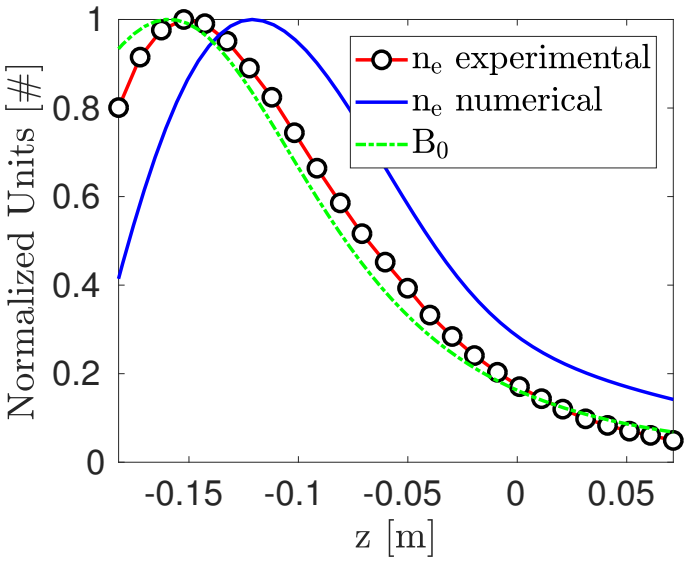

Figure 2.13: Normalized profiles of electron density (n_e) measured experimentally (open circles) and calculated numerically with 3D-VIRTUS (solid line), along with magneto-static field intensity on the axis of the discharge (dashed line); the magneto-static field is generated by the *Source Coil*.

sition $\mathcal{E}_{pow}$, and electron temperature T_e distributions have been solved by 3D-VIRTUS with prescribed threshold values $\epsilon_{F,max} = 10^{-5}$, and $\epsilon_{\max} = 10^{-1}$; besides, the mesh of the EM module is made of 9283 tetrahedra, while the FLUID module consists on a 2D mesh

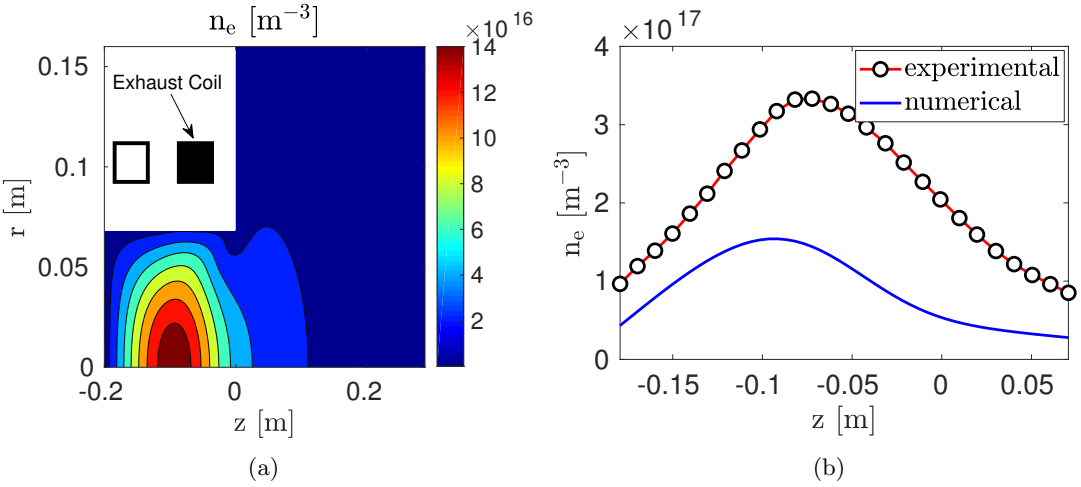

Figure 2.14: (a) The electron density distribution (n_e) calculated with 3D-VIRTUS, and (b) the electron density on the axis of the discharge, when the magneto-static field is generated by the *Exhaust Coil*. Experimental data (open circles), 3D-VIRTUS output (solid line).

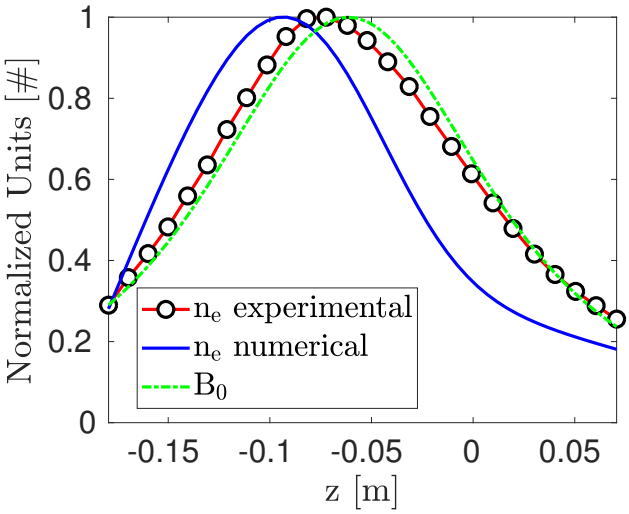

Figure 2.15: Normalized profiles of electron density (n_e) measured experimentally (open circles) and calculated numerically with 3D-VIRTUS (solid line), along with magneto-static field intensity on the axis of the discharge (dashed line); the magneto-static field is generated by the *Exhaust Coil*.

of 15000 hexahedra ($N_r = 75$, $N_z = 200$).

The electron density distribution calculated with 3D-VIRTUS in the *Source Coil* configuration (see Fig. 2.12(a)) is peaked in the source region (i.e., $z < 0$ m) under the active electromagnet and the antenna. In Fig. 2.12(b), the plasma density on the axis

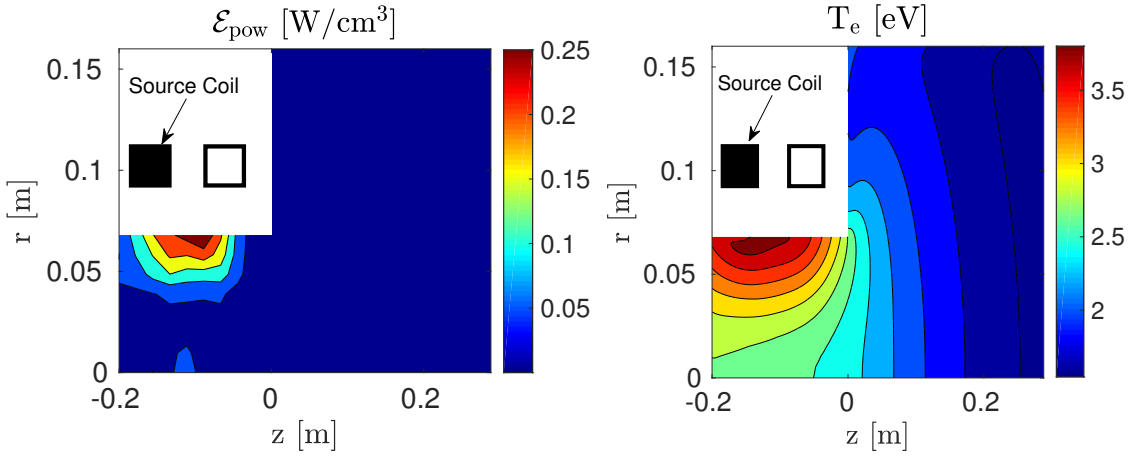

(a) (b)

Figure 2.16: The distribution of (a) the power deposition ($\mathcal{E}_{pow}$), and (b) the electron temperature (T_e) computed by 3D-VIRTUS when the magneto-static field is generated by the *Source Coil*.

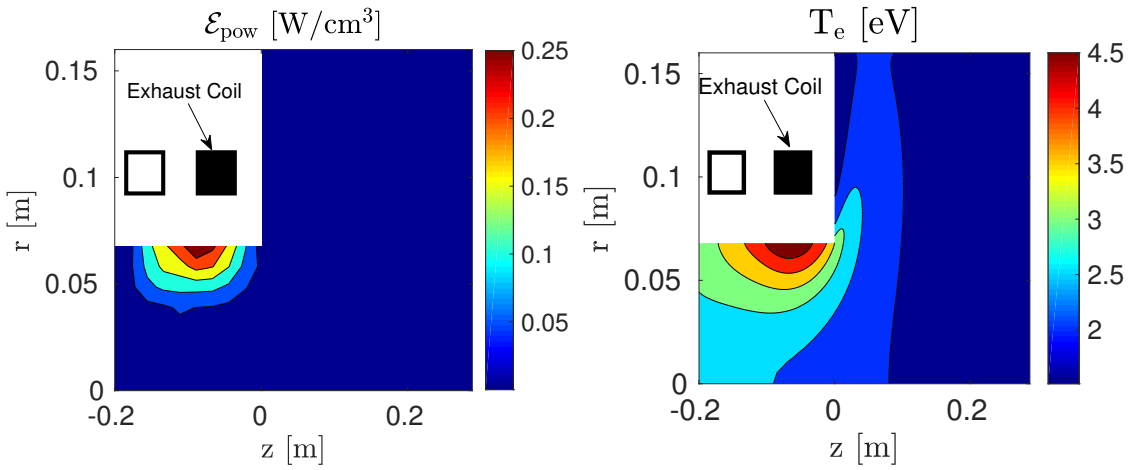

(a) (b)

Figure 2.17: The distribution of (a) the power deposition ($\mathcal{E}_{pow}$), and (b) the electron temperature (T_e) computed by 3D-VIRTUS when the magneto-static field is generated by the *Exhaust Coil*.

of the discharge has been depicted: the trend found experimentally is well reproduced by 3D-VIRTUS, moreover the intensity of the peak predicted numerically is roughly four times lower than the expected experimental value. In particular, comparing the normalized values of the numerical and experimental plasma density (see Fig. 2.13) an extremely well agreement can be appreciated: the numerical results reproduce the experimental one apart from a shift of the density peak of a few centimetres. Also the normalized magnetic field intensity has been reported in Fig. 2.13 (as done in [93, Fig. 8]) to highlight

the strong dependency between the latter and the shape of the electron density profile. Also in the *Exhaust Coil* configuration, the electron density distribution predicted by 3D-VIRTUS is peaked in the source region below the active electromagnet (see Fig. 2.14(a)). Moreover, the trend predicted numerically agrees very well with the experimental one (see Fig. 2.14(b) and Fig. 2.13) and the value of electron density peak calculated with 3D-VIRTUS is roughly half of the experimental one.

Also the power deposition and electron temperature distributions have been reported for both the *Source Coil* and the *Exhaust Coil* configurations (see respectively Figs. 2.16 and 2.17). In the reference paper [93] there are no data to benchmark these predictions, nonetheless the analysis of these results can give useful insights on the plasma behaviour in this reactor. The power deposition distribution is not significantly influenced by the magnetic topology: the power peak is located in the source region close to the edge of the discharge in both configurations (see Fig. 2.16(a) and Fig. 2.17(a)). More significant differences can be noticed on the electron temperature distribution (see Fig. 2.16(b) and Fig. 2.17(b)), in fact the peak position is located under the active electromagnet. Therefore, for these specific configurations, the magneto-static field topology influences much more the electron density and temperature profiles (i.e., the plasma transport) than the power deposition.

In conclusion, the numerical and experimental results show an excellent agreement, in fact: (i) the trend predicted numerically reproduces very well the experimental measurements, (ii) the quantitative differences between the numerical and experimental results can be in part attributed to the measurement uncertainty which, even though not reported in the reference paper [93], can be also exceed the 50% with a Langmuir probe [67]. Moreover it has been shown numerically that the magnetic topology affects much more the plasma transport than the power deposition.

2.3 HPT model

In order to predict the propulsive performances of a HPT, both the *Production Stage* and the *Acceleration Stage* (see Fig. 1.3) have to be modelled. In this work, the *Production Stage* has been solved by 3D-VIRTUS, while the *Acceleration Stage* by a plume model derived from a quasi one-dimensional analytical description of a HPT [42].

Analytical plume model

It is worthwhile to briefly illustrate the plume model, as reported on [42], before discussing its integration with 3D-VIRTUS. More specifically, the aim of [42] is to give a quasi-one dimensional, along the axis of the thruster, description of a HPT (i.e., both *Production Stage* and *Acceleration Stage*). For what concerns the modelling of the *Production Stage*, its principal outputs are the average plasma density n inside the source and the upstream plasma thrust at source outlet F_0 (i.e., the force produced by the plasma acceleration in absence of a magnetic nozzle). The latter is calculated assuming that: (i) the electrons inertia is negligible, (ii) the ions are cold, and (iii) at the source outlet the speed of both

ions and electrons is equal to the Bhom velocity u_B [37, Chap. 8]; therefore

$$F_0 = \left(M\Gamma u_B + \langle p_e \rangle\right) A_0 \tag{2.19}$$

where M is the ion mass, Γ is the ions flux at the source outlet (expressed in $\mathrm{m}^{-2}\mathrm{s}^{-1}$), $\langle p_e \rangle$ is the radially averaged electron pressure, and A_0 is the outlet section of the thruster. Eq. 2.19 can be rewritten as

$$F_0 = 2\beta q n T_e A_0 \tag{2.20}$$

where β is a dimensionless coefficient which accounts for plasma non uniformity, q is the elementary charge, and T_e the electron temperature (expressed in eV). In the region downstream the source outlet an additional thrust due to the magnetic nozzle F_{mag} is produced; therefore the total thrust provided by the plasma acceleration F_p is equal to

$$F_p = F_0 + F_{mag} \tag{2.21}$$

In particular F_{mag} is given as [44]

$$F_{mag} = \int_V J_\theta B_r dV \tag{2.22}$$

where B_r is the radial component of the magneto-static field, J_θ is the azimuthal plasma current, and V is the volume in which the magnetic nozzle effect is non-negligible. In particular, assuming the paraxial approximation $B_z(r,z) \approx B_z(0,z)$, Eq. 2.22 can be rewritten as [44]

$$F_{mag} = \int_{A_0}^{A} \langle p_e \rangle dA \tag{2.23}$$

where A is the area of the magnetic flux tube which determines the boundary of the magnetic nozzle region. Interestingly, the magnetic nozzle plays a similar role of a physical nozzle with the main difference that in the latter only the pressure at the walls impart a force, whereas in the former the force is determined by the average value of the pressure in the expansion volume. From the mass conservation and the momentum equations [42, Eqs. 28,29], Eq. 2.23 can be rewritten as

$$F_{mag} = F_0 \frac{(\mathcal{M}-1)^2}{2\mathcal{M}} \tag{2.24}$$

where $\mathcal{M} = v/u_B$ is the magnetic Mach number, and v is the plasma velocity. Therefore the thrust produced by the plasma acceleration becomes

$$F_p = F_0 + F_0 \frac{\left(\mathcal{M}-1\right)^2}{2\mathcal{M}} \tag{2.25}$$

Provided that, at some point downstream the source outlet, the plasma will not remain attached to the magnetic field indefinitely but will detach, the value of $\mathcal{M}$ to be adopted in Eq. 2.25 is $\mathcal{M}_{det}$, namely the magnetic Mach number at the detachment point. A very simplified criterion to determine the location of the detachment point is assuming that

the latter occurs when the ion gyroradius is equal to the radius of the plasma flow area defined by the diverging magnetic field. Therefore, $\mathcal{M}_{det}$ can be calculated solving

$$\frac{1}{2}\left(\mathcal{M}_{det}^2 - 1\right) - \ln \mathcal{M}_{det} = \ln\left(\frac{qB_0^2 A_0}{\pi M T_i}\right) \tag{2.26}$$

B_0 is the magnetic field at the source outlet, and T_i is the ion temperature (expressed in eV); it is worth recalling that Eq 2.26 is derived from the combination of continuity and momentum equations in the magnetic nozzle region [42, Eqs. 28,29]. Therefore the thrust provided by the plasma acceleration is

$$F_p = F_0 \frac{\mathcal{M}_{det}^2 + 1}{2\mathcal{M}_{det}} \tag{2.27}$$

In general the thrust T produced by a HPT is the sum of two contributions, namely the thrust produced by the acceleration of the plasma F_p, and of the neutral gas F_{gas}. The latter is derived from

$$F_{gas} = \dot{m}_0 v_g \left(1 + \frac{k_B T_g}{M v_g^2}\right) \tag{2.28}$$

where $\dot{m}_0$ is the input mass flow rate, k_B is the Boltzmann constant, T_g is the neutral gas temperature (expressed in K), $v_g = \sqrt{\gamma k_B T_g / M}$ is the speed of sound, and γ is the specific heat constant. Therefore, the thrust T provided by the HPT is

$$T = F_p + F_{gas} \tag{2.29}$$

and trivially the specific impulse I_{sp} is calculated as

$$I_{sp} = \frac{T}{g_0 \dot{m}_0} \tag{2.30}$$

where g_0 is the acceleration of gravity at the sea level.

In conclusion it is worth recalling that the above described plume model is extremely simplified, in fact

- The detachment point is determined with a very simplified criterion.
- Because of the paraxial approximation, the model describes properly only idealized magnetic nozzles.
- Magnetic nozzles in which magnetic cusps appears cannot be handled because the conservation equations as reported in [42] do not hold true.

Nonetheless, this model can be useful to preliminary estimate the thruster performances and, if coupled to an accurate model of the discharge chamber, to identify some parameters for the optimization of the latter.

Integration of the plume model and 3D-VIRTUS

The plume model has been integrated as it is (i.e., relying on the principal hypothesis assumed in [42]) with 3D-VIRTUS. In particular, the minor changes applied to the plume model in order to get coherent results with 3D-VIRTUS have been highlighted in the following, where the coupling strategy is described:

- The upstream plasma thrust F_0 is calculated after solving the discharge with 3D-VIRTUS. More specifically, Eq. 2.20 has been modified in order to account for the generic profiles of the electron density n_e and the electron temperature T_e provided by 3D-VIRTUS
$$F_0 = 2q \int n_e T_e dA \tag{2.31}$$
the integration is performed on the source outlet section.
- The thrust provided by the plasma F_p is obtained as prescribed by Eq. 2.27, although the B_0 value utilized in Eq. 2.26 is an averaged value of the magneto-static field intensity on the source outlet.
- The thrust provided by the neutral gas is calculated as prescribed by Eq. 2.28, nonetheless the neutral mass flow rate is calculated as
$$\dot{m}_0 = v_g \int (n_0 + n_s) dA \tag{2.32}$$
where n_0 is the neutral number density and n_s the excited number density.
- Finally, the thrust T and the specific impulse I_{sp} are calculated as prescribed respectively in Eq. 2.29 and Eq. 2.30.

A schematic of the methodology described is reported in Fig. 2.18.

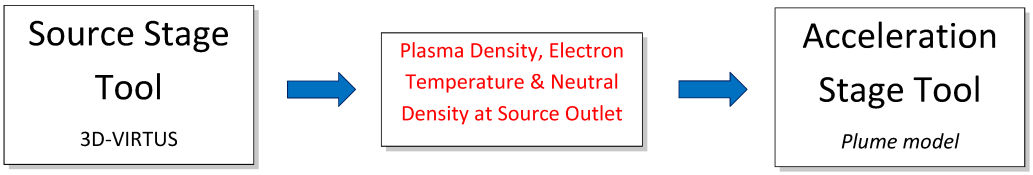

Figure 2.18: Scheme of the HPT simulation strategy.

Matching boundary conditions

In order to match the 3D-VIRTUS results with the assumptions done in the plume model, the boundary conditions at the source outlet have been modified in respect to what stated in Sec. 2.1. Both neutrals and excited are assumed to be at the speed of sound at the source outlet [42], therefore the excited (Γ_s) and neutral (Γ_0) fluxes are given by
$$\Gamma_s = v_g n_s \tag{2.33}$$

$$\Gamma_0 = v_g n_0 \tag{2.34}$$

where n_s and n_0 are respectively the excited and neutral number densities, $v_g = \sqrt{\gamma k_B T_0 / M}$ is the speed of sound, k_B is the Boltzmann constant, T_0 is the heavy species (i.e. ions, neutrals, and excited) temperature, M the heavy species mass, and γ is the ratio of specific heats. The boundary condition for the Poisson equation are derived from [42, Eq. 9]

$$\frac{\partial \phi}{\partial z} = \frac{T_e}{n_e} \frac{\partial n_e}{\partial z} \tag{2.35}$$

where ϕ is the plasma potential, and $\partial / \partial z$ is the derivative along the axis of the thruster.

Chapter 3

Numerical results

The capabilities of the new numerical code have been exploited to perform a numerical study on a simplified configuration of HPT. The aim of this analysis is not to identify the optimum design of a HPT, rather than it is intended to gain a preliminary insight on how the principal design parameters (e.g., geometry of the magneto-static field, of the antenna, and of the discharge chamber) affect the thruster behaviour. A parametric study has been conducted on a idealized HPT which relies on a cylindrical plasma discharge surrounded by four different magnetic topologies. The latter have been compared with respect to: (i) the equilibrium profiles of electron density (n_e), electron temperature (T_e), and power deposition ($\mathcal{E}_{pow}$) in the plasma discharge, (ii) the antenna parameters, namely the impedance (Z) and the current distribution over the conductors, along with (iii) the preliminary estimations of the attained thrust (T) and specific impulse (I_{sp}).

In particular, the magnetic topologies analysed are: (i) uniform magneto-static field (hereinafter referred as *Uniform*) because it has been usually assumed in theoretical works on HPTs [43], (ii) non-uniform magneto-static fields which, even though not particularly complex, are representative of magnetic configurations adopted in real-life experiments. The three non-uniform magnetic topologies analysed are generated by electromagnets, namely:

- Helmholtz coils [115, Chap. 5] (the associated magnetic field will be referred as *Helmholtz*), a similar configuration has been employed in prototypes realised at the Washington University [28]
- single coil (*Single Coil*) which is representative of the configuration adopted in prototypes realized at the Australian National University [20]
- pair of coaxial coils carrying currents in opposite directions (*Cusp*) that generate a magnetic cusp which is a typical feature of experiments involving permanent magnets (e.g., see [19])

The field lines of the four magnetic topologies considered, and the correspondent electromagnets (if present), are depicted in Fig. 3.1. All the electromagnets are coaxial to the discharge tube, have radius $R_c = 5$ cm, and both in the *Helmholtz* and the *Cusp* configurations the two coils are 5 cm-distant. Moreover, the non-uniform magnetic configurations

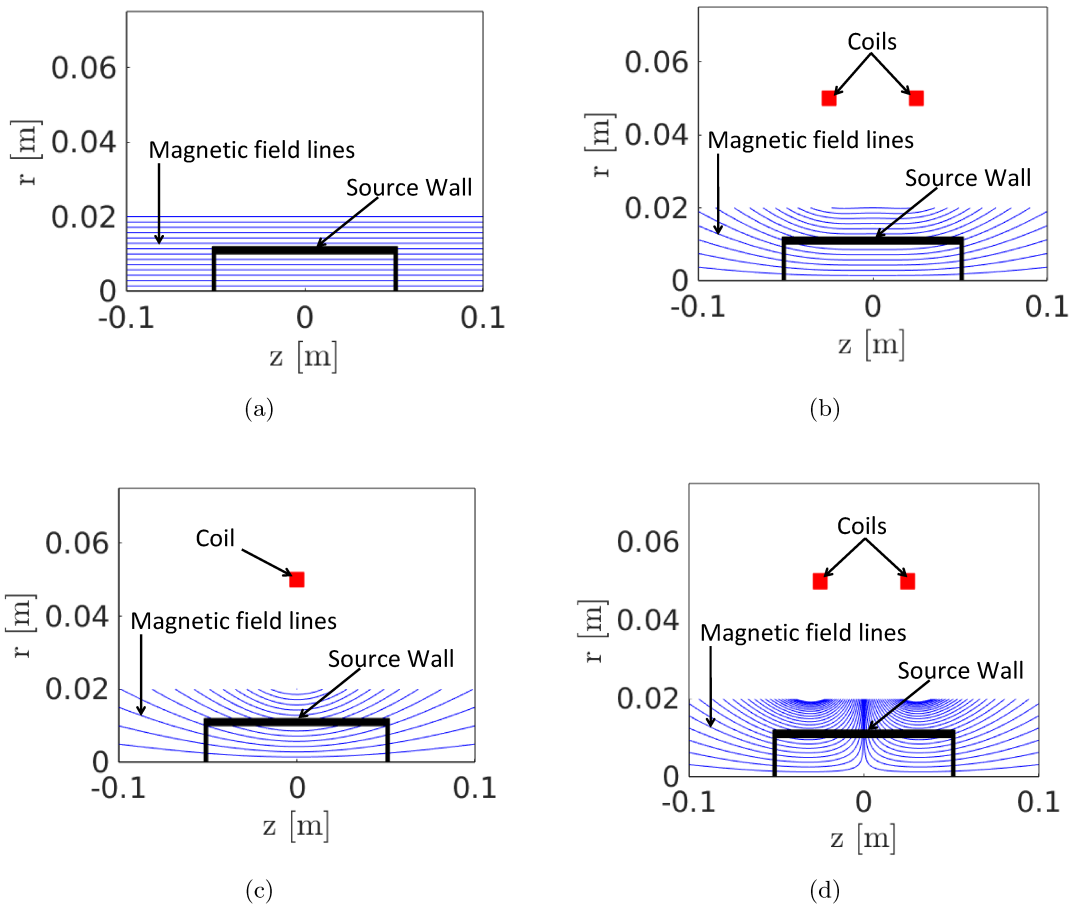

Figure 3.1: Schematic of the magneto-static field lines, the coils of the electromagnets (if present), and the walls of the cylindrical plasma source for: (a) *Uniform*, (b) *Helmholtz*, (c) *Single Coil*, and (d) *Cusp* magnetic topology.

have been chosen also to analyse how the system behaves when the magnetic topology gradually departs from the classically studied *Uniform* case. Specifically, the *Helmholtz* and the *Cusp* configurations present a moderate degree of non-uniformity (the former lower than the latter, see Fig. 3.1(b) and Fig. 3.1(c)). Instead, the *Cusp* configuration highly departs from the *Uniform* case because of the presence of a magnetic cusp region in which the axial magneto-static field is null (see Fig. 3.1(d) at $z = 0$ m).

The parametric study has been carried out in respect to a reference configuration of HPT (hereinafter referred as *Reference*) in which the plasma source comprises a cylindrical plasma column long $L = 10$ cm, whose radius is $R = 1$ cm, and filled with argon plasma. In particular, in the *Reference* configuration the initial neutral density is $n_0 = 10^{21}$ m^{-3}, the total amount of electric power deposited into the plasma is $Pw = 250$ W, and the maximum intensity of magneto-static field on the axis of the discharge is $B_0 = 500$ G (see the 2D map of the intensity in Fig. 3.2). Moreover, the source is driven by a Single Loop

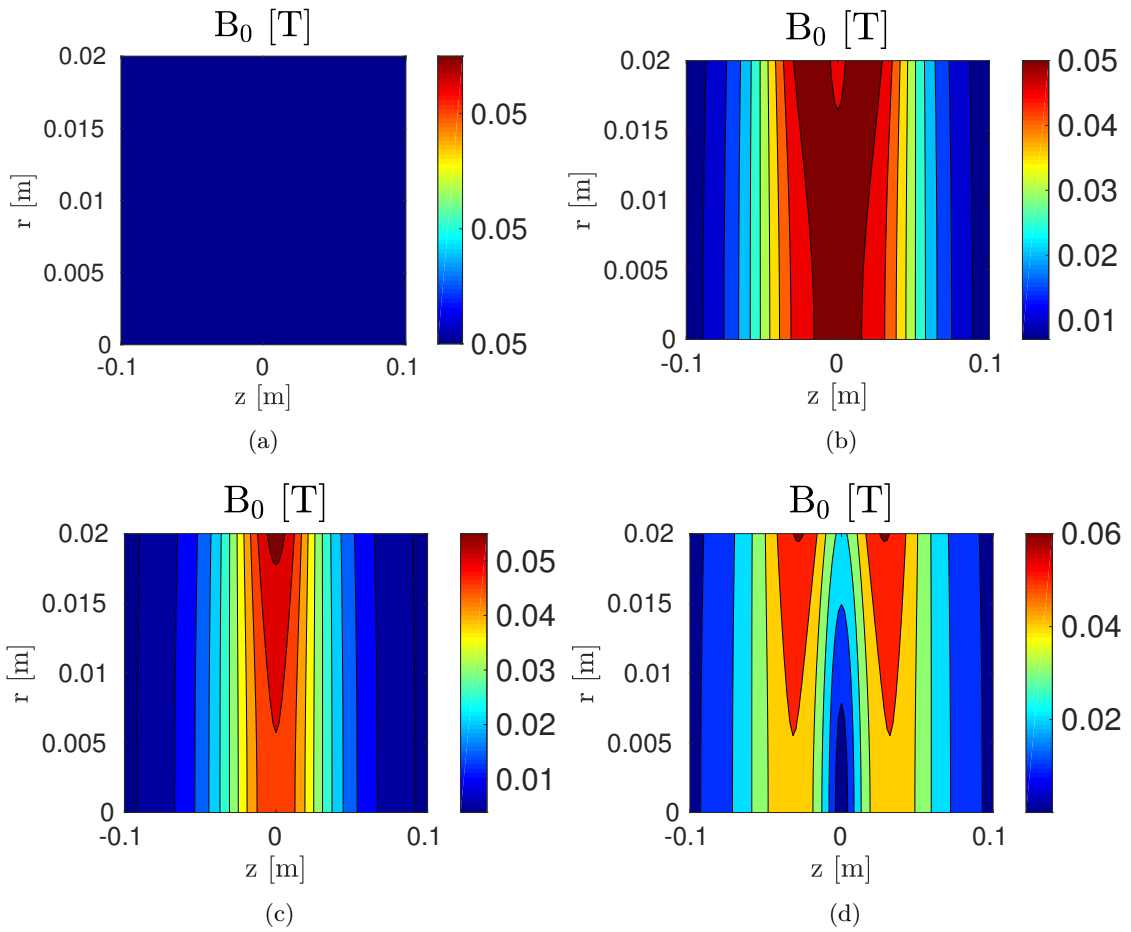

Figure 3.2: Intensity of the magneto-static field B_0 in function of the radial r and axial z position for: (a) *Uniform*, (b) *Helmholtz*, (c) *Single Coil*, and (d) *Cusp* magnetic topology.

antenna of radius $R_A = 3$ cm and width $w = 0.6$ cm (see Fig. 3.3). Subsequently, both the plasma parameters (i.e., n_0, B_0, and Pw) and the source geometry (i.e., L, R, and the antenna type) have been varied in order to evaluate their influence on the equilibrium conditions of the discharge. More specifically, each configuration examined in this study differs from the *Reference* for only one of the listed features so as to keep the analysis lucid. Instead, the parameters which are always kept constant are the symmetrical position of the antenna in respect to the centre of the plasma column, and the antenna excitation frequency $f = 13.56$ MHz. The latter is the typical frequency at which Helicon thrusters are operated during testing (e.g., see [19, 20, 22]).

From a numerical standpoint, the plasma transport problem has been formulated in a 2D-axisymmetric geometry in order to describe accurately the source while keeping the computational cost at bay. The 2D structured mesh of the FLUID module consists of approximately 25000 rectangles, while in the EM module the plasma is meshed with roughly 9000 tetrahedra; finally the *sampling grid* has 20 radial nodes and 7 axial nodes. A time step of 5×10^{-8} has been imposed in the solution of the plasma transport, and the

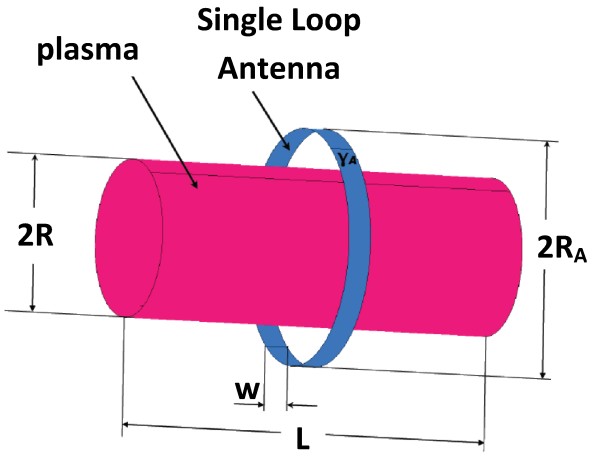

Figure 3.3: Schematic of the *Reference* Helicon sources driven by a Single Loop Antenna. Antenna dimensions: $R_A = 3$ cm, and $w = 0.6$ cm; plasma dimensions: $R = 1$ cm and $L = 10$ cm; plasma parameters: initial neutral density $n_0 = 10^{21}$ m^{-3}, total electric power deposited into the plasma $Pw = 250$ W, and maximum intensity of the magneto-static field on the axis of the discharge $B_0 = 500$ G.

achievement of the convergence has been stated when the relative error associated to the FLUID module is $\epsilon_{F,max} = 10^{-5}$ and to the iteration loop is $\epsilon_{max} = 10^{-1}$.

Finally, it is worth underlying that similar analyses (i.e., wide ranges of design parameters scanned relying on an accurate tool for the discharge chamber modelling) are not available in literature for HPTs. Therefore, the results presented in this chapter are intended to be a starting point for more detailed analyses on realistic HPTs.

3.1 Plasma discharge analysis

3.1.1 *Reference* case

The *Reference* case has been employed to preliminarily evaluate the effect of the magnetic topology on the equilibrium conditions of the discharge. As previously stated, the configurations analysed are *Uniform* (see Fig. 3.4), *Helmholtz* (see Fig. 3.5),*Single Coil* (see Fig. 3.6), and *Cusp* (see Fig. 3.7).

In the *Uniform* case, the electron density is peaked in correspondence of an intermediate radial position and has a very mild axial non-homogeneity (see Fig. 3.4(a)). As the non-uniformity of the magnetic topology increases, the electron density peak moves toward the axis of the discharge and the axial gradients become more intense (see progressively Fig. 3.5(a), Fig. 3.6(a) and Fig. 3.7(a)). Also the value of the electron density peak depends on the magnetic topology, and it is maximum in the *Uniform* and *Cusp* cases. It can be noticed that the contours of Figs. 3.4(a)-3.7(a) resembles the field lines of the associated magnetic topologies (see Figs. 3.1(a)-3.1(d)). This behaviour was expected

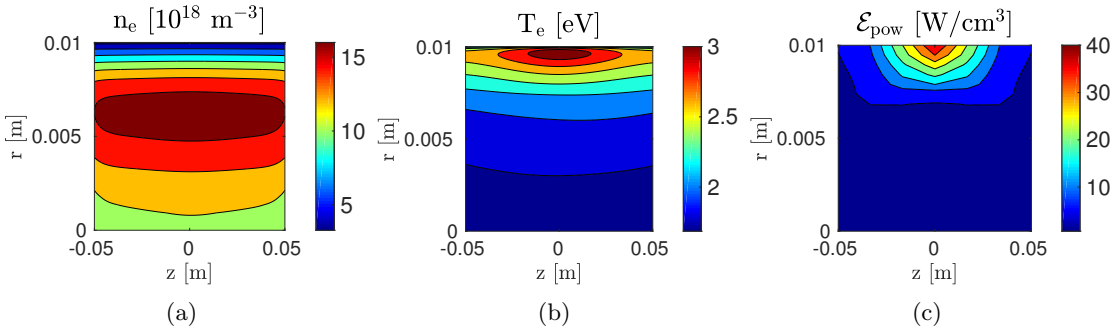

Figure 3.4: *Reference* source (see Fig. 3.3) surrounded by the *Uniform* magnetic topology; (a) electron density n_e, (b) electron temperature T_e, and (c) power deposition $\mathcal{E}_{pow}$ profiles expressed in function of the radial r and axial z position.

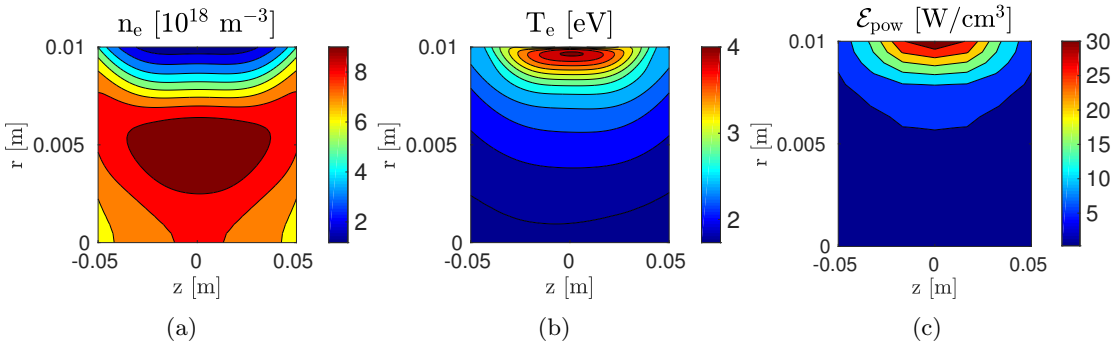

Figure 3.5: *Reference* source (see Fig. 3.3) surrounded by the *Helmholtz* magnetic topology; (a) electron density n_e, (b) electron temperature T_e, and (c) power deposition $\mathcal{E}_{pow}$ profiles expressed in function of the radial r and axial z position.

since the introduction of a magneto-static field results in a reduced rate of diffusion across the field lines, and in turn in steeper gradients of the plasma parameters in this very direction [37, Chap. 5].

The electron temperature is peaked in the edge of the discharge; more specifically in the *Uniform*, *Helmholtz*, and *Single Coil* cases the peak is below the antenna, while in the *Cusp* case there are two peaks below the electromagnets (see Figs. 3.4(b)-3.7(b)). The intensity of the electron temperature depends on the magnetic topology, and the maximum values are registered in the *Helmholtz* and *Single Coil* cases. The position of the electron temperature peaks is consistent with the dumping of TG waves which are confined near the edge of the discharge and propagate only in presence of a sufficiently intense quasi-axial magneto-static field [12]. The power deposition is always peaked under the antenna and close to the edge (see Figs. 3.4(c)-3.7(c)). In particular, the amount of power deposited in proximity of the axis of the discharge is much more intense in the *Cusp* case than in the other three configurations; in addition, also the lowest peak value is registered in this very case. It is worth recalling that total amount of power deposited into the discharge is fixed in this analysis (i.e., $Pw = 250$ W); therefore it is expected that the lower (higher)

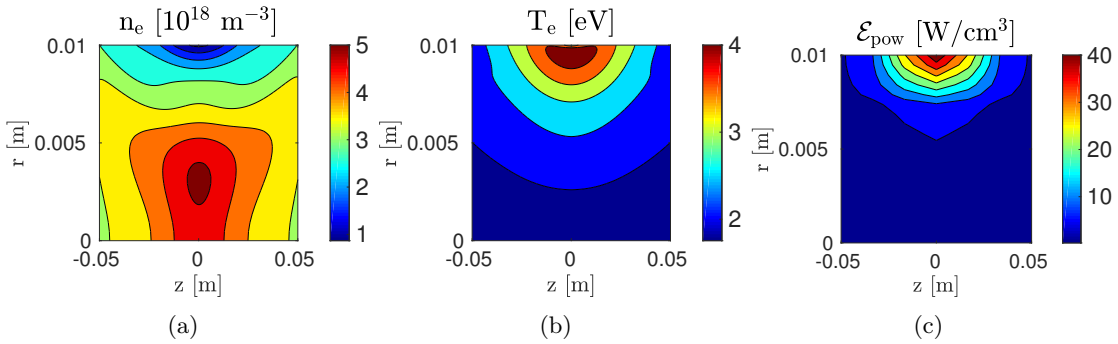

Figure 3.6: *Reference* source (see Fig. 3.3) surrounded by the *Single Coil* magnetic topology; (a) electron density n_e, (b) electron temperature T_e, and (c) power deposition $\mathcal{E}_{pow}$ profiles expressed in function of the radial r and axial z position.

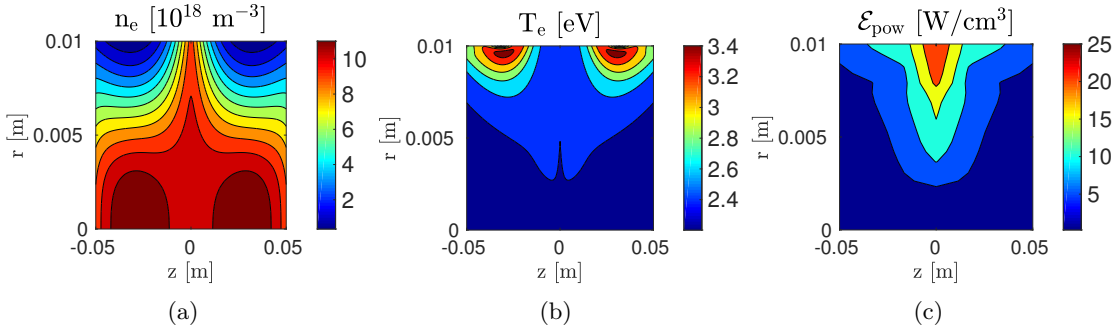

Figure 3.7: *Reference* source (see Fig. 3.3) surrounded by the *Cusp* magnetic topology; (a) electron density n_e, (b) electron temperature T_e, and (c) power deposition $\mathcal{E}_{pow}$ profiles expressed in function of the radial r and axial z position.

peak values are associated to the more (less) spread profiles.

In conclusion, the magnetic topology has a strong influence on the equilibrium profiles being both the plasma diffusion and the power deposition phenomena significantly affected by the geometry of the magneto-static field lines.

3.1.2 Effect of the intensity of the magneto-static field

The effect of the magneto-static field intensity on the equilibrium conditions of the discharge has been evaluated in the range from 0 G to 1000 G; the results of the *Helmholtz* magnetic topology has been utilised for this purpose. More specifically, the source has been studied for $B_0 = 0$ G (see Fig. 3.8), $B_0 = 250$ G (see Fig. 3.9), and $B_0 = 1000$ G (see Fig. 3.10); in addition the *Reference* case for $B_0 = 500$ G is depicted in Fig. 3.5. In absence of the magneto-static field, the electron density profile is centred and peaked on the axis of the discharge, and under the antenna as it would be in a ICP source [29, Chap. 12] (see Fig. 3.8(a)). As the magneto-static field increases the density peak spreads axially around the axis of the discharge, and gets greatly enhanced in magnitude as it

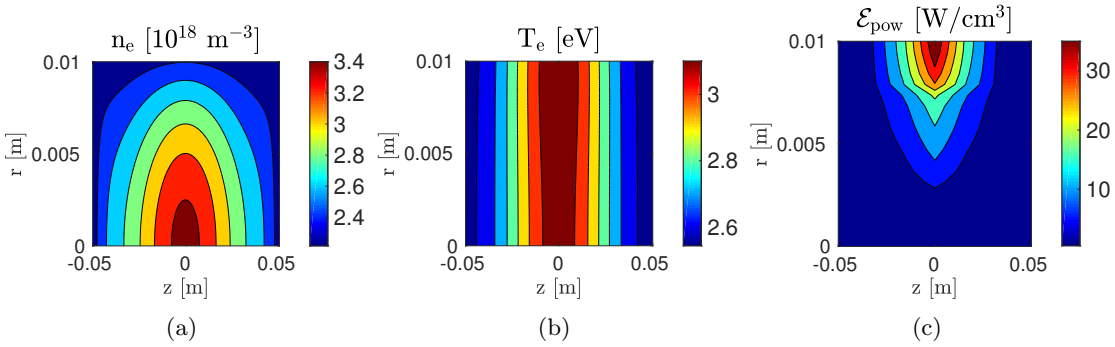

Figure 3.8: Intensity of the magneto-static field $B_0 = 0$ G, the other parameters as in the *Reference* (see Fig. 3.3), source surrounded by the *Helmholtz* magnetic topology; (a) electron density n_e, (b) electron temperature T_e, and (c) power deposition $\mathcal{E}_{pow}$ profiles expressed in function of the radial r and axial z position.

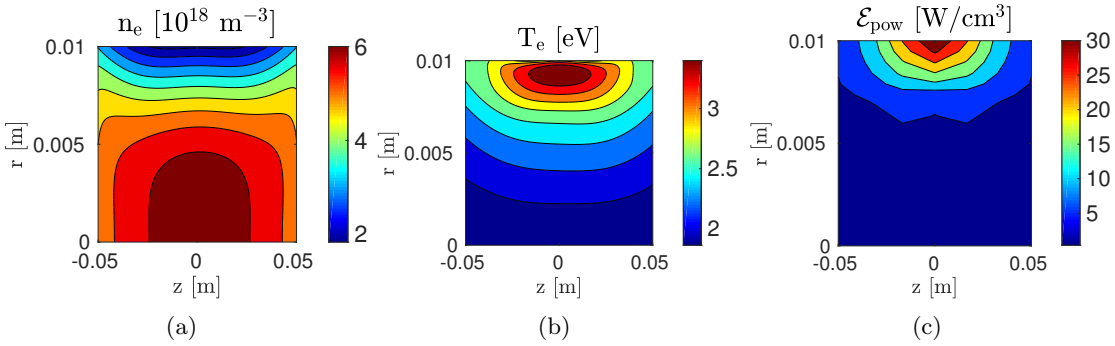

Figure 3.9: Intensity of the magneto-static field $B_0 = 250$ G, the other parameters as in the *Reference* (see Fig. 3.3), source surrounded by the *Helmholtz* magnetic topology; (a) electron density n_e, (b) electron temperature T_e, and (c) power deposition $\mathcal{E}_{pow}$ profiles expressed in function of the radial r and axial z position.

would be for a Helicon source (see progressively Fig. 3.9(a), Fig. 3.5(a), and Fig. 3.10(a)). Eventually, the density peak gets stronger, and moves toward the edge of the discharge for higher values of the magneto-static field (see Fig. 3.10(a)). As a result, the maximum value of the electron density increases of roughly four times from $B_0 = 0$ G to $B_0 = 1000$ G. The electron temperature profile is radially uniform, whereas it exhibits a weak variation along the axial direction in the unmagnetised configuration (see Fig. 3.8(b)). With the introduction of the magneto-static field, the electron temperature becomes predominantly inhomogeneous along the radial direction and the electron temperature peak moves close to the edge of the discharge; in addition the maximum temperature increases as the magnetic field does so (see Fig. 3.9(b), Fig. 3.5(b), and Fig. 3.10(b)). The power deposition profile is peaked under the antenna; it gets closer and closer to the edge of the discharge, as the magneto-static field increases in magnitude (see Figs. 3.8(c)-3.10(c) and Fig. 3.5(c)).

In general, for all the four magnetic topologies considered, a greater (lower) intensity

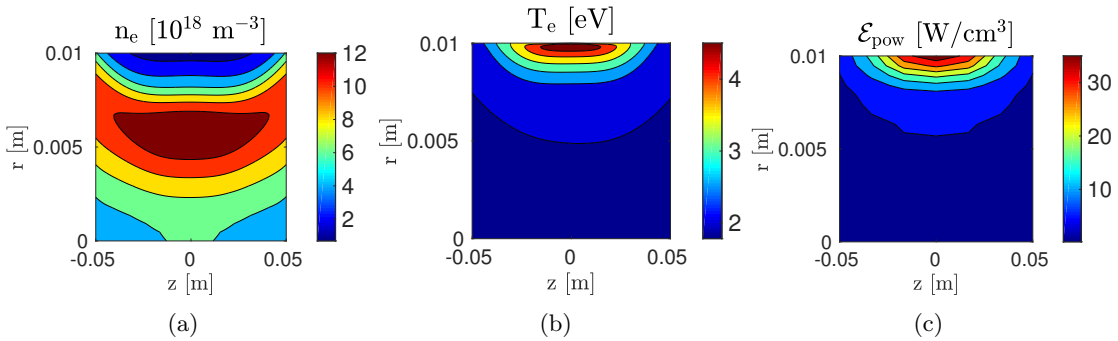

Figure 3.10: Intensity of the magneto-static field $B_0 = 1000$ G, the other parameters as in the *Reference* (see Fig. 3.3), source surrounded by the *Helmholtz* magnetic topology; (a) electron density n_e, (b) electron temperature T_e, and (c) power deposition $\mathcal{E}_{pow}$ profiles expressed in function of the radial r and axial z position.

of the magneto-static field results in: (i) the increase (decrease) of both the density and the temperature peaks, and (ii) the enhancement (diminishment) of the non-homogeneity of the plasma profiles in the direction perpendicular to the magneto-static field lines.

3.1.3 Effect of the initial neutral density

The effect of the initial neutral density has been evaluated in the range from 10^{20} m^{-3} to 10^{22} m^{-3}; the results of the *Uniform* magnetic topology has been utilised for this purpose. More specifically, the source has been studied for $n_0 = 10^{22}$ m^{-3} (see Fig. 3.11), and $n_0 = 10^{20}$ m^{-3} (see Fig. 3.12). In addition: (i) the *Reference* case for $n_0 = 10^{21}$ m^{-3} is depicted in Fig. 3.4, and (ii) also the $n_0 = 2 \times 10^{21}$ m^{-3}, and $n_0 = 5 \times 10^{20}$ m^{-3} cases have been studied but are not reported for the sake of brevity.

The electron density profile presents the same features of the unmagnetised case when $n_0 = 10^{22}$ m^{-3} (see Fig. 3.11(a)). As the neutral density decreases, the peak of the elec-

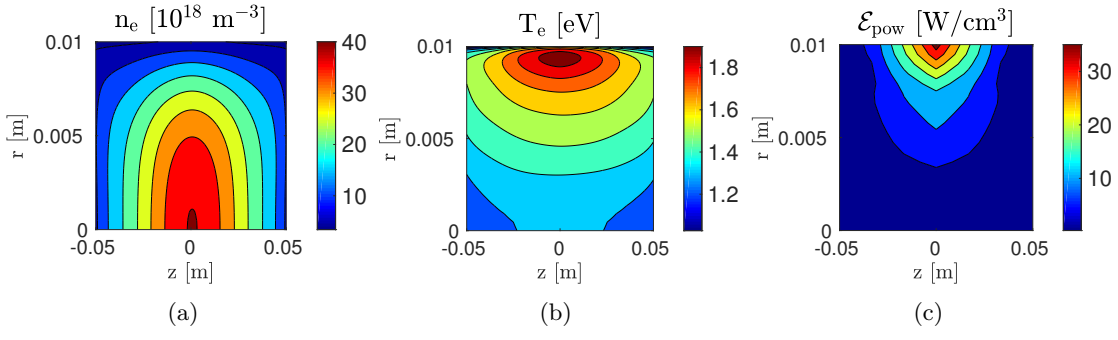

Figure 3.11: Initial neutral density $n_0 = 10^{22}$ m^{-3}, the other parameters as in the *Reference* (see Fig. 3.3), source surrounded by the *Uniform* magnetic topology; (a) electron density n_e, (b) electron temperature T_e, and (c) power deposition $\mathcal{E}_{pow}$ profiles expressed in function of the radial r and axial z position.

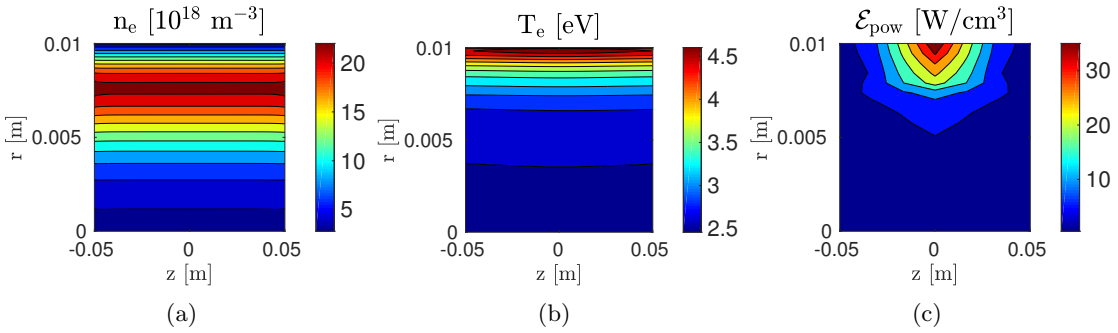

Figure 3.12: Initial neutral density $n_0 = 10^{20}$ m^{-3}, the other parameters as in the *Reference* (see Fig. 3.3), source surrounded by the *Uniform* magnetic topology; (a) electron density n_e, (b) electron temperature T_e, and (c) power deposition $\mathcal{E}_{pow}$ profiles expressed in function of the radial r and axial z position.

tron density spreads axially and moves toward the edge of the discharge (see progressively Fig. 3.4(a), and Fig. 3.12(a)). It was expected that the neutral density had a strong effect on the electron density profile; in fact, the influence of the magneto-static field on the plasma diffusion diminishes as the collisionality (i.e., the neutral density) increases [37, Chap. 5]. The electron temperature is significantly non-uniform along both the radial and the axial directions also when $n_0 = 10^{22}$ m^{-3} (see Fig. 3.11(b)). Moreover, as the neutral density decreases, the temperature peak moves closer to the edge of the discharge, spreads axially, and increases its value (see progressively Fig. 3.4(b) and Fig. 3.12(b)). Finally, the power deposition profile is not significantly affected by the value of the neutral density (see Fig. 3.11(c), Fig. 3.4(c) and Fig. 3.12(c)).

In general, for all the magnetic topologies analysed, the peak of the electron temperature is more (less) intense and closer to (more distant from) the edge of the discharge as the neutral density deceases (increases). The power deposition profile is not significantly influenced by the latter. Moreover, the electron density profile has features closer to the

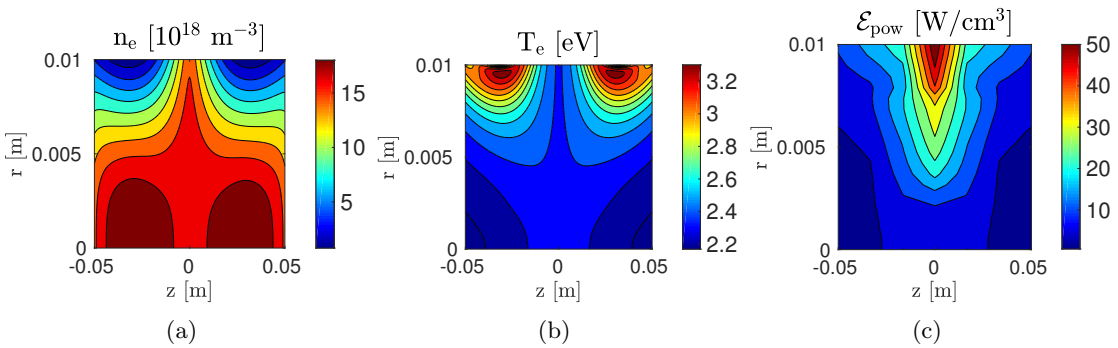

Figure 3.13: Total power $Pw = 500$ W, the other parameters as in the *Reference* (see Fig. 3.3), source surrounded by the *Cusp* magnetic topology; (a) electron density n_e, (b) electron temperature T_e, and (c) power deposition $\mathcal{E}_{pow}$ profiles expressed in function of the radial r and axial z position.

unmagnetised case as the neutral density increases, and conversely the non-uniformity in the direction perpendicular to the magnetic field lines is greatly enhanced as the neutral density decreases. Interestingly, the trend of the electron density peak varies with the magnetic topology: its value increases as the neutral density does so, apart from in the *Uniform* case where the trend is not monotonous.

3.1.4 Effect of the total power deposited into the plasma

The effect of the total power deposited has been evaluated in the range from 50 W to 500 W; the results of the *Cusp* magnetic topology has been utilised for this purpose. More specifically, the source has been studied for $Pw = 500$ W (see Fig. 3.13), $Pw = 100$ W (see Fig. 3.14), and $Pw = 50$ W (see Fig. 3.15); in addition the *Reference* case for $Pw = 250$ W is depicted in Fig. 3.7.

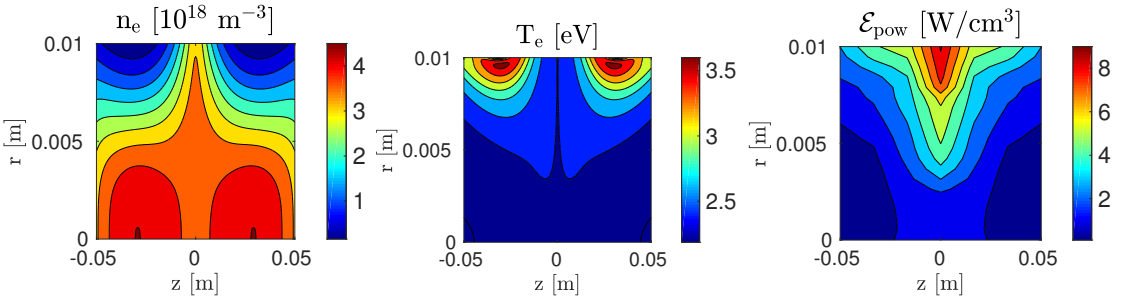

Figure 3.14: Total power $Pw = 100$ W, the other parameters as in the *Reference* (see Fig. 3.3), source surrounded by the *Cusp* magnetic topology; (a) electron density n_e, (b) electron temperature T_e, and (c) power deposition $\mathcal{E}_{pow}$ profiles expressed in function of the radial r and axial z position.

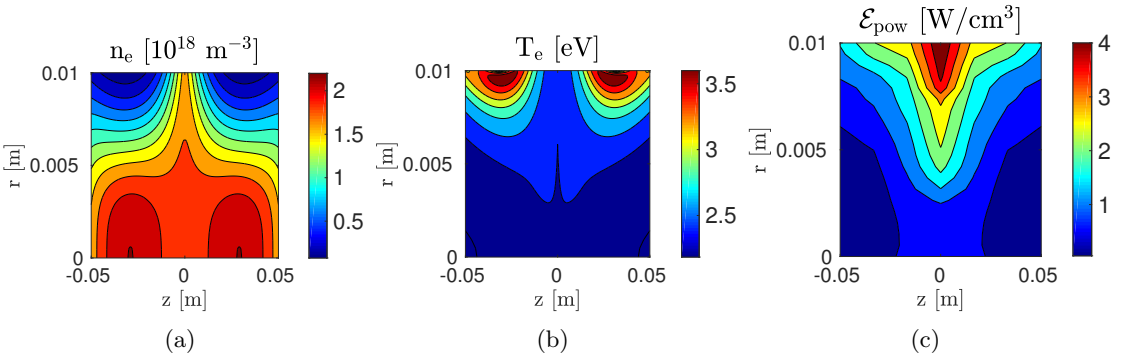

Figure 3.15: Total power $Pw = 50$ W, the other parameters as in the *Reference* (see Fig. 3.3), source surrounded by the *Cusp* magnetic topology; (a) electron density n_e, (b) electron temperature T_e, and (c) power deposition $\mathcal{E}_{pow}$ profiles expressed in function of the radial r and axial z position.

As the total power deposited increases (decreases), the value of electron density peak does so and the shape of the profile is not modified (see Figs. 3.13(a)-3.15(a) and Fig. 3.7(a)). The maximum electron density increases of roughly one order of magnitude passing from $Pw = 50$ W to $Pw = 500$ W. Also the shape of the electron temperature profile is not modified by variations of the total amount of power deposited; nonetheless as the total power increases (decreases), the electron temperature peak mildly decreases (increases) its value (see Figs. 3.13(b)-3.15(b) and Fig. 3.7(b)). Finally, the shape of the power deposition profile is not influenced by the total amount of power, and trivially the peak value is a linear function of the latter (see Figs. 3.13(c)-3.15(c) and Fig. 3.7(c)). The same trends hold true also for the other magnetic topologies analysed.

3.1.5 Effect of the antenna geometry

The effect of the antenna geometry has been evaluated comparing the equilibrium conditions reached when the discharge is driven by a Fractional Helix Antenna (in Fig. 3.16(a) the antenna geometry is depicted), a Nagoya Type-III Antenna (see Fig. 3.16(b)), and a Single Loop Antenna (*Reference* geometry depicted in Fig. 3.3). The results of the *Cusp* magnetic topology have been utilised for this purpose. More specifically, the equilibrium conditions achieved with the Fractional Helix Antenna are depicted in Fig. 3.17, with the Nagoya Type-III Antenna in Fig. 3.18, and with the Single Loop Antenna in Fig. 3.6. It is worth recalling that, as in the *Reference* case, the antenna radius is $R_A = 3$ cm, and the width $w = 0.6$ cm also for the Fractional Helix and the Nagoya Type-III; in addition the length of both antennae is $L_A = 5$ cm (see Fig. 3.16).

The electron density profile is peaked in correspondence of the axis of the discharge only if the system is driven by the Fractional Helix Antenna, or the Nagoya Type-III Antenna (see Fig. 3.17(a), Fig. 3.18(a), and Fig. 3.6(a)). In addition, in the Single Loop Antenna case the value of the electron density peak is roughly half than with the other two antennae. The electron temperature is not significantly influenced by the antenna

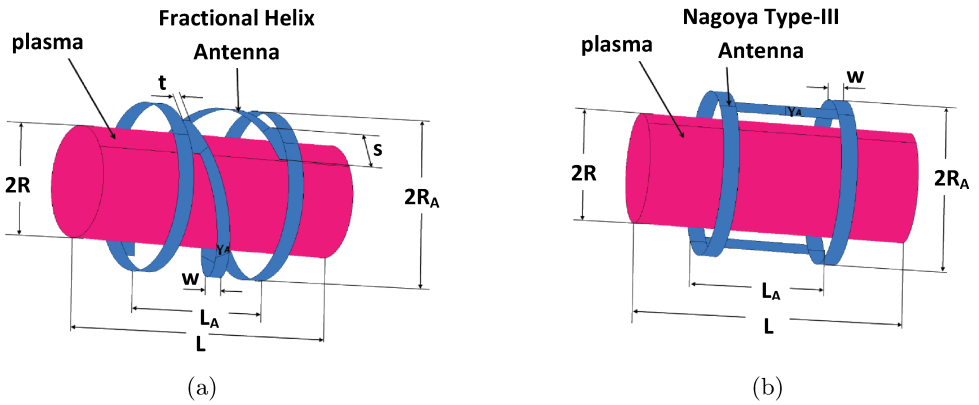

Figure 3.16: Schematic of Helicon sources driven by (a) Fractional Helix Antenna, and (b) Nagoya Type-III Antenna. Antenna dimensions: $R_A = 3$ cm, $w = 0.6$ cm, $L_A = 5$ cm, $s = 5w/2$, and $t = w/2$.

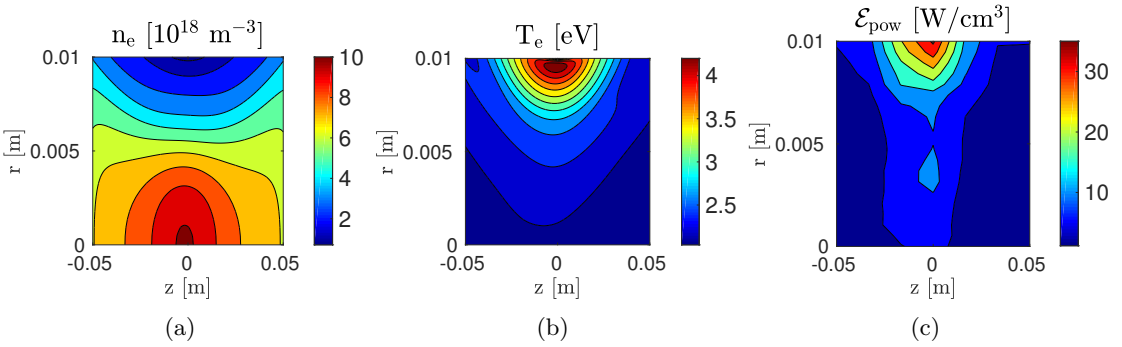

Figure 3.17: System driven by Fractional Antenna, the other parameters as in the *Reference* (see Fig. 3.3), source surrounded by the *Single Coil* magnetic topology; (a) electron density n_e, (b) electron temperature T_e, and (c) power deposition $\mathcal{E}_{pow}$ profiles expressed in function of the radial r and axial z position.

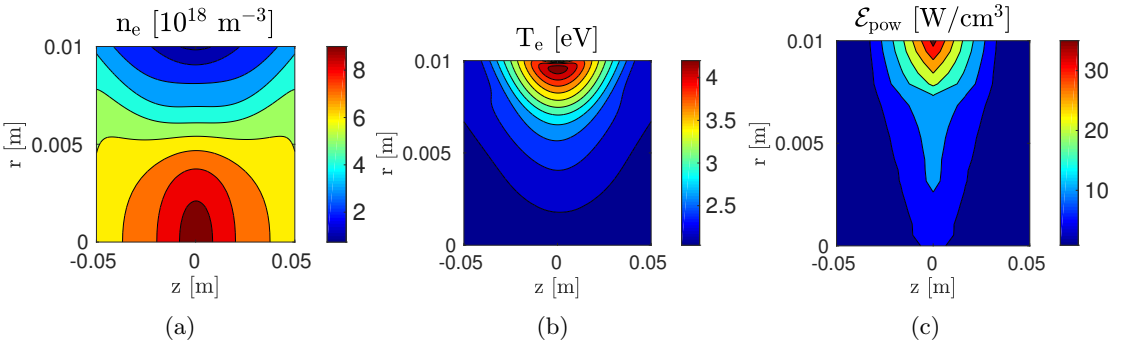

Figure 3.18: System driven by Nagoya Type-III Antenna, the other parameters as in the *Reference* (see Fig. 3.3), source surrounded by the *Single Coil* magnetic topology; (a) electron density n_e, (b) electron temperature T_e, and (c) power deposition $\mathcal{E}_{pow}$ profiles expressed in function of the radial r and axial z position.

geometry (see Fig. 3.17(b), Fig. 3.18(b), and Fig. 3.6(b)); only in the Fractional Helix Antenna case this very profile is mildly asymmetric. On the contrary, the power deposition depends on the antenna: the amount of power deposited in the centre of the discharge is more intense in the Fractional Helix Antenna and Nagoya Type-III Antenna cases than in the *Reference* (see Fig. 3.17(c), Fig. 3.18(c), and Fig. 3.6(c)). Moreover, if the system is driven by Fractional Helix Antenna, a mild asymmetry is noticed also in the power deposition profile. Nonetheless, this behaviour have been found also in experiments in which Fractional Helix Antenna have produced asymmetric plasma profiles [116]. Finally, it can be noticed that the increase of the electron density peak and its translation closer to the axis of the source in the Fractional Helix and Nagoya Type-III cases, is associated to a higher amount of power deposited in the core of the discharge.

The same trends hold true also for the other magnetic topologies: the plasma density peak is more intense and closer to the discharge axis with Fractional Helix Antenna and

Nagoya Type-III Antenna; in the same cases, the amount of power deposited in the core of the discharge is higher in respect to the *Reference*.

3.1.6 Effect of the discharge radius

The effect of the dimension of the discharge radius has been evaluated in the range from 0.5 cm to 2 cm; the results of the *Helmholtz* magnetic topology has been utilised for this purpose. More specifically, the source has been studied for $R = 0.5$ cm (see Fig. 3.19), and $R = 2$ cm (see Fig. 3.20); in addition the *Reference* case for $R = 1$ cm is depicted in Fig. 3.5.

The electron density profile is peaked on the axis of the discharge if $R = 0.5$ cm (see Fig. 3.19(a)). Similarly, the electron temperature peak moves closer to (more distant from) the edge as the radius grows (diminishes), but its value varies mildly and non-

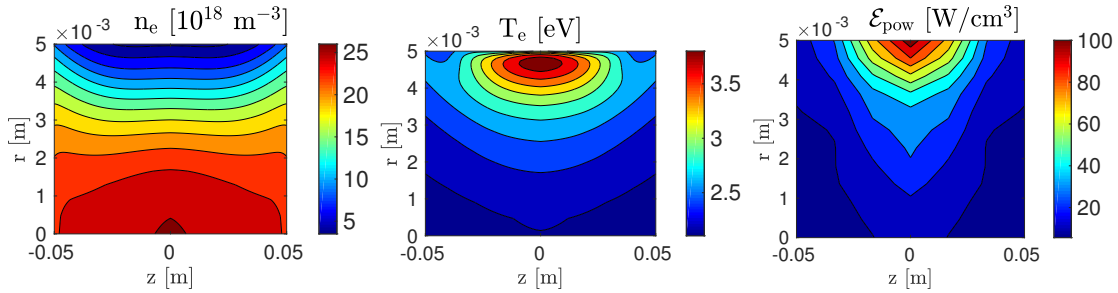

Figure 3.19: Discharge radius $R = 0.5$ cm, the other parameters as in the *Reference* (see Fig. 3.3), source surrounded by the *Helmholtz* magnetic topology; (a) electron density n_e, (b) electron temperature T_e, and (c) power deposition $\mathcal{E}_{pow}$ profiles expressed in function of the radial r and axial z position.

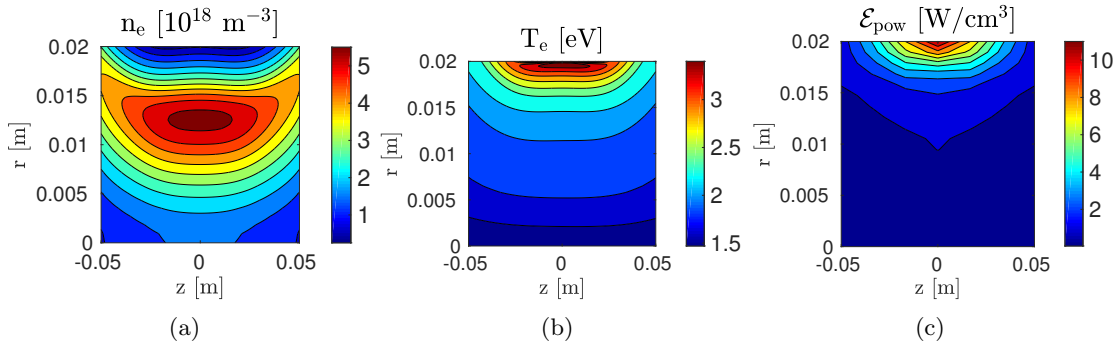

Figure 3.20: Discharge radius $R = 2$ cm, the other parameters as in the *Refernce* (see Fig. 3.3), source surrounded by the *Helmholtz* magnetic topology; (a) electron density n_e, (b) electron temperature T_e, and (c) power deposition $\mathcal{E}_{pow}$ profiles expressed in function of the radial r and axial z position.

monotonously (see Fig. 3.19(b), Fig. 3.5(b), and Fig. 3.20(b)). The power deposition profile is significantly influenced by the dimension of the discharge radius: (i) to smaller (bigger) radius is associated a higher (lower) peak value, and (ii) the amount of power deposited in the centre of the discharge increases as the radius becomes smaller (see Fig. 3.19(c), Fig. 3.5(c), and Fig. 3.20(c)). Point (i) can be explained considering that the total amount of power deposited is kept constant on this analysis (i.e., $Pw = 250$ W), therefore smaller (bigger) is the volume of the discharge tube, higher (lower) is the power per unit volume. Instead from point (ii), it can be inferred that the waves are mainly damped in a superficial region of the plasma column (coherently with the TG waves dynamics [12]). Therefore as the radius grows, the region where the damping, and in turn the power deposition, is important moves away from the centre of the discharge. Notably, the higher intensity of the electron density peak is obtained when the deposited power per unit volume is maximum.

The same features are reproduced also for the other magnetic topologies: increase (decrease) of both the electron density and power deposition peaks as the radius of the discharge grows (diminishes).

3.1.7 Effect of the discharge length

The effect of the dimension of the discharge length has been evaluated in the range from 5 cm to 20 cm; the results of the *Uniform* magnetic topology has been utilised for this purpose. More specifically, the source has been studied for $L = 5$ cm (see Fig. 3.21), and $L = 20$ cm (see Fig. 3.22); in addition the *Reference* case for $L = 10$ cm is depicted in Fig. 3.4.

For the lower values of the discharge length (i.e., $L = 5$ cm) the plasma density profile is not significantly modified in respect to the *Reference* case, only the value of the peak is slightly increased (see Fig. 3.21(a) and Fig. 3.4(a)). The electron temperature profile is more axially uniform for lower values of the discharge length, while the peak value is almost unaltered (see Fig. 3.21(b) and Fig. 3.4(b)). Also the power deposition profile is

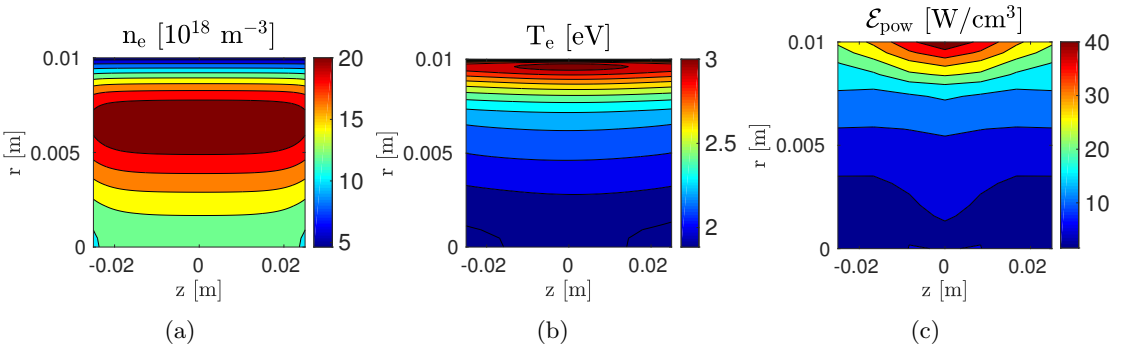

Figure 3.21: Discharge length $L = 5$ cm, the other parameters as in the *Refernce* (see Fig. 3.3), source surrounded by the *Uniform* magnetic topology; (a) electron density n_e, (b) electron temperature T_e, and (c) power deposition $\mathcal{E}_{pow}$ profiles expressed in function of the radial r and axial z position.

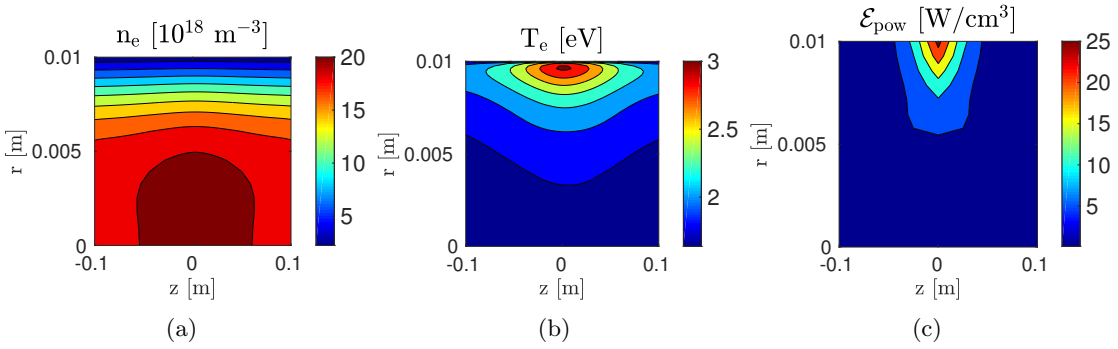

Figure 3.22: Discharge length $L = 20$ cm, the other parameters as in the *Refernce* (see Fig. 3.3), source surrounded by the *Uniform* magnetic topology; (a) electron density n_e, (b) electron temperature T_e, and (c) power deposition $\mathcal{E}_{pow}$ profiles expressed in function of the radial r and axial z position.

more uniform in respect to the *Reference* case, but the peak value is significantly increased (see Fig. 3.21(c) and Fig. 3.4(c)); the latter effect is only due to the fixed amount of power which has been assumed in this analysis (i.e., $Pw = 250$ W). Interestingly, similar trend for the electron temperature and power deposition profiles are registered also for the other magnetic topologies. Similarly, the intensity of the electron density peak increases in each case, but more significantly for the *Helmholtz* and *Single Coil* configurations (see Fig. 3.23). In fact in these two cases, the higher uniformity of the magneto-static field is registered in the centre of the source (see Fig. 3.1(b) and Fig. 3.1(c)); therefore if the discharge length is reduced, the system resembles much more to the *Uniform* case. On the contrary, in the *Cusp* case the non-uniformity of the magneto-static field is maximum in the centre of the discharge, in correspondence of the cusp region (see Fig. 3.2(d)).

For the higher values of the discharge length (i.e., $L = 20$ cm) the electron density peak is located close to the axis of the discharge and its intensity is slightly increased in

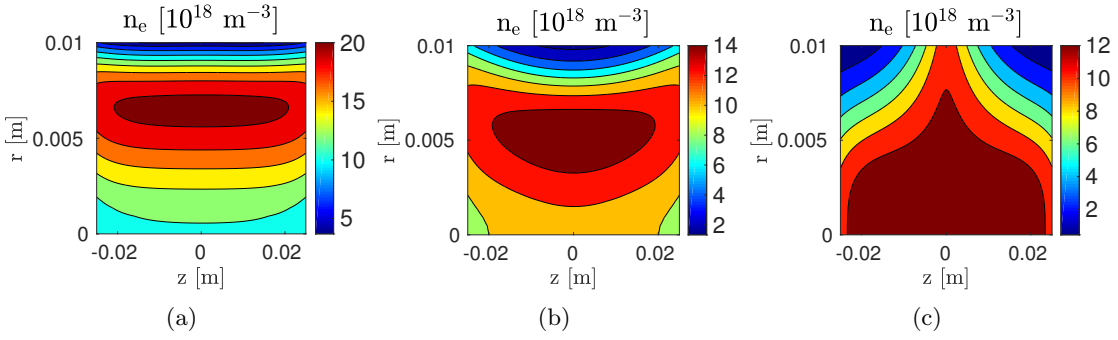

Figure 3.23: Discharge length $L = 5$ cm, the other parameters as in the *Refernce* (see Fig. 3.3); electron density profile n_e expressed in function of the radial r and axial z position. Source surrounded by (a) *Helmholtz*, (b) *Single Coil*, and (c) *Cusp* magnetic topology.

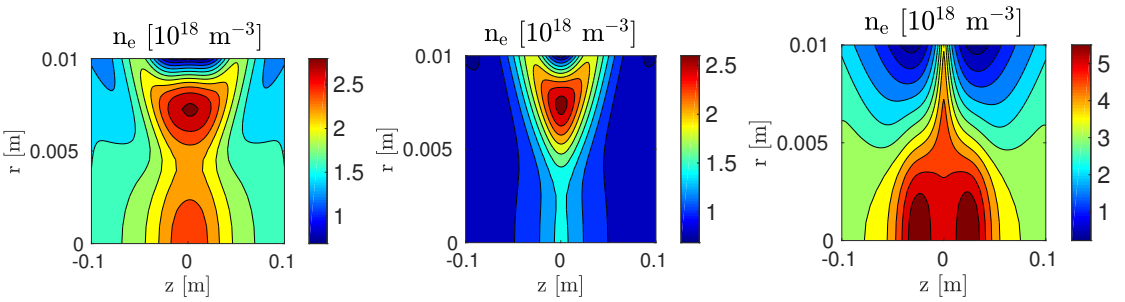

Figure 3.24: Discharge length $L = 20$ cm, the other parameters as in the *Refernce* (see Fig. 3.3); electron density profile n_e expressed in function of the radial r and axial z position. Source surrounded by (a) *Helmholtz*, (b) *Single Coil*, and (c) *Cusp* magnetic topology.

respect to the *Reference* (see Fig. 3.22(a) and Fig. 3.4(a)). Also the maximum value of the electron temperature profile is almost unaltered, but the axial uniformity decreases in respect to the *Reference* (see Fig. 3.22(b) and Fig. 3.4(b)). The power deposition profile has a lower axial uniformity and the peak value is decreased (see Fig. 3.22(c) and Fig. 3.4(c)). Similar trends of the electron temperature and the power deposition profiles have been found also for the other magnetic topologies. Instead, for what concerns the electron density profile: (i) the intensity of the peak decreases in all the configurations apart from the *Uniform*, and (ii) the profiles are significantly non uniform in the axial direction apart in the *Uniform* case (compare Fig. 3.22(a) and Fig. 3.24). Nonetheless, for $L = 20$ cm a different behaviour of the *Uniform* configuration was expected being, at the edge of the source, the intensity of the magneto-static field roughly one order of magnitude higher than in the other cases (see Fig. 3.2 for $z = \pm 10$ cm).

3.2 Antenna analysis

3.2.1 Antenna impedance

One of the most interesting features of the EM module of 3D-VIRTUS is the capability to accurately evaluate the real $\mathrm{Re}(Z)$ and the imaginary $\mathrm{Im}(Z)$ parts of the antenna impedance, which are crucial for the design of the feeding and matching network.

Higher (lower) values of the real part of the plasma impedance are in general associated to higher (lower) intensities of the magneto-static field (see Fig. 3.25(a)). The result is in good agreement with previous analyses [117] which highlighted that in a uniform discharge the antenna impedance is strongly influenced by both the intensity of the magneto-static field and the value of the plasma density. Clearly, the latter parameters are intimately related in a self-consistent model (see Sec. 3.1.2). Higher (lower) values of the real part of the antenna impedance are associated to higher (lower) neutral densities (see Fig. 3.25(b)). Interestingly, it was proven [117] that the value of the neutral density does not particularly affect the plasma impedance. Nonetheless, the present result is still in

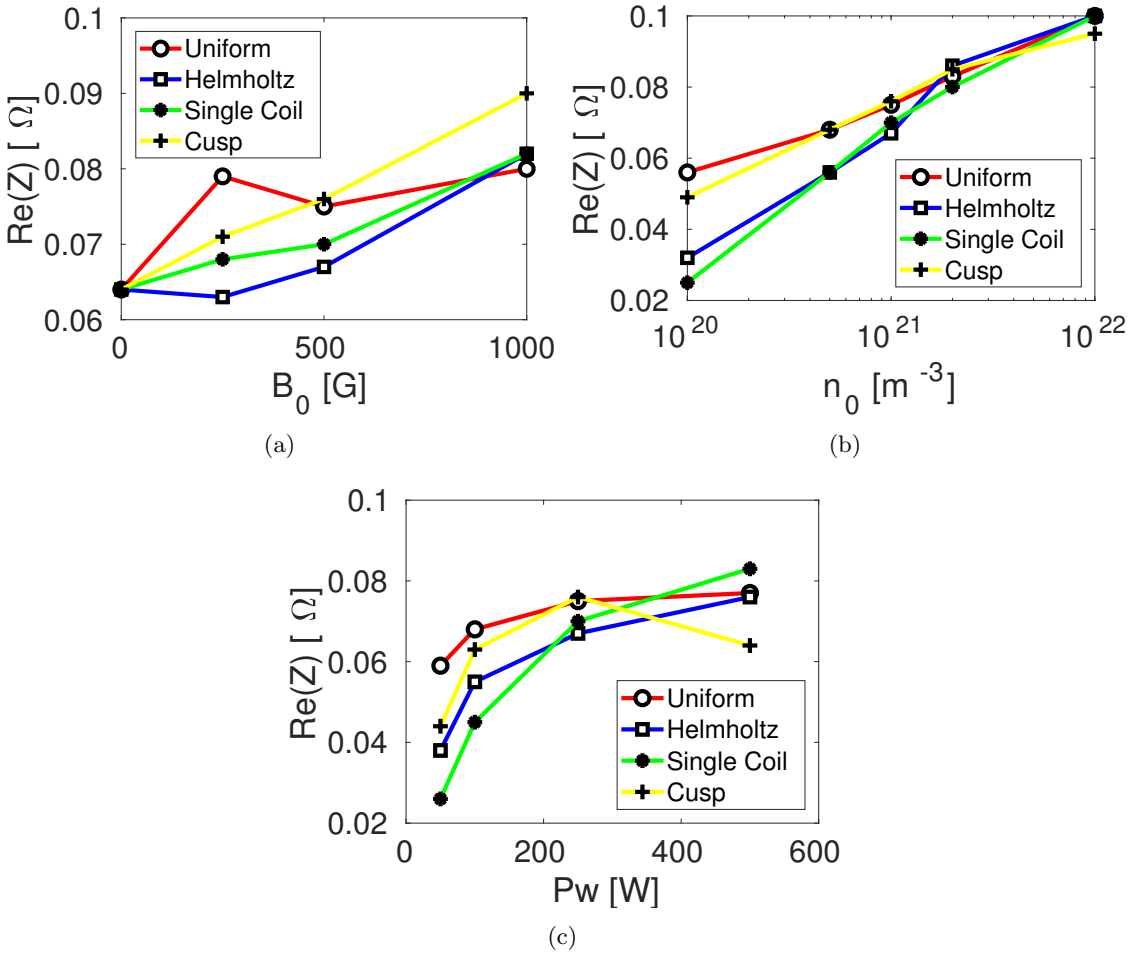

Figure 3.25: Real Re(Z) part of the antenna impedance as a function of (a) the intensity of the magneto-static field B_0, (b) the initial neutral density n_0, and (c) the power deposited Pw for a discharge surrounded by *Uniform*, *Helmholtz*, *Single Coil*, and *Cusp* magnetic topologies. The other parameters of the source are as in the *Reference* (see Fig. 3.3).

agreement with [117] considering that the plasma density varies with the neutral density (see Sec. 3.1.3). Higher (lower) values of the real part of the plasma impedance are in general associated to higher (lower) total powers (see Fig. 3.25(c)). Also in this case, the result is in agreement with [117] being the plasma density related to the deposited power (see Sec. 3.1.4). Higher values of the real and imaginary parts of the antenna impedance are respectively associated to the *Reference* Single Loop Antenna and the Fractional Helix Antenna (see Table 3.1). This result is still in agreement with [117] where it was proven that the antenna geometry has a strong influence on the impedance also if the plasma parameters are kept constant. Considerably higher (lower) values of the real part of the plasma impedance are associated to higher (lower) values of the source radius (see Fig. 3.26(a)). On the contrary, the real part of the antenna impedance does not have a monotonous relation with the source length: lower values are in general associated to

Antenna		*Single Loop*	*Nagoya Type-III*	*Fractional Helix*
Uniform	$\mathrm{Re}(Z)$ [Ω]	7.5×10^{-2}	7.6×10^{-2}	4.8×10^{-2}
	$\mathrm{Im}(Z)$ [Ω]	1.0×10^{1}	1.2×10^{1}	8.5×10^{0}
Helmholtz	$\mathrm{Re}(Z)$ [Ω]	6.7×10^{-2}	6.4×10^{-2}	3.6×10^{-2}
	$\mathrm{Im}(Z)$ [Ω]	1.0×10^{1}	1.2×10^{1}	8.5×10^{0}
Single Coil	$\mathrm{Re}(Z)$ [Ω]	7.0×10^{-2}	5.4×10^{-2}	2.3×10^{-2}
	$\mathrm{Im}(Z)$ [Ω]	1.0×10^{1}	1.2×10^{1}	8.5×10^{0}
Cusp	$\mathrm{Re}(Z)$ [Ω]	7.6×10^{-2}	2.1×10^{-2}	1.5×10^{-2}
	$\mathrm{Im}(Z)$ [Ω]	1.0×10^{1}	1.2×10^{1}	8.5×10^{0}

Table 3.1: Real $\mathrm{Re}(Z)$ and imaginary $\mathrm{Im}(Z)$ part of the antenna impedance for a discharge driven by *Single Loop*, *Nagoya Type-III*, and *Fractional Helix* antennas, along with surrounded by *Uniform*, *Helmholtz*, *Single Coil*, and *Cusp* magnetic topologies. The other parametes of the source are as in the *Reference* (see Fig. 3.3).

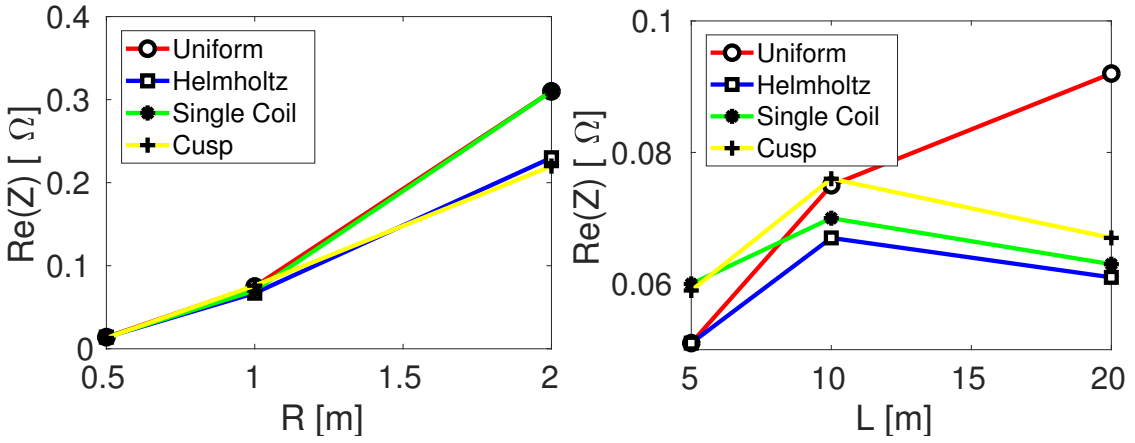

Figure 3.26: Real $\mathrm{Re}(Z)$ part of the antenna impedance as a function of (a) the discharge radius R and (b) the discharge length L for a discharge surrounded by *Uniform*, *Helmholtz*, *Single Coil*, and *Cusp* magnetic topologies. The other parametes of the source are as in the *Reference* (see Fig. 3.3).

both the $L = 5$ cm and $L = 20$ cm cases in respect to the *Reference* (see Fig. 3.26(b)). Finally, a higher value of the impedance is in general associated to the *Uniform* magnetic topology, and the only parameter which influences the imaginary part of the impedance is the antenna geometry (see Table 3.1).

3.2.2 Antenna current distribution

The current distribution over the conductors of the three antennas (i.e., Single Loop, Nagoya Type-III, and Fractional Helix) has been reported in Fig. 3.27. It is worth recalling that this very field is self-consistently calculated in the EM module of 3D-VIRTUS and not assumed a-priori. More specifically, the linear colour bar of Fig. 3.27 has been normalized in respect to the current flowing through the excitation port. In fact, the spatial trend of the current does not depend on the parameters investigated in this analysis (i.e., plasma parameters, source geometry, and magnetic topology). Moreover, the intensity of the current can be inferred once the deposited power and the antenna impedance (see Fig. 3.25, Table 3.1, and Fig. 3.26) are known [53, Eq. 13].

The current distribution over the Single Loop Antenna is almost uniform as depicted

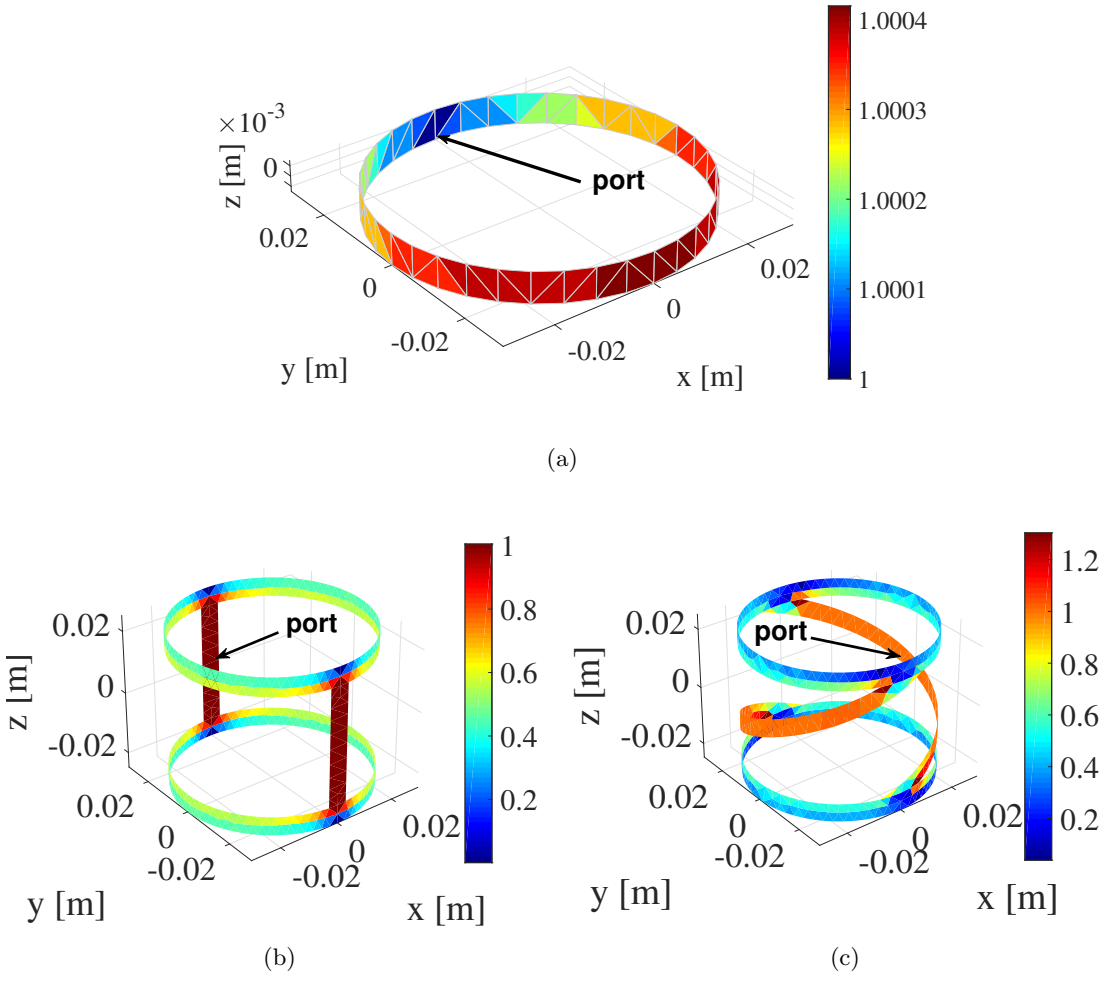

Figure 3.27: Antenna current distribution normalized in respect to the current flowing through the excitation port; (a) Single Loop Antenna, (b) Nagoya Type-III Antenna, and (c) Fractional Helix Antenna.

in Fig. 3.27(a). On the contrary, the antenna current is not constant over the loops of the Nagoya Type-III Antenna (see Fig. 3.27(b)). The largest variation of current is registered in the region where the loops are connected to the legs, on which the current is most intense and constant. The pattern of the current distribution over the Fractional Helix Antenna, given in Fig. 3.27(c),is similar to that of the current over the Nagoya Type-III Antenna. This is expected, since the Fractional Helix Antenna reduces to the Nagoya type-III Antenna in the limit of straight legs. However, in the Fractional Helix Antenna the largest values of the current are not registered in the legs of the antenna but in the region where the latter are joined to the loops.

In conclusion, it is worth highlighting that the spatial trends of the current depicted in Fig. 3.27 are almost equal to that reported in [117], where a similar analysis has been conducted for homogeneous discharges. Moreover, the two works predict coherent effects of the plasma parameters on the intensity of the current, in fact: (i) the latter depends on the antenna impedance through [53, Eq. 13], and (ii) in Sec. 3.2.1 it has been shown that the effect of the plasma parameters on the antenna impedance is in agreement with [117].

3.3 Thruster performances analysis

Following the methodology described in Sec. 2.3, the attainable thrust (T) and specific impulse (I_{sp}) can be preliminary estimated.

Higher (lower) thrust and specific impulse are associated to higher (lower) intensities of the magneto-static field (see Fig. 3.28). In fact, both the plasma density and the electron temperature at the source exhaust, and in turn F_0 (see Eq. 2.31), increase as the intensity of the magneto-static field does so (see Sec. 3.1.2); moreover the magnetic nozzle effect (i.e., the value of $\mathcal{M}_{det}$) depends monotonically on the magnetic field intensity. Lower

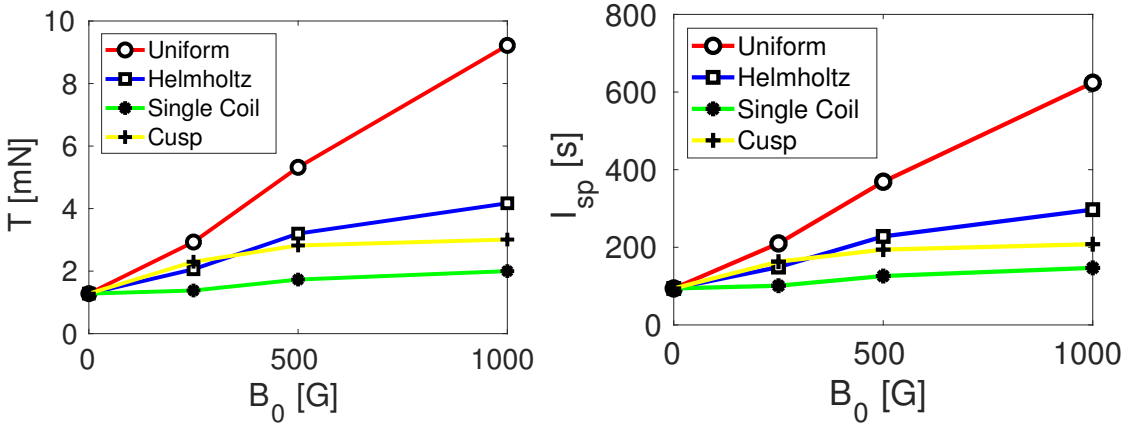

(a) (b)

Figure 3.28: (a) Thrust T and (b) specific impulse I_{sp} as a function of the intensity of the magneto-static field B_0 for a discharge surrounded by *Uniform*, *Helmholtz*, *Single Coil*, and *Cusp* magnetic topologies. The other parametes of the source are as in the *Reference* (see Fig. 3.3).

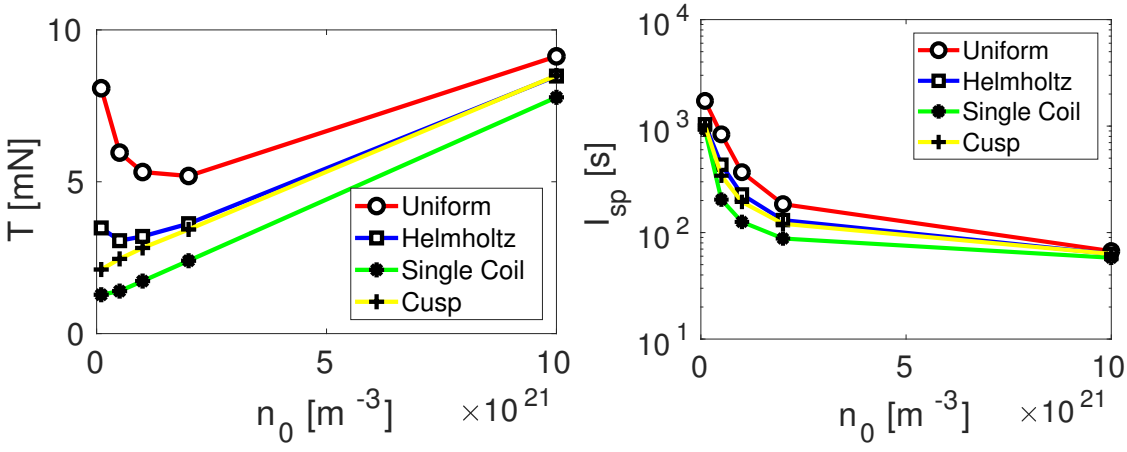

(a) (b)

Figure 3.29: (a) Thrust T and (b) specific impulse I_{sp} as a function of the initial neutral density n_0 for a discharge surrounded by *Uniform*, *Helmholtz*, *Single Coil*, and *Cusp* magnetic topologies. The other parametes of the source are as in the *Reference* (see Fig. 3.3).

(higher) specific impulse is associated to higher (lower) values of the neutral density (see Fig. 3.29(b)). On the contrary the relation between the thrust and the neutral density depends on the magnetic topology (see Fig. 3.29(a)). In the *Single Coil* and *Cusp* configurations higher (lower) thrust is associated to higher (lower) values of the neutral density; instead, in the *Uniform* and *Helmholtz* configurations this trend is reversed for values of

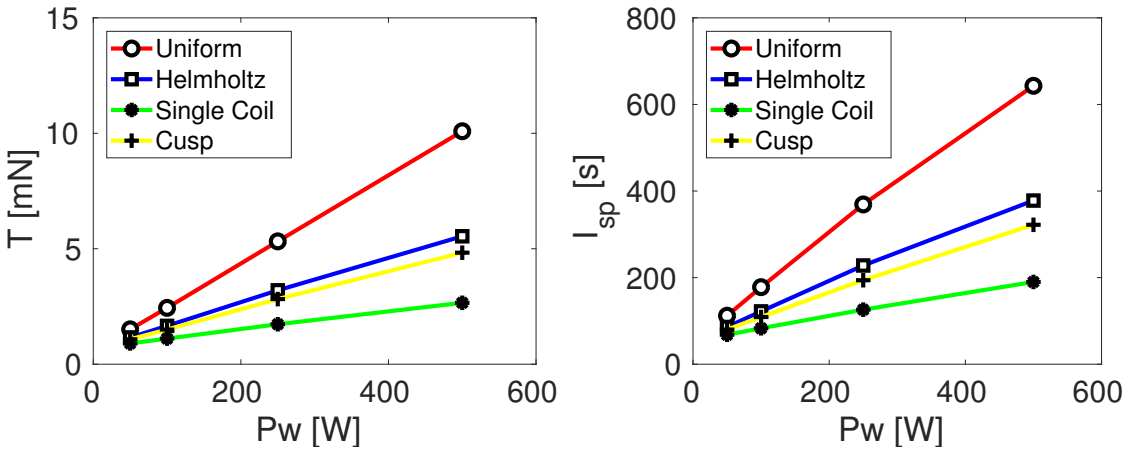

(a) (b)

Figure 3.30: (a) Thrust T and (b) specific impulse I_{sp} as a function of the total power deposited Pw for a discharge surrounded by *Uniform*, *Helmholtz*, *Single Coil*, and *Cusp* magnetic topologies. The other parametes of the source are as in the *Reference* (see Fig. 3.3).

the neutral density lower than a certain threshold (respectively $n_0 = 2 \times 10^{21}$ m^{-3} and $n_0 = 5 \times 10^{20}$ m^{-3}). Interestingly, in the *Uniform* case also the intensity of the electron density peak reverses its trend for values of the plasma density lower than the same threshold (see Sec. 3.1.3), with the consequent enhancement of the F_0 parameter and therefore of the attained thrust.

Higher (lower) thrust and specific impulse are associated to higher (lower) total power (see Fig. 3.30). In fact, the plasma density at the source exhaust increases as the total power does so (see Sec. 3.1.4). The propulsive performances are not significantly influenced by the antenna geometry (see Table 3.2). Only in the *Helmholtz* and *Single Coil* configurations a mild increase of the performances is associated to the adoption of Fractional Helix Antenna and Nagoya Type-III Antenna. Higher (lower) thrust is associated to higher (lower) values of the discharge radius (see Fig. 3.31(a)); for what concerns the specific impulse, the trend is reversed (see Fig. 3.31(b)). In this analysis the diameter of the exhaust section of the source is equal to the diameter of the plasma tube; therefore for higher values of the discharge radius the fluxes of both the plasma and the neutral particles increase, and in turn the overall thrust. Notably, the trend of the specific impulse highlights that the flux of the neutral particles is more influenced by the discharge radius in respect to the plasma flux.

Higher (lower) thrust and specific impulse are associated to lower (higher) values of the discharge length (see Fig. 3.32). This effect is more significant for the non-uniform magnetic configurations where the intensity of the magneto-static field at the source exhaust, and in turn the intensity of the magnetic nozzle effect, depends on the length of the discharge (see Fig. 3.2). In the specific case considered, reducing the discharge length results always in the increase of the value of $\mathcal{M}_{det}$. The best performing magnetic topology is the

Antenna		*Single Loop*	*Nagoya Type-III*	*Fractional Helix*
Uniform	T [mN]	5.32	5.95	5.77
	I_{sp} [s]	369	408	398
Helmholtz	T [mN]	3.20	3.68	3.69
	I_{sp} [s]	228	260	262
Single Coil	T [mN]	1.73	2.21	2.29
	I_{sp} [s]	126	160	166
Cusp	T [mN]	2.82	2.79	2.71
	I_{sp} [s]	194	196	192

Table 3.2: Thrust T and specific impulse I_{sp} for a discharge driven by *Single Loop*, *Nagoya Type-III*, and *Fractional Helix* antennas, along with surrounded by *Uniform*, *Helmholtz*, *Single Coil*, and *Cusp* magnetic topologies. The other parametes of the source are as in the *Reference* (see Fig. 3.3).

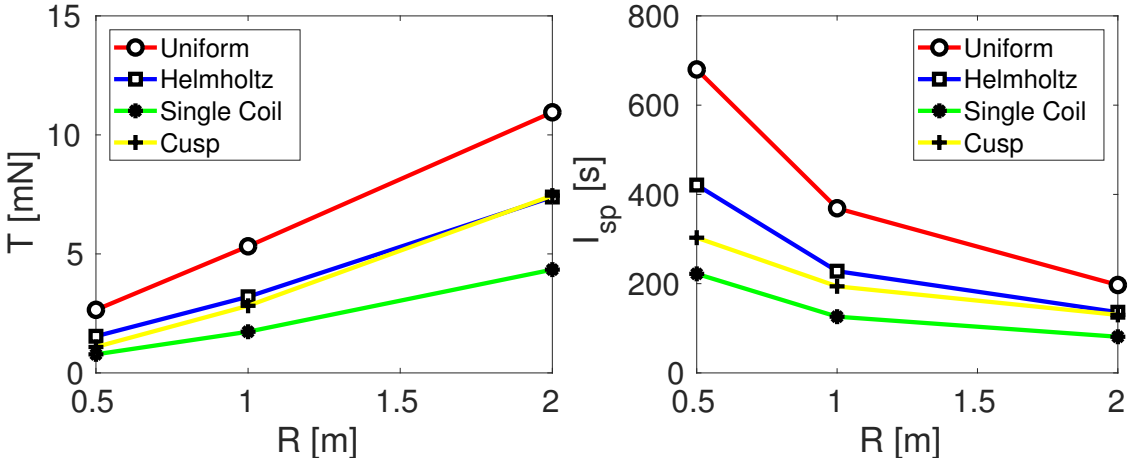

(a) (b)

Figure 3.31: (a) Thrust T and (b) specific impulse I_{sp} as a function of the discharge radius R for a discharge surrounded by *Uniform*, *Helmholtz*, *Single Coil*, and *Cusp* magnetic topologies. The other parametes of the source are as in the *Reference* (see Fig. 3.3).

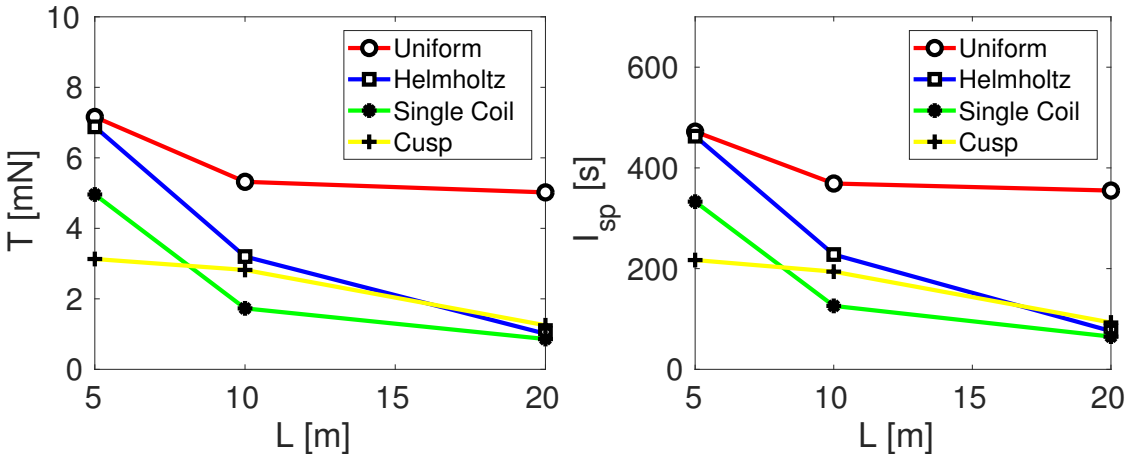

(a) (b)

Figure 3.32: (a) Thrust T and (b) specific impulse I_{sp} as a function of the discharge length L for a discharge surrounded by *Uniform*, *Helmholtz*, *Single Coil*, and *Cusp* magnetic topologies. The other parametes of the source are as in the *Reference* (see Fig. 3.3).

Uniform one, followed by the *Helmholtz* and the *Cusp* (see Figs. 3.28-3.32 and Table 3.2). More specifically, among the configurations simulated, the higher performances are associated to the magnetic topologies which guarantee an higher intensity of the magneto-static field in correspondence of the exhaust section of the source and therefore a more intense magnetic nozzle effect.

In conclusion, the best performances are obtained with the *Uniform* magnetic topology, and the intensity of magneto-static field and total power deposited as high as possible.

The other parameters can be tuned in order to increase the thrust and reduce the specific impulse or vice-versa.

3.4 Discussion

The main findings of the analysis conducted on the equilibrium plasma parameters within the discharge are:

- Higher values of the electron density peak have been found for: (i) the *Uniform* magnetic topology, (ii) higher intensities of the magneto-static field, (iii) higher values of the initial neutral density, (iv) higher amounts of power deposited into the plasma, (v) Fractional Helix and Nagoya Type-III antennas, and (vi) lower values of the discharge radius and length. Moreover, for the higher values of the initial neutral density the influence that the magneto-static field has on the electron density profile is very mild.

- Higher values of the electron temperature peak have been found for: (i) higher intensities of the magneto-static field, (ii) lower values of the initial neutral density. The other parameters do not significantly affect the electron temperature.

- The shape of the power deposition profile is principally influenced by: (i) the geometry of the magneto-static field lines, and (ii) the antenna geometry. The amount of power deposited in the core of the discharge is enhanced in presence of magnetic cusp regions and if the discharge is driven by a Fractional Helix or a Nagoya Type-III Antenna.

For what concerns the antenna behaviour:

- The parameters which has the major influence of the real part of the antenna impedance is the discharge radius; for what concerns the imaginary part, it is influenced only by the antenna geometry.

- The pattern of the current on the conductors of the antennae is not influenced by the parameters analysed. On the contrary, the intensity of the current depends on both the plasma parameters and the source geometry, and can be inferred from the antenna impedance and the total power deposited.

Finally, the thruster performances follow these general rules:

- The highest thrust and specific impulse are obtained with the *Uniform* magnetic topology, and the highest intensity of magneto-static field and total power deposited.

- The other parameters can be tuned in order to increase the thrust and reduce the specific impulse or vice-versa.

Notably, higher thruster performances are obtained in correspondence of higher values of electrons density and temperature. Therefore, the principal parameters which should be investigated in a future optimization analysis are the magneto-static field topology and

the geometry of the discharge chamber; in fact the total input power, the magneto-static field intensity (i.e., the weight of the system) and the initial neutral density (i.e., the mass flow rate) are usually constrained.

In many cases currently under analysis the peak of the electron density is not located on the axis of the discharge. This result is not in agreement with previous experiments performed on Helicon sources [118, 119, 120]. Nonetheless, it must be noted that the geometry of the sources considered in the present study is far distant from that of the experiments mentioned (the latter are approximately 1 m-long). In addition, both the source radius and length have been proven to significantly influence the position of the electron density peak (see Sec. 3.1.6 and Sec. 3.1.7). Moreover, in this very experiments the antenna was of the Helical type (i.e., similar to the Fractional Helix Antenna under analysis), and in Sec. 3.1.5 it has been shown that the electron density peak moves toward the centre of the discharge with this very type of antenna.

In conclusion, it is worth repeating that the outcome of this analysis is to gain some physical insight on how the principal design parameters influence the behaviour of a HPT, and not to simulate or optimize a realistic thruster. Nonetheless, the code developed during this work has been exploited also to simulate a real-life HPT prototype. The discussion of these further results and their comparison against experimental measurements have been reported in a dedicated chapter of this thesis (see Chap. 5). Finally, it is worth to point out that, when the code will be fully developed, it could be it could be used as an optimization tool for realistic HPTs.

Chapter 4

Experimental measurements

A counterbalanced pendulum thrust stand (see Fig. 4.1) has been designed [89] in order to evaluate the performances of HPTs at the high vacuum facility of the University of Padova [91, 66, 92]. This stand is a variant of the conventional hanging pendulum [69, 70], but it incorporates some novel features which enhance the range of HPT prototypes which can be tested. Specifically the stand has been designed in order to handle thrusters producing forces from tens of μNewton up to tens of milliNewton, operated with an electrical power lower than 1 kW, and whose weight envelope (i.e., thruster integrated with other subsystems such as the PPU) is up to 10 kg. This is accomplished through the reconfigurability of the counterweights (both in terms of mass and position) which allows regulating the sensibility of the instrument without changing the dimension of the pendulum arm. Moreover, the instrument is compact enough to be installed inside the vacuum

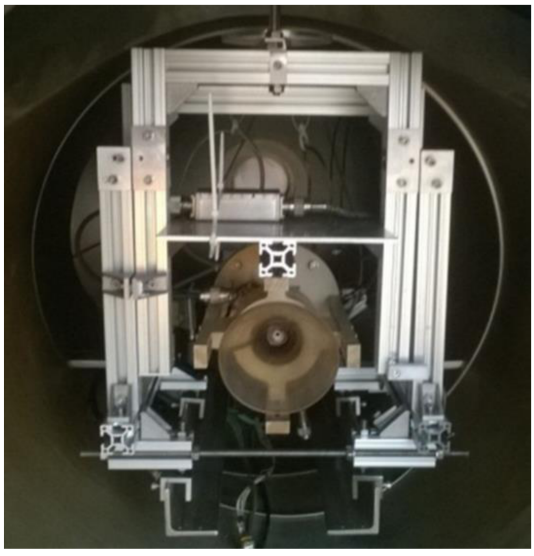

Figure 4.1: Picture of the counterbalanced pendulum thrust stand installed inside the vacuum chamber of the University of Padova. A HPT prototype of 0.5 kg is fastened to the stand.

chamber of the University of Padova (characterized by an inner diameter of 0.60 m and length of 2.00 m) providing more than 1 m of free space for the plume formation. Any null-displacement system [80, 81] has been avoided, since it may be affected by RF disturbances; rather than a laser interferometer has been employed to measure the displacement of the pendulum. In addition, the thrust stand has the capability to perform tens of measures per day (the system is particularly robust and easy to configure), and to provide rather accurate data (2-σ uncertainty in the range of 15%). In addition, even though the target application of the stand is the testing of HPTs, this instrument can be employed also for the characterization of other concepts of RF based electric thrusters (e.g., RIT [121] and electrodless [122]).

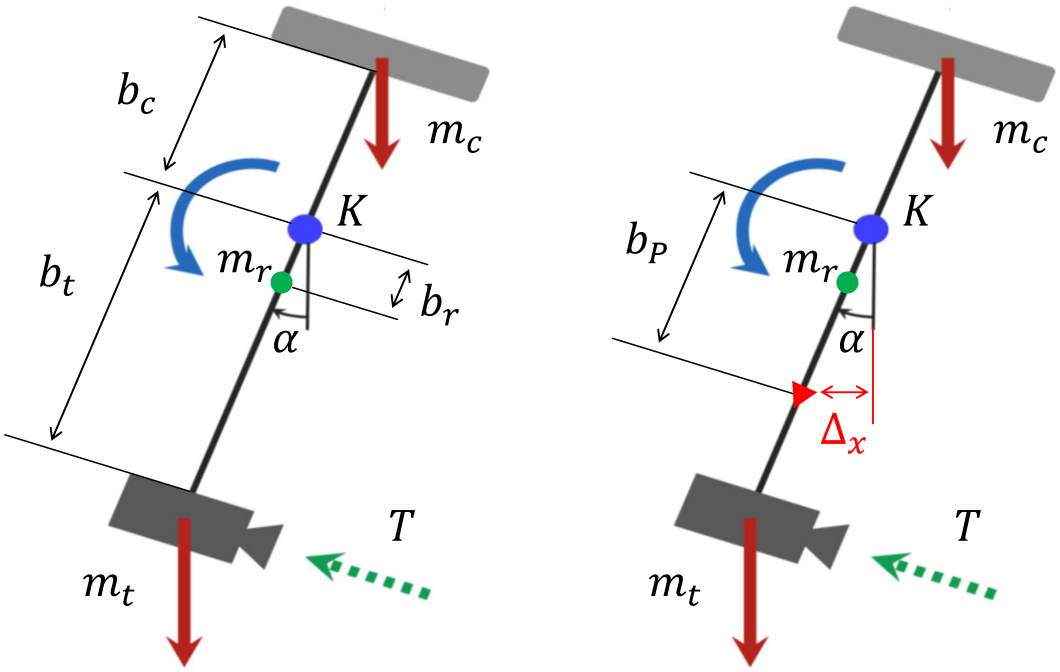

Figure 4.2: Schematic principle of the counterbalanced pendulum thrust stand. The parameters indicated are the produced thrust T, the mass of the thruster m_t, the mass of the counterweights m_c, the mass of the rotation arm m_r, the torsional stiffness of the pivot K, and the rotation angle α, along with: (a) the distance between the pivot and the thruster b_t, the counterweights b_c, and the centre of mass of the rotating arm b_r; (b) the horizontal displacement Δ_x to be measured, and the distance between the pivot and the reference point b_P.

4.1 Thrust stand design description

The schematic principle of the counterbalanced pendulum thrust stand is depicted in Fig. 4.2. The pendulum arm is fastened to the frame of the stand through a frictionless pivot characterized by a torsional stiffness K. The thruster is represented as a mass m_t fastened to the inferior tip of the pendulum arm at a distance b_t from the pivot, while the counterweights are depicted as a mass m_c distant b_c from the pivot (see Fig. 4.2(a)). In particular, the thrust T produces a rotation of the pendulum arm of an angle α given by the rotational equilibrium equation

$$K\alpha = Tb_t + g_0 \sin(\alpha)(m_c b_c - m_t b_t - m_r b_r) \tag{4.1}$$

in which m_r is the mass of the pendulum arm, b_r is the distance between the centre of mass of the pendulum arm and the pivot, and g_0 is the gravitational acceleration at sea level. Assuming small angles, Eq. 4.1 reduces to

$$\alpha = \frac{Tb_t}{K + g_0(m_t b_t - m_c b_c + m_r b_r)} \tag{4.2}$$

From a practical point of view, it is more accurate to measure the horizontal displacement Δ_x of a reference point in the pendulum arm (distant b_P from the pivot as reported in Fig. 4.2(b)) rather than the rotation angle α; therefore, from Eq. 4.2, it follows that

$$R_T = \frac{\Delta_x}{T} = \frac{b_t b_P}{K + g_0(m_t b_t - m_c b_c + m_r b_r)} \tag{4.3}$$

where R_T is the sensibility of the instrument.

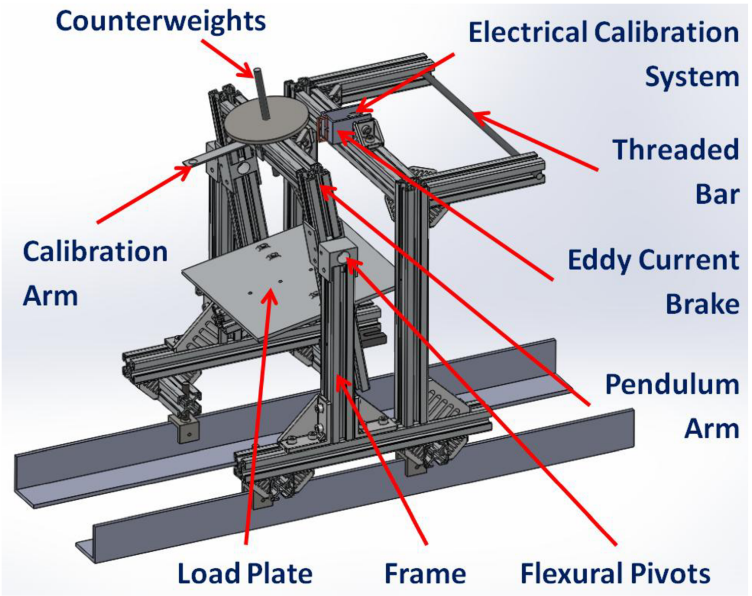

Figure 4.3: Illustration of the countrbalanced pendulum thrust stand.

4.1.1 Design

An illustration of the counterbalanced pendulum thrust stand is reported in Fig. 4.3. The frame of the stand is composed of two L-shaped legs joined by a threaded bar which is employed to house gas and power connections. The oscillating pendulum arm is C-shaped and is connected to the frame by means of two Riverhawk 5020-800 flexural pivots. The counterweights are housed in a mobile platform put on top of the pendulum arm. On the contrary, the thruster is fastened to a load plate integrated in the pendulum arm; any additional equipment, such as a Power Processing Unit (PPU) or Power Control Units (PCU) [15], can be placed on top of load plate. The pendulum arm is allowed to rotate freely and its displacement is measured by means of an Agilent 5529A near-Infrared Radiation (IR) laser interferometer, which is capable of a resolution inferior to 0.01 μm. The laser is focused through a series of mirrors on a corner cube reflector, placed on the inferior tip of the pendulum arm (see Fig. 4.4). The dumping of the vibrational noise is provided by an eddy current brake.

The principal calibration mechanism consists on a beam mounted on top of the pendulum arm (called calibration arm in Fig. 4.3), which can be loaded with a calibrated mass. Provided that the length of the calibration arm, namely the distance between the point in which the mass is applied and the pivot, is fixed, an accurate estimation of the torque applied to the pendulum arm can be obtained. Therefore the displacement induced can be associated to this very torque in order to estimate the sensibility of the instrument. Nevertheless, the principal calibration can be accomplished only if the system is not in vacuum. In order to quickly verify the calibration during the test session an auxiliary electrical calibration system has been added. This additional system is based on a coil and a permanent magnet fastened respectively to the frame and the pendulum arm. When the current is fed, a net momentum acts on the pendulum arm because of the interaction

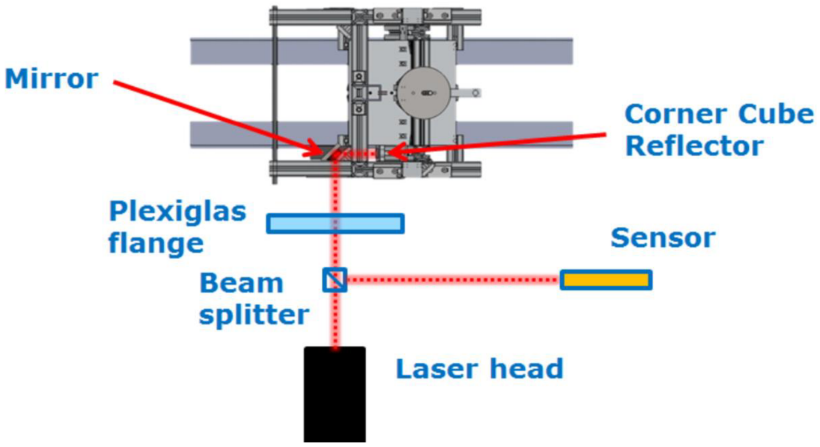

Figure 4.4: Schematic of the optical setup devoted to the evaluation of the displacement of the pendulum arm.

between the magnetic fields produced by respectively the coil and the permanent magnet. The applied current is then correlated to the displacement induced, thus obtaining a calibration tool employable also when the system is in vacuum.

In conclusion, it is worth highlighting that only commercially available components, such as standard aluminum profiles have been employed in order to minimize the cost effectiveness ratio.

4.2 Mechanical response of the thrust stand

Preliminarily, the thrust stand have been tested in order to verify how its mechanical response varies with the position and the mass of respectively the counterweights and the prototype at hand.

4.2.1 Calibration

The aim of the calibration is to determine the sensibility of the instrument, i.e., the ratio between the force exerted by the thruster and the horizontal displacement of the pendulum arm (see Eq. 4.3). The procedure is divided into two parts, namely principal and auxiliary calibration. During the principal calibration, the pendulum is loaded with a known mass

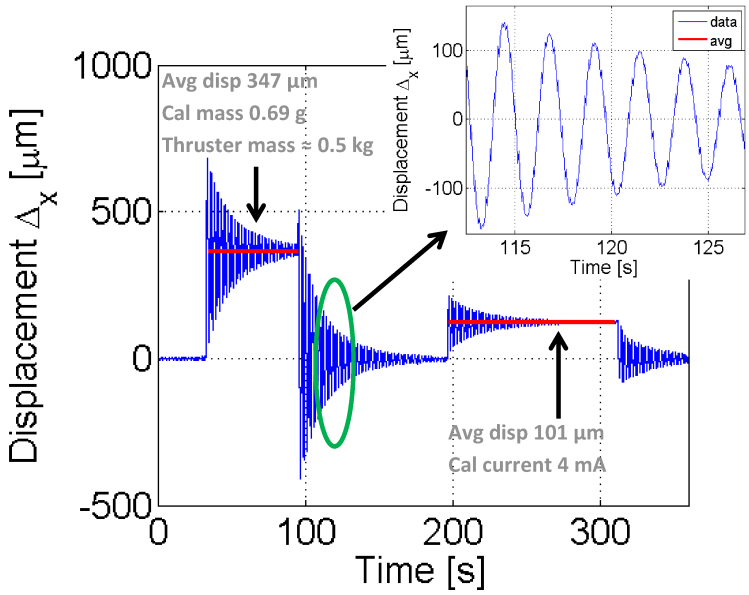

Figure 4.5: Calibration procedure: horizontal displacement of the pendulum arm Δ_x in function of the time. The thruster under test is a prototype of mass 0.5 kg. The calibration consists in two parts: i) application of a calibrated mass $m_m = 0.69 \pm 0.01$ g, ii) application of a calibration current $I = 4.00 \pm 0.01$ mA. The sensibility of the instrument is $R_T = 76.94 \pm 3.80$ μm/mN, $R_I = 25.25 \pm 1.75$ μm/mA. The zoom highlights the sinusoidal damped oscillation of the pendulum arm.

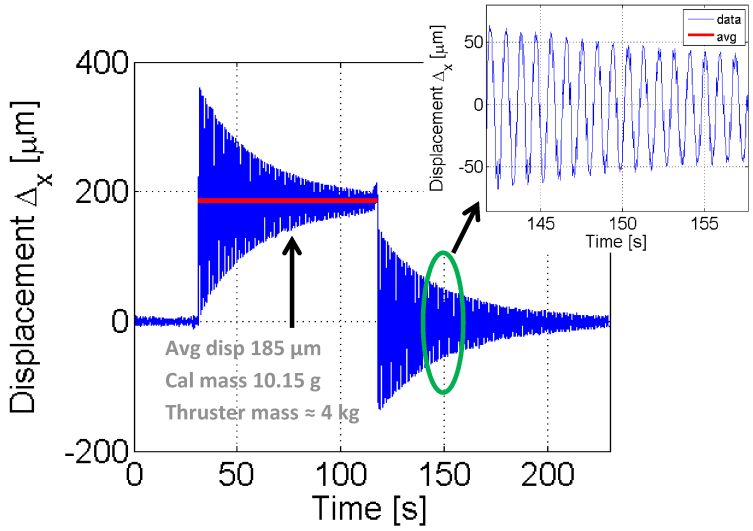

Figure 4.6: Calibration procedure: horizontal displacement of the pendulum arm Δ_x in function of time. The thruster under test is a prototype of mass roughly 4 kg. The calibration consists only on the application of a calibrated mass $m_m = 10.15 \pm 0.01$ g. The sensibility of the instrument is $R_T = 3.43 \pm 0.13$ μm/mN. The zoom highlights the sinusoidal damped oscillation of the stand.

m_m which produces a displacement Δ_x. The mass is fastened at the tip of the calibration arm (see Fig. 4.3), namely at a distance b_m from the pivot. The momentum generated is therefore $M_m = g_0 m_m b_m$, where g_0 is the gravitational acceleration. Notably, the same momentum would be reproduced by an equivalent thrust $T_{eq} = M_m / b_t$, where b_t is the thruster - pivot arm (see Fig. 4.2). Therefore, the sensibility of the instrument can be calculated as

$$R_T = \frac{\Delta_x}{T_{eq}} = \frac{\Delta_x b_t}{g_0 m_m b_m} \tag{4.4}$$

In the auxiliary calibration, the horizontal displacement Δ_x is produced by an electrical calibration system (see Fig. 4.3). More specifically, a current I flows in a coil fastened to the frame and produces a magnetic field; the latter interacts with a permanent magnet fastened to the pendulum arm, causing its displacement. In such a way, a current-displacement ratio can be calculated

$$R_I = \frac{\Delta_x}{I} \tag{4.5}$$

Clearly, this value must remain constant during all the test session, otherwise it means that the principal calibration is lost (for example because of the movement of electrical cables).

In the following, the calibration procedure performed with two different HPT prototypes has been discussed. More specifically, the mass of the two prototypes is respectively 0.5 kg and a 4 kg. The displacement of the pendulum arm, recorded during the calibration

with the 0.5 kg prototype, has been reported in Fig. 4.5. The stand has been loaded with a mass $m_m = 0.69 \pm 0.01$ g after 32 s from the beginning of the test, this has lead to an average displacement $\Delta_x = 347 \pm 1$ μm; at time $t = 95$ s the stand has been unloaded. Subsequently, at $t = 195$ s a current $I = 4.00 \pm 0.01$ mA has been imposed in the calibration wire, resulting in an average displacement $\Delta_x = 101 \pm 2$ μm. Provided that the mass has been loaded at a distance from the pivot $b_m = 0.100 \pm 0.002$ m and the thruster arm is $b_t = 0.150 \pm 0.002$ m, the equivalent thrust is $T_{eq} = 4.51 \pm 0.21$ mN. The resultant calibration ratios are therefore $R_T = 76.94 \pm 3.80$ μm/mN , and $R_I = 25.25 \pm 1.75$ μm/mA. For what concerns the calibration accomplished with the 4 kg prototype, it has been reported in Fig. 4.6. In this case, only the principal calibration with a mass $m_m = 10.15 \pm 0.01$ g has been performed. The stand has been loaded at $t = 31$ s causing an average displacement of $\Delta_x = 185 \pm 3$ μm. The resultant calibration ratio is $R_T = 3.43 \pm 0.13$ μm/mN. Finally, it is worth recalling that the uncertainty analysis has been performed in accordance with ISO/IEC GUIDE 98-3:2008(E) (GUM,1995) [123].

It can be seen from the two cases reported that the sensibility of the instrument is strongly dependent on the mass of the thruster. This was expected since, from the theoretical relation reported in Eq. 4.3, and being in practice $K \ll g_0(m_t b_t - m_c b_c + m_r b_r)$

$$R_T \propto \frac{1}{m_t - b_c/b_t m_c + b_r/b_t m_r} = \frac{1}{m_{red}} \tag{4.6}$$

where m_{red} is the reduced mass of the system which depends on the combination of the thruster mass and position (i.e., m_t and b_t), the counterweights mass and position (i.e., m_c and b_c), and the rotating arm geometry (i.e., m_r and b_r). Other analyses which confirm the inverse proportionality between R_T and m_{red} have been performed but are not reported for the sake of brevity.

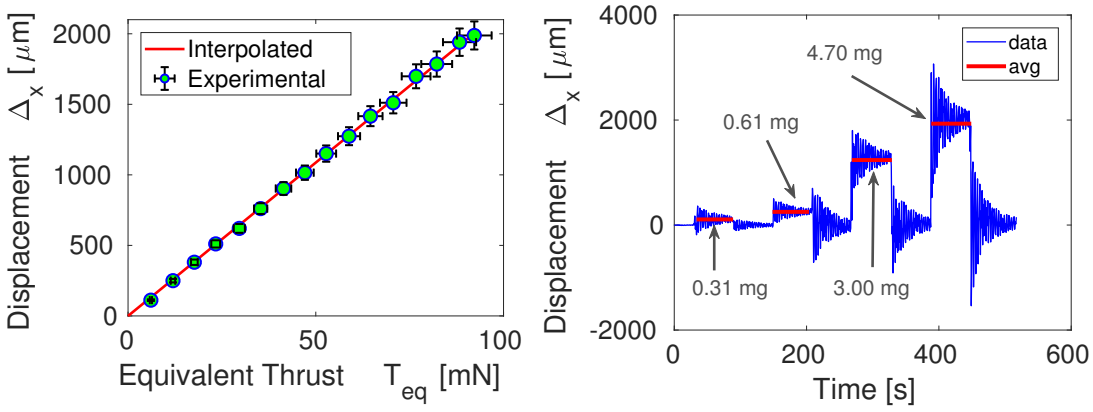

Figure 4.7: Linear response verification with a 0.5 kg-thruster: (a) averaged displacement Δ_x in function of the equivalent thrust T_{eq} generated by the calibration mass applied; (b) averaged "avg" and recorded "data" displacement in function of time if the calibrated masses employed are 0.31 ± 0.01 g, 0.61 ± 0.01 g, 3.00 ± 0.01 g, and 4.70 ± 0.01 g.

In conclusion, both in Figure 4.5 and Figure 4.6 a zoomed portion of the recorded displacement has been depicted in order to highlight that, after loading - unloading the stand, the pendulum arm describes sinusoidal dumped oscillations as expected.

4.2.2 Linear response verification

The interval of thrust inside which the stand responds linearly has been evaluated in the tests reported in Fig. 4.7 and Fig. 4.8; a prototype of 0.5 kg has been employed. More specifically, in the test of Fig. 4.7 the force exerted on the pendulum arm has been produced by calibrated masses in the range from 0.31 ± 0.01 g up to 4.70 ± 0.01 g which generate an equivalent thrust from 6.1 ± 0.3 mN up to 92.2 ± 4.6 mN. The linear behaviour is well verified in the overall thrust range (see Fig. 4.7(a)), which corresponds to a displacement of the pendulum arm up to 2000 μm (see Fig. 4.7(b)). In order to confirm that the results obtained are independent from the means in which the stand is loaded (calibrated masses in the case reported in Fig. 4.7), the linear response have been verified also when the displacement is induced by the calibration current. In the test reported in Fig. 4.8 the calibration currents has been varied from 5.00 ± 0.01 mA up to 100.00 ± 0.01 mA producing an equivalent thrust from 4.1 ± 0.2 mN up to 82.3 ± 4.1 mN. It can be confirmed that the linear behaviour is well verified in all the thrust range (see Fig. 4.8(a)), namely up to a displacement of roughly 2000 μm (see Fig. 4.8(b)).

In general, the linearity range is more properly associated to an interval of displacements rather than of forces: if the displacement induced by the thrust is higher than a threshold Δ_{max}, the small angle approximation for the pendulum rotation angle α is no more valid and the linear relation between α and the thrust T reported in Eq. 4.2 does not hold true. Therefore the maximum thrust for which the instrument is linear T_{max} is

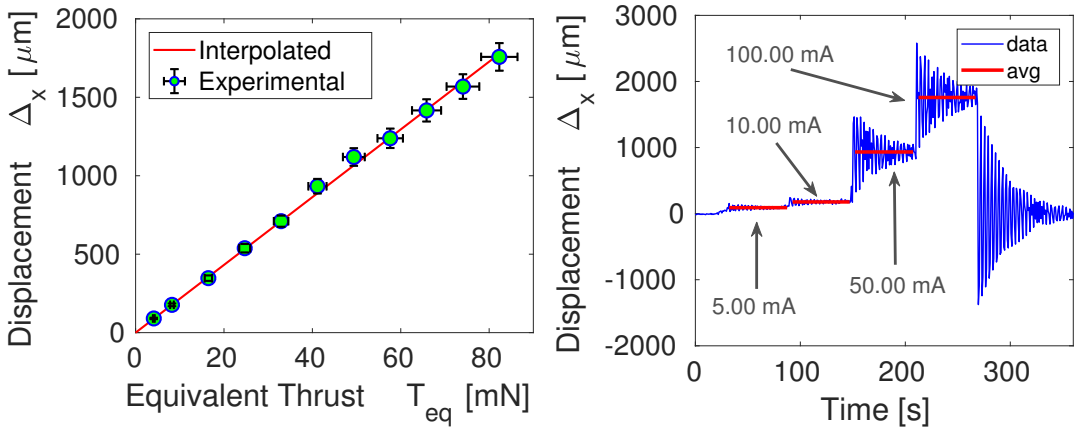

(a) (b)

Figure 4.8: Linear response verification with a 0.5 kg-thruster: (a) average displacement Δ_x in function of the equivalent thrust T_{eq} generated by the calibration current applied; (b) averaged "avg" and recorded "data" displacement in function of time if the calibration currents are 5.00 ± 0.01 mA, 10.00 ± 0.01 mA, 50.00 ± 0.01 mA, and 100.00 ± 0.01 mA.

not determined a-priori but depends on the sensibility R_T; it can be estimated empirically

$$T_{max} = \frac{\Delta_{max}}{R_T} \tag{4.7}$$

where $\Delta_{max} = 2000$ μm is a precautionary value chosen in accordance to the analysis depicted in Fig. 4.7 and Fig. 4.8.

4.2.3 Noise

The signal recorded during the test session, which gives the displacement in function of the time, is always affected by noise (see Fig. 4.9); the latter trivially limits the actual sensitivity of the thrust stand. The intensity of the noise has been evaluated through the standard deviation (σ) of the displacement (Δ_x) at the steady state while the pumping system was in operation. The signal recorded for a 0.5 kg thruster and a sensibility of $R_T = 79.21 \pm 4.19$ μm/mN, has been reported in Fig. 4.9. The intensity of the noise is $\sigma = 1.20$ μm, which corresponds to an equivalent thrust of $T_\sigma = 15$ μN. Nonetheless, the target thrust of the motor under test is roughly 1 mN, which corresponds to a displacement $\Delta_x \approx 80$ μm; therefore the noise is less than 2% of the expected value of the measurement. In general, the intensity of the noise increase as the sensibility does so. Moreover, σ is almost independent from the equilibrium position reached by the pendulum; this means that the intensity of the noise is not expected to change during the oscillations of the pendulum arm.

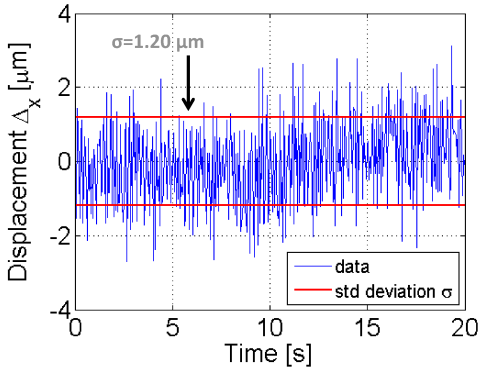

Figure 4.9: Displacement Δ_x recorded at the steady state; mass of the thruster 0.5 kg, and sensibility of the stand $R_T = 79.21 \pm 4.19$ μm/mN. The intensity of the noise is evaluated in terms of the standard deviation "std deviation σ" of the displacement "data" in respect to the equilibrium value; in this case $\sigma = 1.20$ μm.

4.3 Thrust measurement

Once the mechanical response of the stand had been thoroughly investigated, the instrument has been employed for measuring the actual thrust provided by the HPTs prototypes. As expected, once the system is subject to thermal and electrical loads zero-position drift [71] arises.

4.3.1 Zero-position drift

Pendulum-based thrust stands are notoriously susceptible to zero-position drift, which means that when the thruster is turned off, the pendulum arm does not return to its initial position [71]. In the case of the counterbalanced pendulum thrust stand, the drift is principally induced by the heating of the thruster caused by the plasma. In turn, thermal expansions arise and the centre of mass of the system shifts in respect to its initial position causing a rotation of the pendulum arm and consequently a zero-position drift. Also electrical wires, which heat up and deforms when the power to sustain the thruster is provided, can contribute to the zero-position drift. However, this second contribution can be minimized if the cables are disposed in order to minimize the torque induced into the pendulum arm, namely, are fastened close to the pivot.

An example of zero-position drift has been depicted in Fig. 4.10 where the displacement recorded during the test of a 0.5 kg HPT prototype has been reported. The acquisition

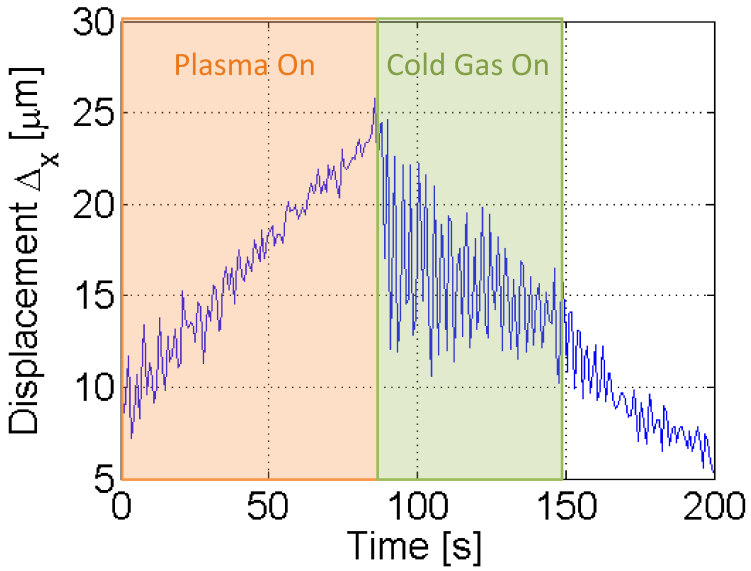

Figure 4.10: Example of zero-position drift: pendulum arm displacement Δ_x in function of time. The test is divided into three parts: (i) the thruster is operating at the steady state "Plasma On"; (ii) the plasma discharge is switched off but the cold gas is still flowing "Cold Gas On"; (iii) the mass flow of the cold gas is reduced to zero.

starts when the thruster is operating at the steady state ("Plasma On"); in this condition a steep thermal drift arises due to the heating induced by the plasma. When the antenna is turned off ($t = 90$ s), the direction of the drift reverses and its magnitude decreases because the thruster is cooling down. Near the $t = 150$ s mark the gas is interrupted. Therefore in order to evaluate the thrust, a procedure to mitigate or compensate the zero-position drift is required; in the present case, the correction is performed in post-processing.

It is worth recalling that other thrust stands include several additional components to mitigate the zero-position drift such as water cooling of the pendulum arm, or systems based on pools of liquid gallium to provide the power to the thruster [71]. Even though these strategies allows to enhance the accuracy of the measure, the complexity and cost of the apparatus significantly grow. Provided that a requirement of the counterbalanced pendulum thrust stand is to be a low cost and simple to operate device, the most suitable strategy seems to correct the zero-position drift in post-processing.

4.3.2 Zero-position drift correction and thrust evaluation

The procedure adopted to correct the zero-position drift in post-processing is explained with the aid of test depicted in Fig. 4.10 and Fig. 4.11. The experiment is split in three sub-sets (as shown in Fig. 4.10) in which the heating-cooling flux is almost constant and therefore the zero-position drift can be properly interpolated with a linear function (see Fig. 4.11(a)). The adoption of linear interpolation functions is justified if the test duration is much lower than the heating-cooling time scales; under this hypothesis the temperature evolution in time has a linear trend, and therefore the thermal expansions which generate the position drifts have a linear dependence from time too. The inclination of the inter-

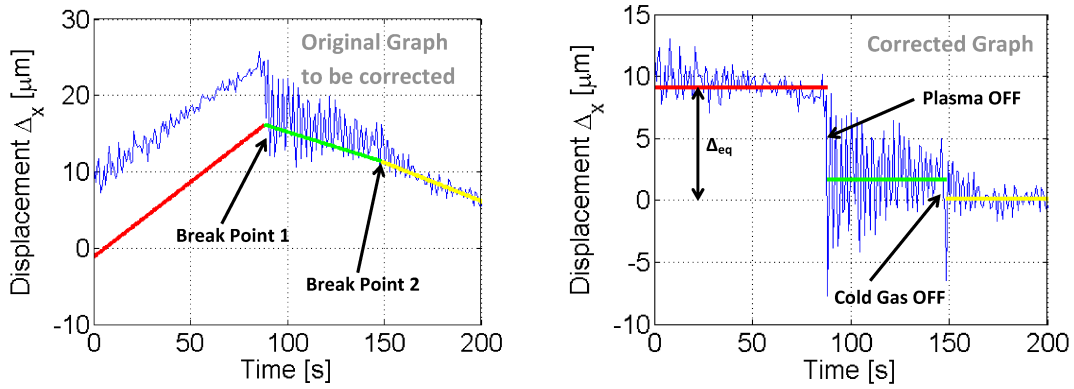

(a) (b)

Figure 4.11: Zero-position drift correction: (a) raw data, (b) corrected graph. The raw data have been corrected with three lines of different inclination, each line best fits the zero-position drift in one of the three sub-sets identified by the "Break Points". The thrust is evaluated from the difference Δ_{eq} between the average position when the plasma is on (red line) and the thruster is off (yellow line)

polation lines is determined with the least square method. The displacement corrected of the zero-position drift is computed subtracting the interpolation line to the raw data, the result is reported in Fig. 4.11(b). Once the corrected graph is obtained, the total thrust can be derived from the equivalent displacement (Δ_{eq}) calculated as the difference between the average position when the plasma is on (red line in Fig. 4.11(b)) and the thruster is off (yellow line in Fig. 4.11(b)).

It is worth to point out that this methodology gives a representative measure of the thrust only if the thruster is operating at the steady state when the plasma is turned off. The achievement of this condition is established checking that the plasma impedance and power absorption values are constant within a proper uncertainty band (some percentage points).

4.3.3 Accuracy of the measurement

In order to evaluate the accuracy of the measurements of the thrust stand, it is necessary to calculate the error introduced with the correction of the zero-position drift. This value has been identified with a Monte Carlo strategy

1. The "Break Points" which divide the experiments in sub-sets are preliminarily positioned in accordance with the test plan; e.g., "Break Point 1" is located where the plasma is supposed to be turned off, namely at $t = 90$ s (see Fig. 4.11).

2. The position of the "Break Points" is moved randomly with a standard deviation ± 2 s, the associated drift correction line is calculated (i.e., the piecewise line reported in Fig. 4.11(a)), and therefore a value of the thrust is obtained.

3. Iterating *step 2* for a sufficiently high number of repetitions (usually hundreds) a set of values is obtained whose mean value and standard deviation gives respectively the thrust measured and the uncertainty associated to the zero-position drift correction.

Test	T [mN]	Uncertainty [mN]
1	0.278	± 0.029
2	0.426	± 0.033
3	0.380	± 0.065
4	0.252	± 0.037
5	0.405	± 0.079

Table 4.1: Thrust T measured with the stand and relative uncertainty. Tested a 0.5 kg-HPT operated with xenon propellant.

The overall uncertainty is obtained combining the contributions of both the calibration and the drift correction procedures as prescribed in ISO/IEC GUIDE 98-3:2008(E) (GUM,1995) [123]. The results of five tests performed with a 0.5 kg-HPT operated with xenon propellant have been reported in Tab. 4.1: the uncertainty is in the order of 15%.

Moreover, it is worth highlighting that back-streaming effects due to the relatively proximity between the stand and the walls of the discharge chamber have not been accounted in the error budget. In fact, such effects have been proven to be non-negligible while testing cold-gas thrusters operated with mass flow rates higher than some milligrams per second, and relying on vacuum chambers smaller than the one of the University of Padova [124]. In addition, during the testing of HPTs (operated with input power up to 700 W, and mass flow rate up to 0.5 mg/s) in environments similar to the vacuum facility of the University of Padova (chambers 1-2 m long and with a diameter lower than 1 m) back-streaming effects have been neglected [19, 20]. Clearly, if thrusters requiring mass flow rates in the order of some milligrams per second would be operated in the vacuum facility of the university of Padova, dedicated analyses should be performed in order to account for back-streaming.

4.3.4 Benchmark

Finally, the measurements of the thrust stand have been benchmarked against the results of a Faraday probe [66]. In Table 4.2 four tests performed with a 0.5 kg-HPT have been reported; in particular the thruster has been operated with argon propellant in tests 1, 2 and 4, while Krypton has been adopted in test 3. The two estimations agree within 20%; the disagreement between the two measurement methods is in line with the 15% uncertainty associated to the data of the thrust stand, and the 40-50% uncertainty of the results of the Faraday probe.

Test	T_{FP} [mN]	T_s [mN]	ε_{rel} [%]
1	0.203	0.178	-12.4
2	0.254	0.208	-18.2
3	0.147	0.172	16.6
4	0.180	0.192	6.8

Table 4.2: The measurements of the thrust provided by the Faraday probe T_{FP} and the thrust stand T_s are reported, along with their relative difference ε_{rel}. A 0.5 kg-HPT prototype has been tested.

4.4 Experimental campaign

The thrust stand have been exploited in order to characterize a non-optimized medium-power (200-300 W) HPT prototype. The performances have been evaluated in terms of thrust (T), provided directly from the stand, and specific impulse (I_{sp}); the latter is derived from

$$I_{sp} = \frac{T}{g_0 \dot{m}_0} \tag{4.8}$$

where $\dot{m}_0$ is the propellant mass flow rate and g_0 is the acceleration of gravity. In particular, the input power to the thruster has been varied in the range from 50 W up to 450 W, the propellant mass flow rate from 0.1 mg/s up to 0.5 mg/s, and two propellants have been tested, namely xenon (Xe) and carbon dioxide (CO_2). The principal aim of the experimental campaign is to test the capability of the thrust stand to provide reliable data (uncertainty in the order of 15%), in a reasonable time (up to tens of tests per day), and in a wide range of operational conditions.

The experiments have been carried out inside the vacuum chamber of the University of Padova [66] which has a cylindrical shape, inner diameter 0.6 m, and length 2.0 m. The pumping capacity is 12600 l/s which allows achieving base pressures in the range of 10^{-6} mbar, and background pressures lower than $< 10^{-4}$ mbar when the thruster is operated with a 0.5 mg/s mass flow rate of Xe propellant. A water-cooled ENI OEM-12B3-02 linear amplifier driven by a HP 8648A signal generator has been adopted to provide the electric power to the thruster; the latter is measured with customized RF probes which guarantee an accuracy of some percent points [66]. The propellant mass flow rate is regulated with a MKS 1179A01311CS1BV mass flow controller whose accuracy is ± 0.01 mg/s.

The HPT prototype under test (see Fig. 4.12) has a cylindrical envelope of diameter 85 mm and length 130.5 mm, its mass is 1.5 kg. The discharge chamber has been realized in hexagonal Boron Nitride (hBN) because of its relatively high thermal conduction co-

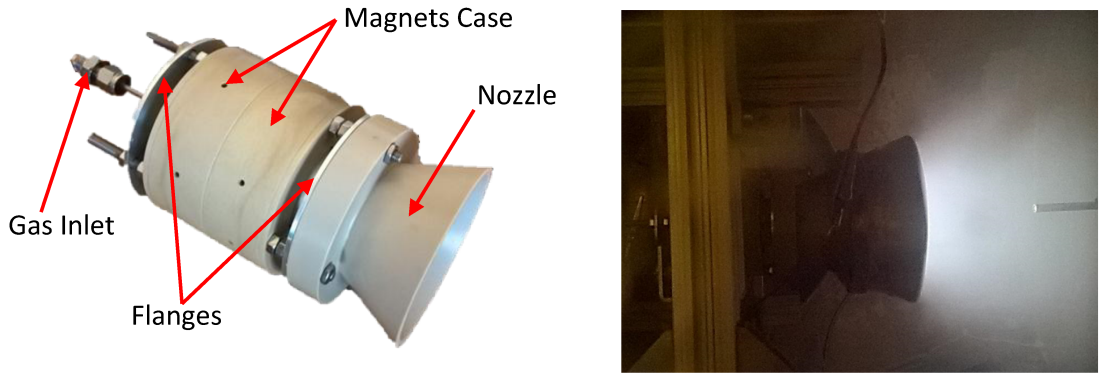

(a) (b)

Figure 4.12: Pictures of the HPT prototype which undertook the experimental campaign: (a) highlighted the principal components of the thruster, (b) thruster fastened to the stand and operated with CO_2 propellant.

efficient (up to 600 W/(m K)), low density (2100 kg/m^3), high resistance to erosion due to plasma, and high maximum operating temperature (up to 2270 K). The RF antenna is a S-Helicon type [125]. The magneto-static field is generated with permanent magnets in Samarium Cobalt (SmCo) whose residual magnetization is around 1.1 T, and the maximum operational temperature is around 300 °C; magnets are disposed in two rings around the plasma chamber. The resulting magneto-static field has a maximum intensity inside the discharge chamber of roughly 1500 G, presents two cusp regions, and the field lines downstream the plasma chamber are divergent; the latter means that this very field geometry produces a magnetic nozzle effect. The magnets are encased in supports in PEEK [126], this material has been selected because of its good mechanical properties, high temperature resistance and high thermal insulation. Also the nozzle at the exhaust of the discharge chamber is realized in PEEK. The frame of the prototype is realized in Aluminium (Al) and is electrically grounded (included the two Al flanges positioned at the front and back sides of the thruster).

4.4.1 Test

It is worth reporting a complete test (calibration and thrust evaluation) which illustrates the procedure followed to take each measurement of the experimental campaign. Specifically, the thruster is operated with Xe, the imposed mass flow rate is $\dot{m}_0 = 0.40 \pm 0.01$ mg/s and the imposed power is $Pw = 120 \pm 5$ W.

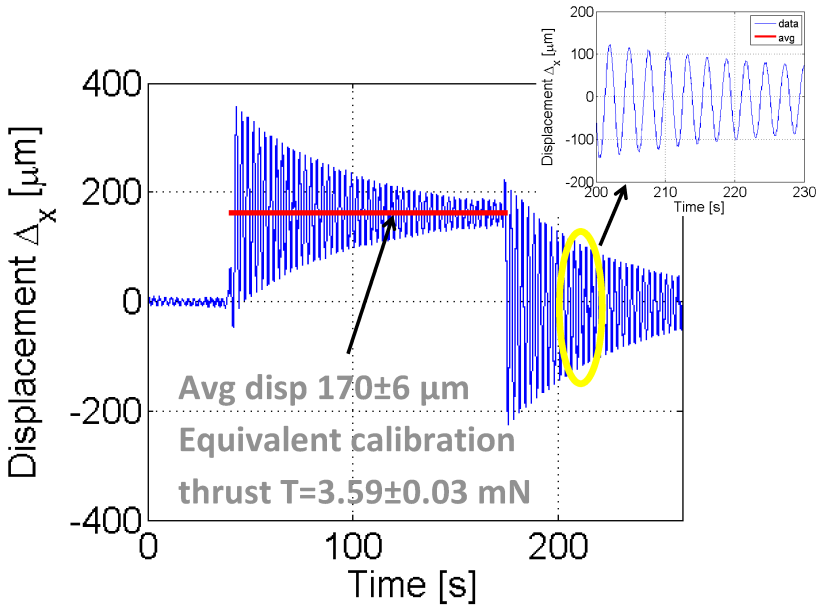

Figure 4.13: Calibration procedure; equivalent thrust of $T = 3.59 \pm 0.03$ mN. The sensibility of the instrument is therefore $R_T = 47.4 \pm 2.1$ μm/mN. Zoom highlights the sinusoidal damped oscillation of the stand after the mass removal.

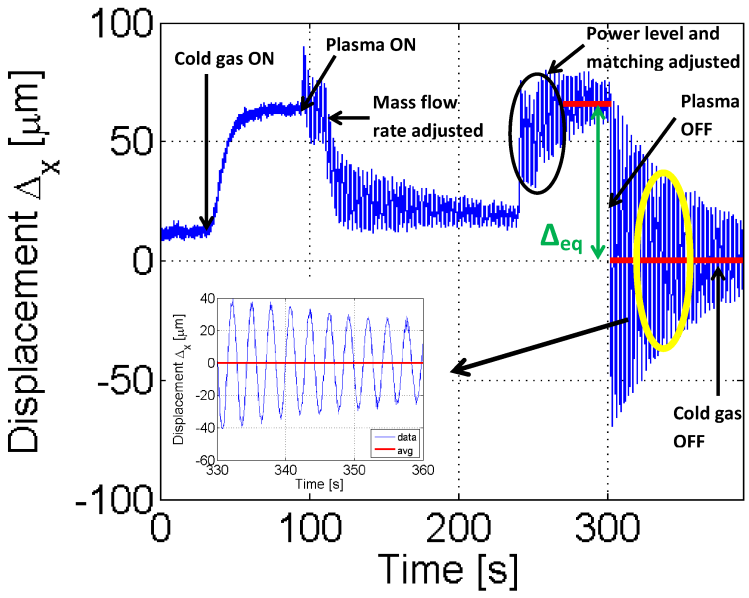

Figure 4.14: Thrust measurement; Xe mass flow rate of $\dot{m}_0 = 0.40 \pm 0.01$ mg/s, and input power of $Pw = 120 \pm 5$ W. The recorded signal reports: (i) supply of the maximum attainable Xe mass flow rate at t=30 s for the ignition, (ii) plasma switch on at 20 W at t=90 s, (iii) mass flow rate adjusted to 0.4 mg/s at t=105 s, (iv) power and electric matching adjusted to 120 W between t=240 s and t= 270 s, (v) plasma switch off at t=300 s, (vi) cold gas switch off at t=360 s. The measured thrust is $T = 1.43 \pm 0.29$ mN and specific impulse $I_{sp} = 364 \pm 82$ s. Zoom highlights the sinusoidal damped oscillation of the stand after the plasma switch off.

In Fig. 4.13 the calibration procedure has been reported. At $t = 40$ s the pendulum arm has been loaded with a known mass that generates the same torque of a thrust $T = 3.59 \pm 0.03$ mN; the calibration mass has been removed at $t = 175$ s. The average displacement generated by the calibration mass is $\Delta_x = 170 \pm 6$ μm, therefore the sensibility is $R_T = \Delta_x/T = 47.4 \pm 2.1$ μm/mN. The zoomed portion of Fig. 4.13 highlights the sinusoidal damped oscillation of the mobile arm after the mass removal.

Once the sensibility of the stand is known, the thrust can be measured as reported in Fig. 4.14. The test consists in: (i) at $t = 30$ s supplying the maximum Xe mass flow rate allowed by the gas feeding system, in order to ease plasma ignition, (ii) at $t = 90$ s switching on the plasma at 20 W power level, (iii) at $t = 105$ s regulating the mass flow rate at the nominal test value of 0.4 mg/s, (iv) between $t = 240$ s and $t = 270$ s regulating the power level at 120 W and adjusting the electrical matching, (v) at $t = 300$ s switching off the plasma, (vi) at $t = 360$ s switching off the cold gas mass flow rate. The difference between the average value of the displacement after and before the plasma switch off is $\Delta_{eq} = 68 \pm 11$ μm. Therefore, in accordance with the calibration reported in Fig. 4.13, the thrust is $T = \Delta_{eq}/R_T = 1.43 \pm 0.29$ mN, and from Eq. 4.8 the specific impulse results

$I_{sp} = 364 \pm 82$ s. In particular, in Fig. 4.14 only the graph corrected for the zero-position drift has been reported (correction applied only for $t \geq 270$ s); nonetheless the drift intensity was low ($< 5\%$ of Δ_{eq}). Moreover, it can be noticed that the cold gas switch off has produced negligible variations in the mean value of the displacement, therefore it can be assumed that almost only the plasma contributes to the thrust. Finally, the zoomed portion of Fig. 4.14 highlights the sinusoidal damped oscillation of the mobile arm after the plasma switch off.

4.4.2 Results

The results of the testing campaign for Xe have been depicted in Fig. 4.15, while for the CO_2 propellant in Fig. 4.16. In particular, both in Fig. 4.15 and Fig. 4.16, the uncertainty band has not been reported for the sake of clarity. Nonetheless, the uncertainty associated to the thrust is roughly 15%, to the specific impulse between 15% and 20%, to the power is few percent points, and to the mass flow rate ± 0.01 mg/s.

For what concerns the Xe propellant, higher (lower) thrust can be obtained with higher (lower) mass flow rates and input power (see Fig. 4.15(a)). The highest thrust achieved is around $T = 3$ mN for an input power of roughly $Pw = 350$ W and a mass flow rate of $\dot{m}_0 = 0.5$ mg/s. The specific impulse depends linearly from the input power and has a non-monotonous dependence to the mass flow rate (see Fig. 4.15(b)). More specifically, two different regimes can be identified, namely high specific impulse for a mass flow rate higher than $\dot{m}_0 > 0.3$ mg/s, and low specific impulse for $\dot{m}_0 < 0.3$ mg/s. The maximum specific impulse achieved is $I_{sp} = 700$ s with input power of roughly $Pw = 350$ W and a mass flow rate of $\dot{m}_0 = 0.5$ mg/s. If the thruster is operated with CO_2, the thrust has the same dependencies to input power and mass flow rate identified with the Xe gas (see Fig. 4.16(a)). The specific impulse still increases with the input power, but decreases

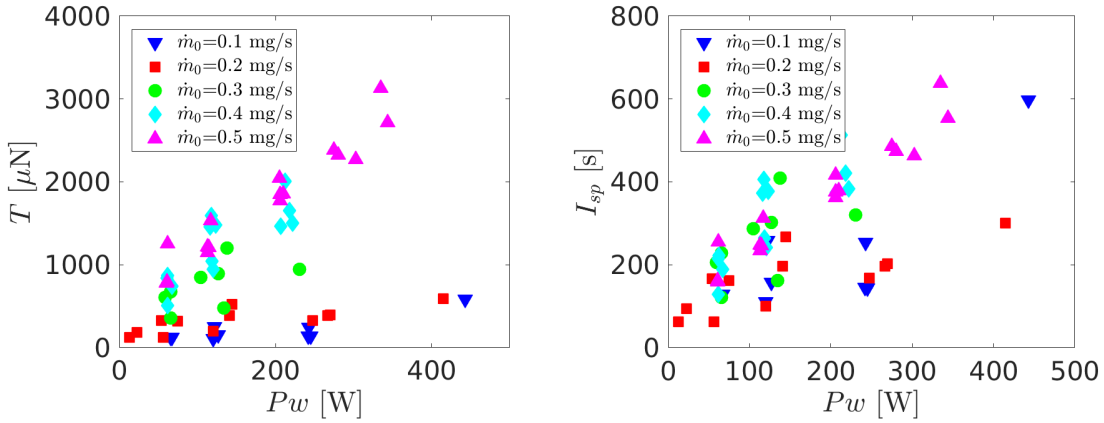

Figure 4.15: Performances of the HPT operated with Xe propellant: (a) thrust T against input power to the thruster Pw for different propellant mass flow rates $\dot{m}_0$; (b) specific impulse I_{sp} against input power to the thruster for different propellant mass flow rates.

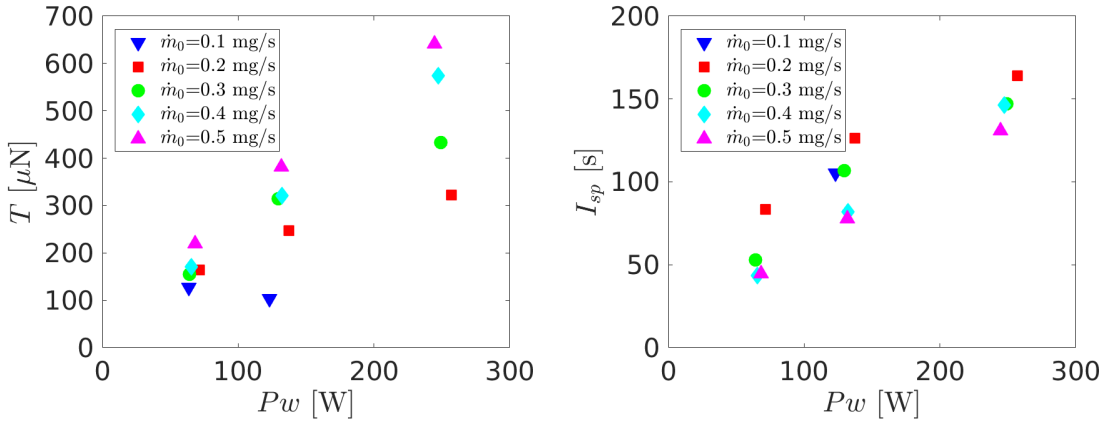

(a) (b)

Figure 4.16: Performances of the HPT operated with CO_2 propellant: (a) thrust T against input power to the thruster Pw for different propellant mass flow rates $\dot{m}_0$; (b) specific impulse I_{sp} against input power to the thruster for different propellant mass flow rates.

(increases) for higher (lower) values of the mass flow rate (see Fig. 4.16(b)). The higher thrust $T = 0.6$ mN have been obtained with a mass flow rate of $\dot{m}_0 = 0.5$ mg/s and an input power of roughly $Pw = 250$ W.

Therefore, independently from the propellant gas, the thrust increases (decreases) as both the mass flow rate and the input power does so, and the specific impulse is a linear function of the input power. On the contrary, the behaviour of the specific impulse in function of the the mass flow rate varies with the propellant gas. Moreover, for the same operative conditions, the thrust (specific impulse) obtained with Xe propellant is roughly four times higher than with CO_2; therefore the former performs far better than the latter from a propulsive standpoint. Finally, instability problems have been found when the thruster was operated with Xe at $\dot{m}_0 = 0.3$ mg/s, in particular when the input power was higher than $Pw > 250$ W (in Fig. 4.15 the measures taken in this very unstable regime have not been reported).

4.4.3 Discussion

The capabilities of the thrust stand have been successfully verified within this experimental campaign. The calibration procedure can be accomplished in less than five minutes (see Fig. 4.13), and each test requires less than ten minutes (see Fig. 4.14); therefore tens of measurements per day can be performed. Moreover, the uncertainty associated to the thrust measurement is in the order of 15%; these results are accurate enough for the intended application of the stand (i.e., characterization of HPT prototypes usually still under development). Finally, the thrust stand have not shown any problem (e.g., thermo-mechanical, electrical, or RF interference) in all the operational envelope that has been scanned (see Fig. 4.15 and Fig 4.16).

Chapter 5

Comparison between numerical and experimental results

The results of the HPT numerical model (see Chap. 2) have been compared against experimental measurements performed with the counterbalanced pendulum thrust stand in order to evaluate the reliability of the code when dealing with real-life prototypes. Nonetheless, the data discussed on Chap. 3 describe configurations which are too simplified in respect to the actual HPTs available at the University of Padova. At the same time, the data retrieved during the testing campaign described in Chap 4 cannot be employed for a comparison against numerical results being the actual code capable of simulating only HPTs operated with Ar gas. Therefore, a dedicated combined numerical-experimental campaign has been conducted on a non-optimized low power (50 W range) HPT prototype operated with Ar propellant.

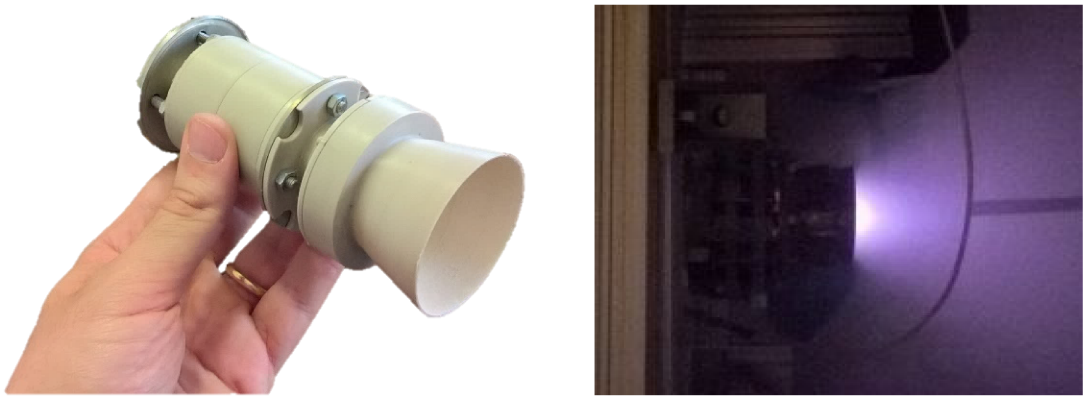

(a) (b)

Figure 5.1: (a) Picture of the low power (50 W range) HPT prototype under analysis, (b) thruster fastened to the stand and operated with Ar propellant.

5.1 Prototype description

The HPT prototype under consideration (see Fig. 5.1) has a cylindrical envelope of diameter 55 mm and length 120 mm, its mass is roughly 0.4 kg. As for the HPT described in Sec. 4.4, the discharge chamber has been realized in hexagonal Boron Nitride (hBN), the RF antenna is a S-Helicon type [125], and the magneto-static field is generated with two rings of permanent magnets in Samarium Cobalt. The field lines of the resulting magneto-static field has been depicted in Fig. 5.2; two cusp regions inside the discharge chamber can be noticed. The structure in which the magnets are encased, along with the physical nozzle have been realized in PEEK. Finally, the frame of the prototype is realized in Al and is electrically grounded.

In particular, the performances of the thruster (i.e., thrust T and specific impulse I_{sp}) have been evaluated, both experimentally and numerically, for an input power Pw varying from 10 W up to 70 W, and an Ar mass flow rate $\dot{m}_0$ from 0.06 mg/s up to 0.15 mg/s.

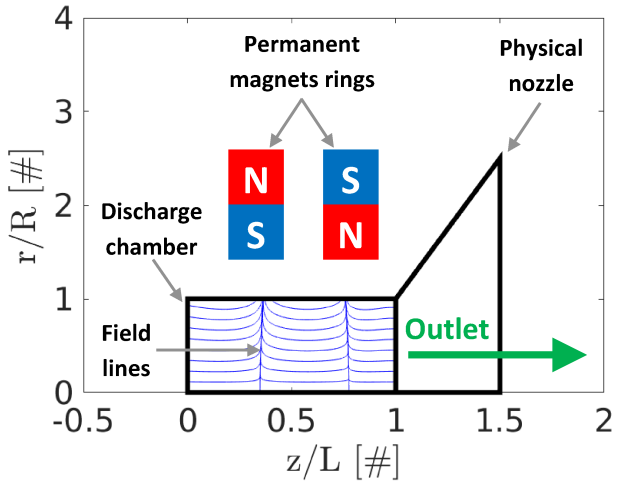

Figure 5.2: Schematic of the magnetic configuration of the HPT prototype under test. Highlighted the walls of the discharge chamber, the walls of the physical nozzle, the source outlet, the polarization of the two rings of permanent magnets which generate the magneto-static field, along with the field lines inside the discharge chamber. The radial coordinate r is normalized in respect to the source radius R, and the axial coordinate z in respect to the source length L.

5.2 Experimental measurements

The thruster performances have been measured at the vacuum facility of the University of Padova [66] with the counterbalanced pendulum thrust stand described in Chap. 4. A water-cooled ENI OEM-12B3-02 linear amplifier driven by a HP 8648A signal generator has been adopted to provide the electric power to the thruster; the latter is measured with customized RF probes which guarantee an uncertainty of some percent points [66]. The

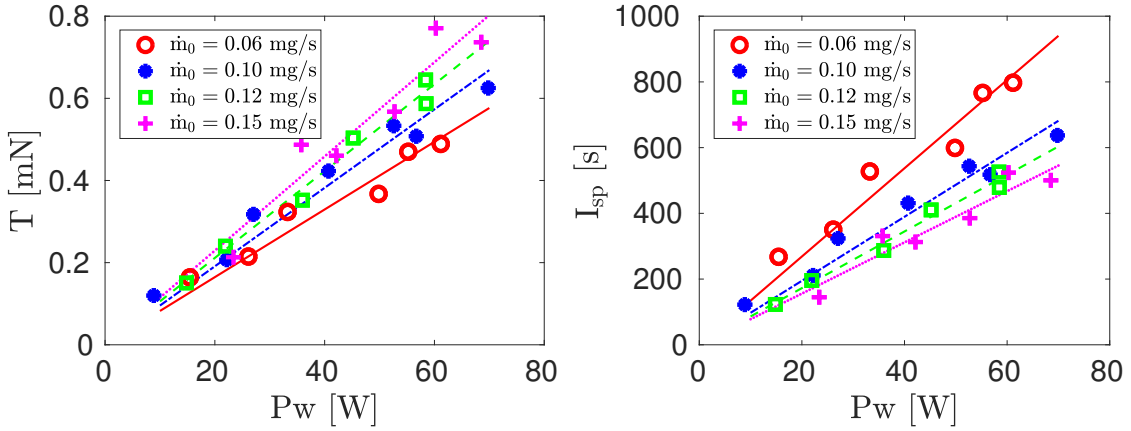

(a) (b)

Figure 5.3: Experimental measurements of the performances of the HPT prototype operated with Ar propellant: (a) thrust T (uncertainty in the order of 15%), and (b) specific impulse I_{sp} (uncertainty in the order of 15-20%) against input power Pw (uncertainty few percent points) for different propellant mass flow rates $\dot{m}_0$.

propellant mass flow rate is regulated with a MKS 1179A01311CS1BV mass flow controller whose accuracy is ±0.01 mg/s.

The results of the testing campaign has been reposted in Fig. 5.3. Higher (lower) thrust can be obtained with higher (lower) mass flow rates and input power (see Fig. 5.3(a)). The highest thrust achieved is around $T = 0.8$ mN for an input power of roughly $Pw = 70$ W and a mass flow rate of $\dot{m}_0 = 0.15$ mg/s. The specific impulse depends linearly from the input power and is inverse proportional to the mass flow rate (see Fig. 5.3(b)). The maximum specific impulse achieved is roughly $I_{sp} = 800$ s with input power of $Pw = 60$ W and a mass flow rate of $\dot{m}_0 = 0.06$ mg/s. No instability issues have been encountered within this input power and mass flow rate ranges. The uncertainty associated to the measurements is in the range of 15% for the thrust, and 15-20% for the specific impulse.

5.3 Numerical estimations

The low-power HPT prototype has been simulated with the numerical code described in Chap. 2 (i.e., 3D-VIRTUS for the analysis of the discharge chamber and a plume model for the preliminary estimation of the thruster performances). The plasma transport has been resolved in a 2D domain in order to reduce the computational cost. The convergence of the 3D-VIRTUS code has been stated when the relative error associated to the FLUID module is $\epsilon_{F,max} = 10^{-5}$ and to the iteration loop is $\epsilon_{max} = 10^{-1}$.

The estimation of the thruster performances has been reported in Fig. 5.4. Higher (lower) thrust is associated to higher (lower) values of mass flow rate and input power (see Fig. 5.4(a)). The highest thrust estimated is roughly $T = 0.5$ mN for an input power of $Pw = 70$ W and a mass flow rate of $\dot{m}_0 = 0.15$ mg/s. The specific impulse depends linearly from the input power and is inverse proportional to the mass flow rate (see Fig. 5.4(b)).

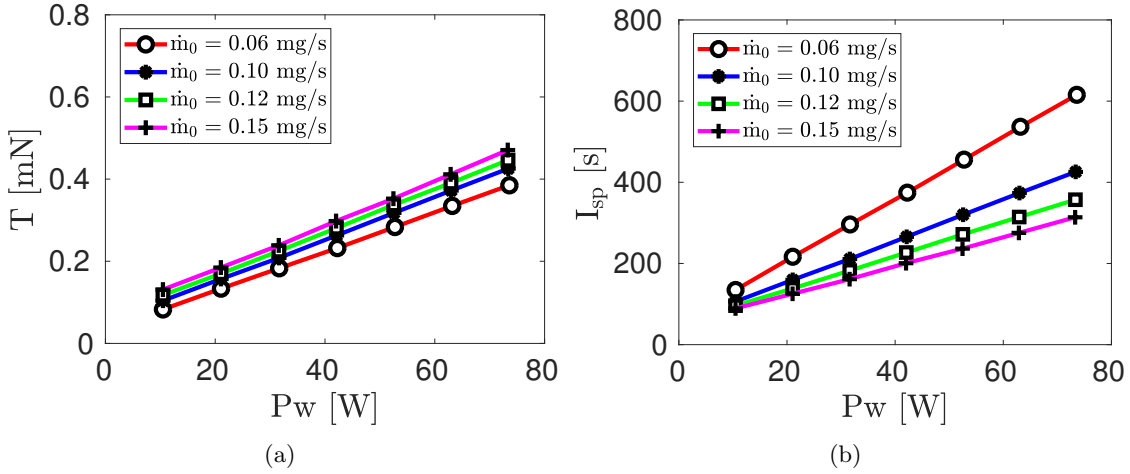

(a) (b)

Figure 5.4: Numerical estimations of the performances of the HPT prototype operated with Ar propellant: (a) thrust T, and (b) specific impulse I_{sp} against input power Pw for different propellant mass flow rates $\dot{m}_0$.

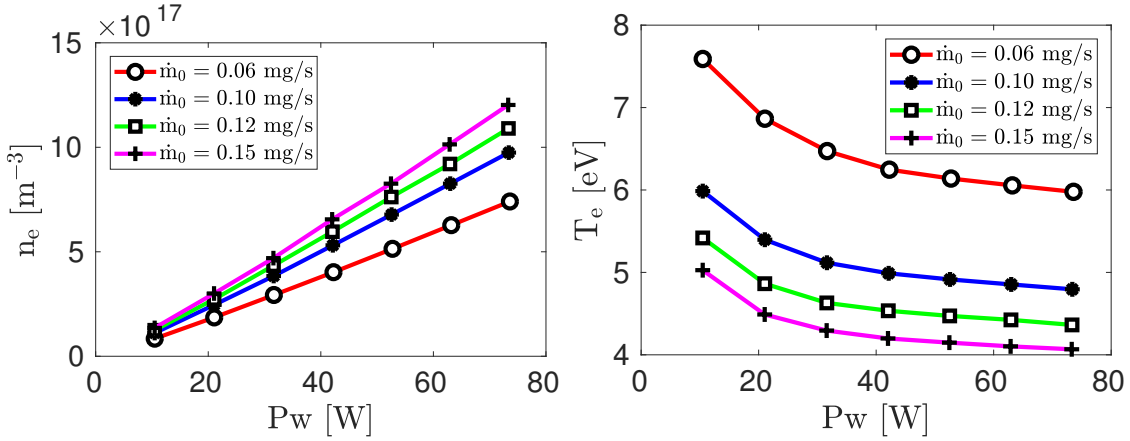

(a) (b)

Figure 5.5: Numerical estimations of the average plasma properties at the outlet section of the HPT prototype operated with Ar propellant: (a) electrons density n_e, and (b) electrons temperature T_e against input power Pw for different propellant mass flow rates $\dot{m}_0$.

The maximum specific impulse estimated is roughly $I_{sp} = 600$ s with input power of $Pw = 70$ W and mass flow rate of $\dot{m}_0 = 0.06$ mg/s.

In order to get a deeper physical insight on the results depicted in Fig. 5.4, it is worth discussing more thoroughly the data provided by 3D-VIRTUS on the plasma discharge. In Fig. 5.5 the average values of electrons density n_e and electrons temperature T_e on the outlet section of the discharge have been reported. In fact, the thrust provided by the acceleration of the plasma, and in turn T, depends linearly from both n_e and T_e (see

Eq. 2.31). The electrons density increases with the input power, while the electrons temperature mildly decreases (see respectively Fig. 5.5(a) and Fig. 5.5(b)); the former effect is more intense than the latter, therefore both thrust and specific impulse increase with the input power (as depicted in Fig. 5.4). Similarly, the electrons density increases with the mass flow rate while the electrons temperature decreases (see respectively Fig. 5.5(a) and Fig. 5.5(b)). The former effect is slightly more intense than the latter and therefore, in combination with an higher thrust provided by the neutral gas acceleration, the total thrust T increases with the mass flow rate (see Fig. 5.4(a)). On the contrary the specific impulse decreases with the mass flow rate as the electrons temperature does (see Fig. 5.4(b) and Fig. 5.5(b)).

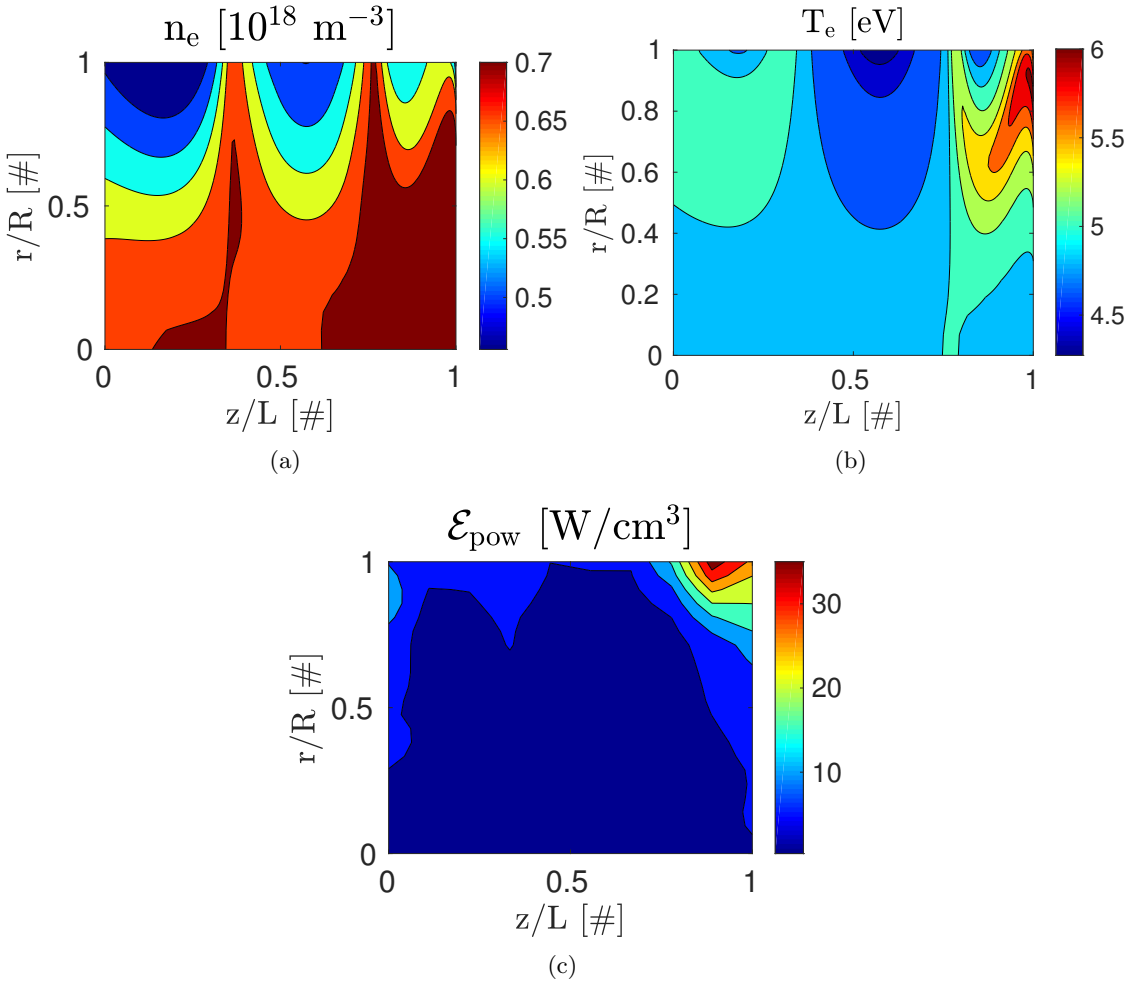

Figure 5.6: Numerical estimations of the plasma parameters distribution inside the discharge chamber in function of the radial r and axial z positions (normalized in respect the the source radius R and length L): (a) electron density n_e, (b) electron temperature T_e, and (c) power deposition $\mathcal{E}_{pow}$. Input power $Pw = 50$ W, Ar mass flow rate $\dot{m}_0 = 0.10$ mg/s.

Finally, the distribution of the plasma parameters on the discharge chamber, calculated with 3D-VIRTUS, has been depicted on Fig. 5.6. Specifically, the electrons density n_e, the electrons temperature T_e, and the power deposition $\mathcal{E}_{pow}$ have been reported for an input power $Pw = 50$ W and a mass flow rate $\dot{m}_0 = 0.10$ mg/s. Despite the presence of the two magnetic cusps, the electron density distribution is mildly non-uniform inside the discharge, and the peak value is registered in correspondence of the source outlet (see Fig. 5.6(a)). The electrons temperature presents a higher degree of non-uniformity in respect to the electrons density, nonetheless the peak value is located in correspondence of the source outlet and close to the edge (see Fig. 5.6(b)). Moreover, it must be noticed that also the power deposition peak is located very close to the source outlet and on the edge (see Fig. 5.6(c)). Therefore, even if the prototype has not undertook a dedicated optimization campaign, the plasma parameters are maximum in correspondence of the

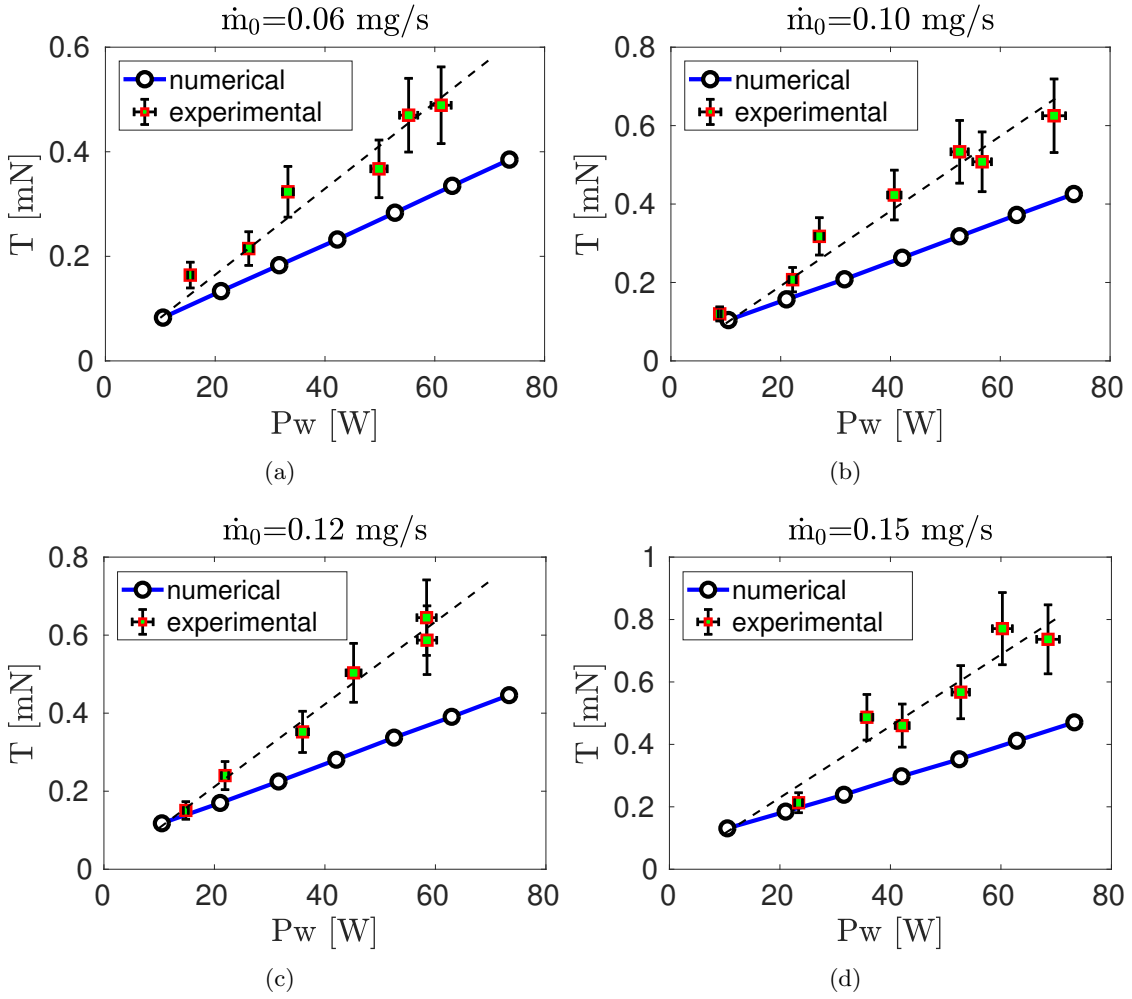

Figure 5.7: Comparison between the experimental measurements and the numerical estimations of the attainable thrust T against the input power Pw. Ar mass flow rate: (a) $\dot{m}_0 = 0.06$ mg/s, (b) $\dot{m}_0 = 0.10$ mg/s, (c) $\dot{m}_0 = 0.12$ mg/s, (d) $\dot{m}_0 = 0.15$ mg/s.

source outlet leading to an enhancement of the thruster performances (see Eq. 2.31) in respect to the wall losses [42, Sec.II-D]. In conclusion, the plasma parameters distributions share the same features highlighted for the case reported in Fig. 5.6 regardless the value of the input power and of the mass flow rate.

5.4 Comparison

The thruster performances measured experimentally (see Sec. 5.2), and estimated numerically (see Sec. 5.3) have been compared in order to verify the reliability of the HPT model when handling a real-life prototype.

From a qualitative standpoint, the numerical and experimental data show a good agreement. In fact, the HPT model has predicted: (i) the linear dependency of both the

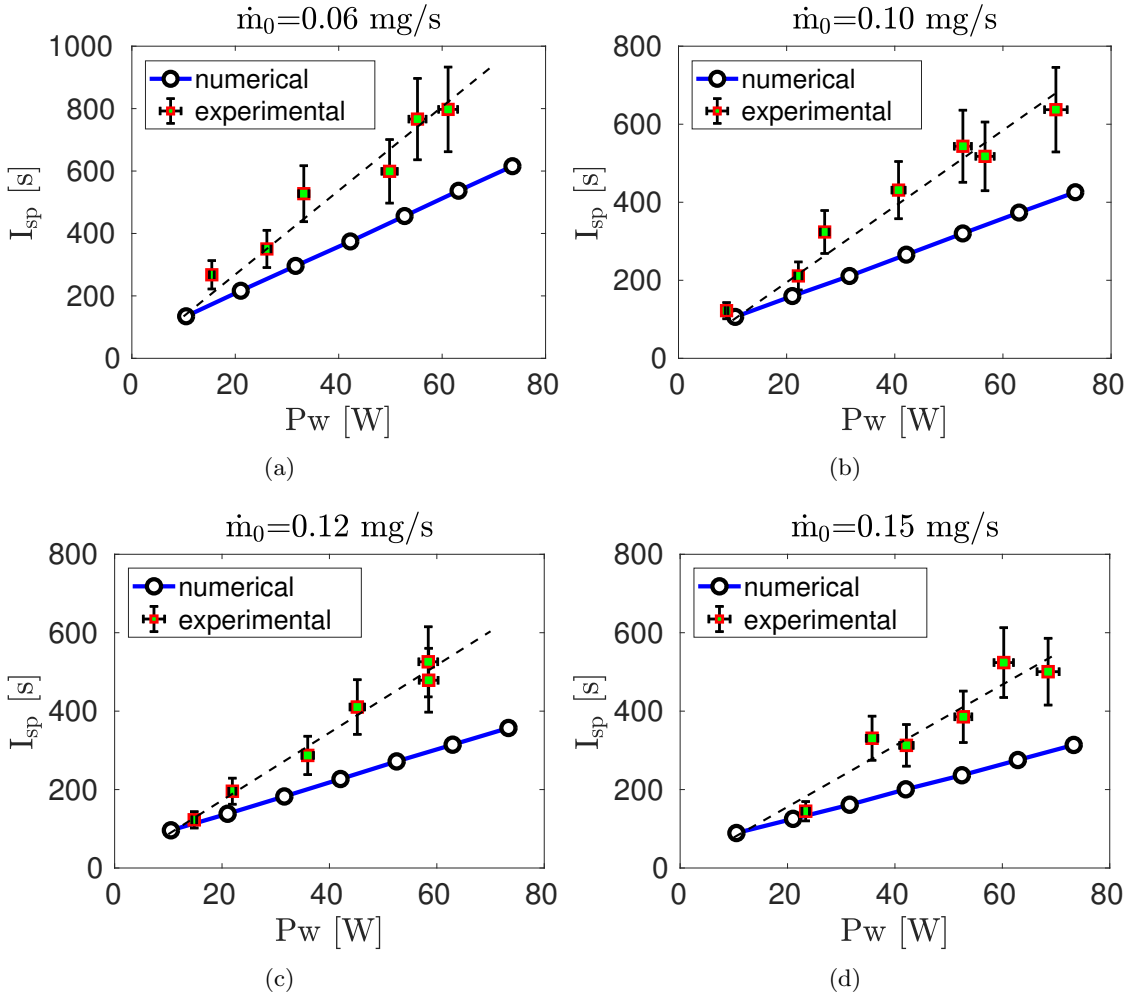

Figure 5.8: Comparison between the experimental measurements and the numerical estimations of the attainable specific impulse I_{sp} against the input power Pw. Ar mass flow rate: (a) $\dot{m}_0 = 0.06$ mg/s, (b) $\dot{m}_0 = 0.10$ mg/s, (c) $\dot{m}_0 = 0.12$ mg/s, (d) $\dot{m}_0 = 0.15$ mg/s.

thrust T and the specific impulse I_{sp} from the input power Pw (compare Fig. 5.3 and Fig. 5.4), (ii) the linear increase of T with the mass flow rate $\dot{m}_0$ (compare Fig. 5.3(a) and Fig. 5.4(a)), and (iii) the inverse proportionality between I_{sp} and $\dot{m}_0$ (compare Fig. 5.3(b) and Fig. 5.4(b)).

From a quantitative standpoint, the agreement is satisfactory. Regardless the value of $\dot{m}_0$, the numerical estimation of T almost agrees with the experimental data for $Pw =$ 10 W; however the relative error between experimental and numerical results increases progressively up to 40% for $Pw = 70$ W (see Fig. 5.7). Similarly, the relative error on I_{sp} grows from few percent point at $Pw = 10$ W up to 50% at $Pw = 70$ W, still regardless the value of $\dot{m}_0$ (see Fig. 5.8). This mismatching cannot be attributed exclusively to the measurement uncertainty, being the latter in the order of 15-20% for both T and I_{sp}. Nonetheless, a better agreement was not expected; in fact, as previously stressed, the plume model [42] describes the plasma acceleration and detachment with a simplified 1D approach which cannot provide very accurate results. In particular, the paraxial approximation and the detachment criterion (see Sec. 2.3), are the main limitation of the actual model adopted to estimate the propulsive performances. Finally, it is worth highlighting that the HPT numerical model predicts lower thruster performances in respect to the measured values, therefore it provides conservative data.

In summary, a low-power (50 W range) HPT operated with Ar gas has been analysed both numerically and experimentally. The comparison has shown a good qualitative and a satisfactory quantitative agreement. Nonetheless, a better accord was not expected since the plume model adopted for the estimation of the performances is very simplified. Moreover, it has been shown numerically that, even if the thruster is not optimized, the plasma parameters distributions are more intense in the source outlet leading to an enhancement of the propulsive performances in respect to the wall losses.

Chapter 6

Conclusions, future work, and novelty

6.1 Conclusions

This work has been focused on the presentation and discussion of:

- A numerical model of HPT which consists on the 3D-VIRTUS code [88] for the simulation of Helicon sources and a simplified plume model [42] for the preliminary estimation of the propulsive performances.
- The characterization and the exploitation of a counterbalanced pendulum thrust stand [89] specifically developed for testing HPTs.

The numerical model of HPT operates in two steps: (i) first the Helicon source is solved with 3D-VIRTUS, (ii) second the plume is simulated with an analytical model that takes as input the plasma parameters at the source outlet. In particular, 3D-VIRTUS solves self-consistently (i.e., both EM wave propagation and plasma transport) the equilibrium conditions of a Helicon plasma source that has arbitrary geometry, is driven by an arbitrary-shaped conductive RF antenna, and is magnetized by coils or permanent magnets. As a result, it is possible to predict the propulsive performances of HPTs relying on realistic Helicon sources. Moreover, 3D-VIRTUS has been verified against both the well established code SEMS [59] and against experimental measurements [93].

The numerical model of HPT has been exploited in a parametric analysis in order to gain a preliminary insight on how the principal design parameters (e.g., geometry of the magneto-static field, of the antenna, and of the discharge chamber) affect the thruster behaviour. The main findings of the study performed on the plasma discharge are:

- The maximum values of plasma density and electron temperature have been obtained for the highest intensities of the magneto-static field and input power.
- The behaviour of the discharge is strongly influenced by the initial neutral density: the plasma density increases as the neutral density does so, while the electron temperature decreases.

- Higher plasma densities have been found in presence of a uniform magneto-static field, and for the lower values of the discharge radius and length. These very parameters (i.e., geometry of the source and of the magneto-static field topology) have a relatively mild influence on the electron temperature.

- The power deposition profile is significantly influenced only by the geometry of the antenna and of the magneto-static field topology; the amount of power deposited in the core of the discharge is enhanced in presence of a magnetic cusp region and if the discharge is driven by a Fractional Helix or a Nagoya Type-III antenna.

For what concerns the preliminary estimation of the thruster performances:

- The best thruster performances are obtained with uniform magnetic topology, and the highest intensities of magneto-static field and input power.

- The other parameters (i.e., neutral density, geometry of the source and of the antenna) can be tuned in order to enhance the thrust and reduce the specific impulse or vice-versa.

Notably, higher performances are obtained in correspondence of higher values of electrons density and temperature. Therefore, the principal parameters which should be investigated in a possible optimization analysis are the magneto-static field topology and the geometry of the discharge chamber; in fact the total input power, the magneto-static field intensity (i.e., the weight of the system) and the initial neutral density (i.e., the mass flow rate) are usually constrained.

The counterbalanced pendulum thrust stand is a variant of the conventional hanging pendulum in which both the position and the mass of the counterweights can be reconfigured in order to regulate the sensibility of the instrument. Specifically, the stand can handle prototypes producing thrust from tens of μNewton up to tens of milliNewton, operated with an electrical power lower than 1 kW, and whose weight envelope (i.e., thruster integrated with other subsystems such as the PPU) is up to 10 kg; tens of measurements per day can be accomplished with a 2-σ uncertainty in the order of 15%. The principal tests performed with the thrust stand are:

- Characterization of the mechanical response of the stand. Preliminary tests highlighted that the sensibility of the instrument is almost inverse proportional to the reduced mass of the system (see Eq. 4.6). In addition, the sensibility influences both the range of linearity and the level of noise: the latter increases as the sensibility does so, while the former decreases.

- Verification of the accuracy and the reliability of the measurements. As the other pendulum-based thrust stands, also the counterbalanced pendulum is susceptible to zero-position drift. In order to properly evaluate the thrust, this effect has been corrected in post-processing with a procedure that introduces an uncertainty in the order of 15%. In addition, the measurements of the stand have been benchmarked against the results of a Faraday probe [66]: the two estimations agree within 20%.

- Exploitation of the thrust stand to test a medium power (200-300 W) HPT operated with xenon and carbon dioxide. The thrust increases as both the mass flow rate and the input power does so, and the specific impulse is a linear function of the input power. On the contrary, the relation between the specific impulse and the mass flow rate is propellant gas dependent. In general, the xenon propellant presents far better propulsive performances than the carbon dioxide, namely thrust four times higher for the same operative conditions.

It is worth highlighting that during the test campaign the stand has been proven to be a robust instrument in a wide range of operational conditions. Moreover, the good accuracy of the measurements (up to 15%) and the possibility of accomplishing tens of tests per day have been confirmed.

In conclusion, a combined numerical-experimental campaign has been conducted on a non-optimized low power (50 W range) prototype operated with Ar propellant in order to evaluate the reliability of the HPT code when dealing with real-life thrusters.

- A good qualitative agreement has been found between numerical and experimental results provided that the code has correctly predicted that (i) both thrust and specific impulse are linear functions of the input power, (ii) the thrust increases with the mass flow rate, and (iii) the specific impulse is inverse proportional to the mass flow rate.

- A satisfactory qualitative agreement has been found, provided that the maximum mismatching between measurements and numerical previsions is in the order of 40%.

Nonetheless, higher agreement between numerical and experimental data was not expected provided the very simplified plume model adopted. Finally, the HPT numerical model predicts lower thruster performances in respect to the measured values, therefore it provides conservative data.

6.2 Future work

The satisfactory agreement between the numerical results and experimental measurements have confirmed that the HPT numerical code is a sufficiently reliable instrument to deal with real-life prototypes. Nonetheless, it is particularly unlikely that a HPT propelled with argon is suitable for space applications. In a real space mission the adoption of xenon is the most probable solution. Therefore, the next step will be enabling the code to study HPTs propelled by Xe. Subsequently, a combined numerical-experimental campaign will be conducted in order to optimize the discharge chamber of Xe-based HPTs (i.e., potentially usable in real space missions). Moreover, in the last years many feasibility studies have been conducted on the adoption of exotic propellants, such as Iodine, for Electric Thrusters [127]. In particular, the University of Padova in collaboration with T4i Srl is getting involved into this field of research; therefore a further step will be upgrading the HPT model to handle Iodine plasmas.

Nevertheless, more work is needed to properly predict the thruster performances. The model adopted for the plasma accelleration must be improved in order to obtain more

reliable results. Provided that in the plume the distribution function of the charged particles can significantly depart from the Maxwellian (e.g., because of the presence of a Double Layer [62, 63]), and that the plasma density is order of magnitudes lower than in the plasma source [40], a PIC strategy seems the best option to obtain accurate data with reasonable computing time. The numerical code F3MPIC [128] seems a good candidate to describe the plasma plume, in fact it is a PIC code coupled with a finite element electrostatic solver which has been validated and widely employed during the HPH.COM project [9]. Once the 3D-VIRTUS and the F3MPIC code will be integrated, the new tool will be adopted to optimize the overall thruster, namely both *Production Stage* and *Acceleration Stage*.

6.3 Novelty

Finally, it is worth highlighting the innovative contributions made by this research work:

- The development of the 3D-VIRTUS code. It is one of the very few self-consistent (i.e., which resolves both the EM wave propagation and plasma transport) numerical tools which can handle Helicon sources. In particular it is the only which can (i) treat discharges with a generic 3D geometry, and (ii) model the actual RF antenna, solving the current distribution thereof. In addition, the code can resolve generic plasma sources driven by RF antennas (e.g., ICPs and CCPs [29]) if all the plasma species can be considered Maxwellian. Furthermore, the FLUID module stand-alone can also simulate DC discharges [29], provided that the Maxwellianity hypothesis is respected. Thanks to its versatility, the code has been exploited also for studying plasma discharges adopted in Gaseous Plasma Antennas (GPAs) [129].

- The development of the HPT numerical code. Even though the plasma plume is studied with a very simplified model, the numerical results show a satisfactory agreement with experimental data. Moreove, this code is the only one in literature which predicts the performances of HPTs relying on an accurate tool for the plasma source simulation.

- The characterization and exploitation of the counterbalanced pendulum thrust stand for evaluating HPTs performances. This compact and low-cost instrument is perfectly suited for testing generic HPTs, in fact it is robust against RF disturbances (2-σ uncertainty of 15%) and can handle a wide range of thrusters, both in term of force produced and mass. Moreover, this stand has been successfully exploited also to test other RF driven Electric Thrusters, such as RIT [121] and cathodeless [122].

- The parametric analysis reported in Chap. 3. In literature, no similar analyses on both Helicon discharges and HPTs (i.e., wide ranges of design parameters scanned relying on an accurate tool for the discharge chamber modelling) are available.

Bibliography

[1] R. G. Jahn, Physics of electric propulsion, Dover Publications, Inc., Mineola NY, USA, 2006.

[2] R. W. Humble, G. N. Henry, W. J. Larson, *et al.*, Space propulsion analysis and design, McGraw-Hill, New York NY, USA, 1995.

[3] W. J. Larson, J. R. Wertz, Space Mission Analysis and Design, 3rd Edition, Microcosm, Inc., El Segundo CA, USA, 1999.

[4] M. Martinez-Sanchez, J. E. Pollard, Spacecraft electric propulsion-an overview, Journal of propulsion and power 14 (5) (1998) 688–699.

[5] R. G. Jahn, E. Y. Choueiri, Electric propulsion, http://alfven.princeton.edu/publications/ep-encyclopedia-2001, accessed: 2018-09-19.

[6] List of spacecraft with electric propulsion, https://en.wikipedia.org/wiki/List_of_spacecraft_with_electric_propulsion, accessed: 2018-09-19.

[7] D. M. Goebel, I. Katz, Fundamentals of electric propulsion: Ion and Hall thrusters, JPL Space Science & Technology Series, 2008.

[8] R. J. Cybulski, D. M. Shellhammer, R. R. Lovell, E. J. Domino, J. T. Kotnik, J. Cybulski, R. R. Loveli, Results from SERT I Ion Rocket Flight Test, Tech. Rep. D-2718, NASA (1965).

[9] D. Pavarin, F. Ferri, M. Manente, D. Rondini, D. Curreli, Y. Guclu, M. Melazzi, S. Suman, G. Bianchini, Helicon Plasma Hydrazine: COmbined Micro project overview and development status, in: Proceedings of the 2^{nd} Space Propulsion Conference, no. SP2010-1842379, San Sebastian, ES, 2010.

[10] F. F. Chen, Helicon discharges and sources: a review, Plasma Sources Science and Technology 24 (1) (2015) 014001.

[11] E. Ahedo, M. Merino, Two-dimensional supersonic plasma acceleration in a magnetic nozzle, Physics of Plasmas 17 (7) (2010) 073501.

[12] F. F. Chen, D. Arnush, Generalized theory of helicon waves. i. normal modes, Physics of Plasmas 4 (9) (1997) 3411–3421.

[13] F. F. Chen, Helicon plasma sources, http://www.seas.ucla.edu/~ffchen/Publs/Chen155R.pdf, accessed: 2018-09-19.

[14] F. Trezzolani, M. Manente, A. Selmo, D. Melazzi, M. Magarotto, D. Moretto, P. De Carlo, M. Pessana, D. Pavarin, Development and test of an high power RF plasma thruster in project SAPERE-STRONG, in: 35^{th} International Electric Propulsion Conference, no. IEPC-2017-462, Atlanta GA, USA, 2017.

[15] F. Trezzolani, M. Manente, E. Toson, A. Selmo, M. Magarotto, D. Moretto, F. Bosi, P. De Carlo, D. Melazzi, D. Pavarin, Development and testing of a miniature helicon plasma thruster, in: 35^{th} International Electric Propulsion Conference, no. IEPC-2017-519, Atlanta GA, USA, 2017.

[16] F. R. C. Diaz, The VASIMR rocket, Scientific American 283 (5) (2000) 90–97.

[17] B. W. Longmier, J. P. Squire, L. D. Cassady, M. G. Ballenger, M. D. Carter, C. Olsen, A. V. Ilin, T. W. Glover, G. E. McCaskill, F. C. Dıaz, et al., Vasimr vx-200 performance measurements and helicon throttle tables using argon and krypton, in: 32^{nd} International Electric Propulsion Conference, no. IEPC-2011-156, Wiesbaden, DE, 2011.

[18] R. W. Boswell, C. Charles, The helicon double layer thruster, in: 28^{th} International Electric Propulsion Conference, no. IEPC-2003-332, Toulouse, FR, 2003.

[19] K. Takahashi, T. Lafleur, C. Charles, P. Alexander, R. Boswell, M. Perren, R. Laine, S. Pottinger, V. Lappas, T. Harle, et al., Direct thrust measurement of a permanent magnet helicon double layer thruster, Applied Physics Letters 98 (14) (2011) 141503.

[20] S. Pottinger, V. Lappas, C. Charles, R. Boswell, Performance characterization of a helicon double layer thruster using direct thrust measurements, Journal of Physics D: Applied Physics 44 (23) (2011) 235201.

[21] Technology for propulsion and innovation official web site, http://www.t4innovation.com/, accessed: 2018-09-19.

[22] M. Merino, J. Navarro, S. Casado, E. Ahedo, V. Gómez, M. Ruiz, E. Bosch, J. G. del Amo, Design and development of a 1 kw-class helicon antenna thruster, in: 34^{th} International Electric Propulsion Conference, no. IEPC-2015-297, Kobe, J, 2015.

[23] S. Shinohara, H. Nishida, T. Tanikawa, T. Hada, I. Funaki, K. P. Shamrai, Development of electrodeless plasma thrusters with high-density helicon plasma sources, IEEE Transactions on Plasma Science 42 (5) (2014) 1245–1254.

[24] D. Kuwahara, Y. Koyama, S. Otsuka, T. Ishii, H. Ishii, H. Fujitsuka, S. Waseda, S. Shinohara, Development of direct thrust measurement system for the completely electrodeless helicon plasma thruster, Plasma and Fusion Research 9 (2014) 3406025.

[25] K. Takahashi, A. Komuro, A. Ando, Effect of source diameter on helicon plasma thruster performance and its high power operation, Plasma Sources Science and Technology 24 (5) (2015) 055004.

[26] O. V. Batishchev, Minihelicon plasma thruster, IEEE Transactions on plasma science 37 (8) (2009) 1563–1571.

[27] J. P. Sheehan, T. A. Collard, F. H. Ebersohn, B. W. Longmier, Initial operation of the cubesat ambipolar thruster, in: 34^{th} International Electric Propulsion Conference, no. IEPC-2015-243, Kobe, J, 2015.

[28] T. Ziemba, J. Carscadden, J. Slough, J. Prager, R. Winglee, High power helicon thruster, in: 41^{st} AIAA/ASME/SAE/ASEE Joint Propulsion Conference & Exhibit, no. AIAA 2005-4119, Tucson AZ, USA, 2005.

[29] M. A. Lieberman, A. J. Lichtenberg, Principles of plasma discharges and materials processing, John Wiley & Sons, Inc., Hoboken NJ, USA, 2005.

[30] D. Melazzi, D. Curreli, M. Manente, J. Carlsson, D. Pavarin, SPIREs: A Finite-Difference Frequency-Domain electromagnetic solver for inhomogeneous magnetized plasma cylinders, Computer Physics Communications 183 (6) (2012) 1182–1191.

[31] J. A. Lehane, P. C. Thonemann, An experimental study of helicon wave propagation in a gaseous plasma, Proceedings of the Physical Society 85 (2) (1965) 301–316.

[32] R. W. Boswell, Very efficient plasma generation by whistler waves near the lower hybrid frequency, Plasma Physics and Controlled Fusion 26 (10) (1984) 1147–1162.

[33] F. F. Chen, R. W. Boswell, Helicons-the past decade, IEEE Transactions on Plasma Science 25 (6) (1997) 1245–1257.

[34] I. Tepermeister, N. Blayo, F. Klemens, D. Ibbotson, R. Gottscho, J. Lee, H. Sawin, Comparison of advanced plasma sources for etching applications. I. Etching rate, uniformity, and profile control in a helicon and a multiple electron cyclotron resonance source, Journal of Vacuum Science & Technology B: Microelectronics and Nanometer Structures Processing, Measurement, and Phenomena 12 (4) (1994) 2310–2321.

[35] R. H. Goulding, J. B. O. Caughman, J. Rapp, T. M. Biewer, T. S. Bigelow, I. H. Campbell, J. F. Caneses, D. Donovan, N. Kafle, E. H. Martin, H. B. Ray, G. C. Shaw, M. A. Showers, Progress in the development of a high power helicon plasma source for the materials plasma exposure experiment, Fusion Science and Technology 72 (4) (2017) 588–594.

[36] A. J. Perry, D. Vender, R. W. Boswell, The application of the helicon source to plasma processing, Journal of Vacuum Science and Technology B, Nanotechnology and Microelectronics: Materials, Processing, Measurement, and Phenomena 9 (2) (1991) 310–317.

[37] F. F. Chen, Introduction to plasma physics and controlled fusion, 2nd Edition, Vol. 1: Plasma Physics, Plenum Press, New York NY, USA, 1984.

[38] M. D. Carter, F. W. Baity Jr., G. C. Barber, R. H. Goulding, Y. Mori, D. O. Sparks, K. F. White, E. F. Jaeger, F. R. Chang-Diaz, J. P. Squire, Comparing experiments

with modeling for light ion helicon plasma sources, Physics of Plasmas 9 (12) (2002) 5097–5110.

[39] A. Cardinali, D. Melazzi, M. Manente, D. Pavarin, Ray-tracing wkb analysis of whistler waves in non-uniform magnetic fields applied to space thrusters, Plasma Sources Science and Technology 23 (1) (2014) 015013.

[40] F. Cichocki, A. Domínguez-Vázquez, M. Merino, E. Ahedo, Hybrid 3d model for the interaction of plasma thruster plumes with nearby objects, Plasma Sources Science and Technology 26 (12) (2017) 125008.

[41] M. Merino, F. Cichocki, E. Ahedo, A collisionless plasma thruster plume expansion model, Plasma Sources Science and Technology 24 (3) (2015) 035006.

[42] T. Lafleur, Helicon plasma thruster discharge model, Physics of Plasmas 21 (4) (2014) 043507.

[43] E. Ahedo, J. Navarro-Cavallé, Helicon thruster plasma modeling: Two-dimensional fluid-dynamics and propulsive performances, Physics of Plasmas 20 (4) (2013) 043512.

[44] A. Fruchtman, K. Takahashi, C. Charles, R. Boswell, A magnetic nozzle calculation of the force on a plasma, Physics of Plasmas 19 (3) (2012) 033507.

[45] A. R. Choudhuri, The physics of fluids and plasmas: an introduction for astrophysicists, Cambridge University Press, Cambridge, UK, 1998.

[46] J. Van Dijk, G. Kroesen, A. Bogaerts, Plasma modelling and numerical simulation, Journal of Physics D: Applied Physics 42 (19) (2009) 190301.

[47] G. Hagelaar, L. Pitchford, Solving the boltzmann equation to obtain electron transport coefficients and rate coefficients for fluid models, Plasma Sources Science and Technology 14 (4) (2005) 722–733.

[48] M. Martinez-Sanchez, J. Navarro-Cavallé, E. Ahedo, Electron cooling and finite potential drop in a magnetized plasma expansion, Physics of Plasmas 22 (5) (2015) 053501.

[49] C. K. Birdsall, A. B. Langdon, Plasma physics via computer simulation, Tylor & Francis Group, New York NY, USA, 2005.

[50] G. Chen, A self-consistent model of helicon discharge, PhD thesis, The University of Texas at Austin (2008).

[51] Y. Mouzouris, J. E. Scharer, Modeling of profile effects for inductive helicon plasma sources, IEEE Transactions on Plasma Science 24 (1) (1996) 152–160.

[52] D. Melazzi, D. Curreli, M. Manente, J. Carlsson, D. Pavarin, SPIREs: A finite-difference frequency-domain electromagnetic solver for inhomogeneous magnetized plasma cylinders, Computer Physics Communication 183 (6) (2012) 1182–1191.

[53] D. Melazzi, V. Lancellotti, ADAMANT: A surface and volume integral-equation solver for the analysis and design of helicon plasma sources, Computer Physics Communications 185 (7) (2014) 1914–1925.

[54] D. Arnush, The role of Trivelpiece - Gould waves in antenna coupling to helicon waves, Physics of Plasmas 7 (7) (2000) 3042–3050.

[55] A. Cardinali, F. Santini, Lower hybrid penetration across a steep density gradient, Plasma Physics and Controlled Fusion 53 (12) (2011) 125001.

[56] S. Cho, M. Lieberman, Self-consistent discharge characteristics of collisional helicon plasmas, Physics of Plasmas 10 (3) (2003) 882–890.

[57] R. L. Kinder, M. J. Kushner, Wave propagation and power deposition in magnetically enhanced inductively coupled and helicon plasma sources, Journal of Vacuum Science & Technology A: Vacuum, Surfaces, and Films 19 (1) (2001) 76–86.

[58] R. L. Kinder, M. J. Kushner, Noncollisional heating and electron energy distributions in magnetically enhanced inductively coupled and helicon plasma sources, Journal of Applied Physics 90 (8) (2001) 3699–3712.

[59] D. Bose, T. Govindan, M. Meyyappan, Modeling of a helicon plasma source, IEEE transactions on plasma science 31 (4) (2003) 464–470.

[60] M. Manente, J. Carlsson, I. Musso, C. Bramanti, D. Pavarin, F. Angrilli, Numerical simulation of the helicon double layer thruster concept, in: 43^{rd} AIAA/ASME/SAE/ASEE Joint Propulsion Conference & Exhibit, no. AIAA 2007-5312, Cincinnati, OH, 2007.

[61] J. Carlsson, M. Manente, D. Pavarin, Implicitly charge-conserving solver for Boltzmann electrons, Physics of Plasmas 16 (6) (2009) 062310.

[62] M. Merino, E. Ahedo, Two-dimensional quasi-double-layers in two-electron-temperature, current-free plasmas, Physics of Plasmas 20 (2) (2013) 023502.

[63] N. Singh, Current-free double layers: A review, Physics of plasmas 18 (12) (2011) 122105.

[64] K. L. Brown, G. W. Tautfest, Faraday-Cup monitors for high-energy electron beams, Review of Scientific Instruments 27 (9) (1956) 696–702.

[65] C. Enloe, High-resolution retarding potential analyzer, Review of scientific instruments 65 (2) (1994) 507–508.

[66] F. Trezzolani, Optimization and automatic control of radio-frequency plasma thrusters for space applications, PhD thesis, Università degli studi di Padova (2015).

[67] F. F. Chen, Langmuir probe diagnostics, http://www.seas.ucla.edu/~ffchen/Publs/Chen210R.pdf, accessed: 2018-09-19.

[68] K. D. Diamant, J. E. Pollard, M. W. Crofton, M. J. Patterson, G. C. Soulas, Thrust stand characterization of the NASA evolutionary xenon thruster, Journal of Propulsion and Power 27 (4) (2011) 777–785.

[69] A. Wang, H. Wu, H. Tang, Y. Liu, X. Liang, Development and testing of a new thrust stand for micro-thrust measurement in vacuum conditions, Vacuum 91 (2013) 35–40.

[70] A. V. Loyan, T. A. Maksymenko, Performance investigation of SPT-20M low power hall effect thruster, in: 30^{th} International Electric Propulsion Conference, no. IEPC-2007-100, Firenze, IT, 2007.

[71] K. A. Polzin, T. E. Markusic, B. J. Stanojev, A. DeHoyos, B. Spaun, Thrust stand for electric propulsion performance evaluation, Review of Scientific Instruments 77 (10) (2006) 105108.

[72] N. Nagao, S. Yokota, K. Komurasaki, Y. Arakawa, Development of a two-dimensional dual pendulum thrust stand for hall thrusters, Review of Scientific Instruments 78 (11) (2007) 115108.

[73] K. G. Xu, M. L. Walker, High-power, null-type, inverted pendulum thrust stand, Review of Scientific Instruments 80 (5) (2009) 055103.

[74] A. Knoll, D. Lamprou, V. Lappas, M. Pollard, P. Bianco, Thrust balance characterization of a 200 w quad confinement thruster for high thrust regimes, IEEE Transactions on Plasma Science 43 (1) (2015) 185–189.

[75] A. D. Kodys, R. Murray, L. Cassady, E. Y. Choueiri, An inverted-pendulum thrust stand for high-power electric thrusters, in: 42^{nd} AIAA/ASME/SAE/ASEE Joint Propulsion Conference & Exibit, no. AIAA 2016-4821, Sacramento CA, USA, 2006.

[76] Z. He, J. Wu, D. Zhang, G. Lu, Z. Liu, R. Zhang, Precision electromagnetic calibration technique for micro-newton thrust stands, Review of Scientific Instruments 84 (5) (2013) 055107.

[77] T. W. Haag, Thrust stand for pulsed plasma thrusters, Review of Scientific Instruments 68 (5) (1997) 2060–2067.

[78] H. Koizumi, K. Komurasaki, Y. Arakawa, Development of thrust stand for low impulse measurement from microthrusters, Review of scientific instruments 75 (10) (2004) 3185–3190.

[79] J. K. Ziemer, Performance measurements using a sub-micronewton resolution thrust stand, in: 27^{th} International Electric Propulsion Conference, no. IEPC-2001-238, Pasadena CA, USA, 2001.

[80] S. Rocca, Onera micronewton thrust balance: Analytical modelling and parametric analysis, Aerospace Science and Technology 15 (2) (2011) 148–154.

[81] E. Canuto, A. Rolino, Nanobalance: An automated interferometric balance for micro-thrust measurement, ISA transactions 43 (2) (2004) 169–187.

[82] A. J. Jamison, A. D. Ketsdever, E. Muntz, Gas dynamic calibration of a nano-newton thrust stand, Review of Scientific Instruments 73 (10) (2002) 3629–3637.

[83] A. Acosta-Zamora, J. R. Flores, A. Choudhuri, Torsional thrust balance measurement system development for testing reaction control thrusters, Measurement 46 (9) (2013) 3414–3428.

[84] S. Banetta, R. Falorni, L. Biagioni, G. Saccoccia, Development of a two-axes thrust stand for electric thrusters, in: 4^{th} International Spacecraft Propulsion Conference, Cagliari, IT, 2004.

[85] A. Grubisic, S. Gabriel, Development of an indirect measurement Micro-to-Milli-Newton thrust balance, in: 2^{nd} International Symposium on Propulsion for Space Transportation, Heraklion, GR, 2008.

[86] S. Ciaralli, M. Coletti, S. Gabriel, An impulsive thrust balance for applications of micro-pulsed plasma thrusters, Measurement Science and Technology 24 (11) (2013) 115003.

[87] J. G. del Amo, G. Saccoccia, P. E. Frigot, ESA propulsion lab at ESTEC, in: 31^{st} International Electric Propulsion Conference, no. IEPC-2009-236, Ann Arbor MI, USA, 2009.

[88] M. Magarotto, M. Manente, P. de Carlo, F. Trezzolani, D. Pavarin, D. Melazzi, Numerical model of the plasma source of an helicon plasma thruster, in: 6^{th} Space Propulsion Conference, no. SP2018-424, Seville, ES, 2018.

[89] F. Trezzolani, M. Magarotto, M. Manente, D. Pavarin, Development of a counter-balanced pendulum thrust stand for electric propulsion, Measurement 122 (2018) 494–501.

[90] H. G. Weller, G. Tabor, H. Jasak, C. Fureby, A tensorial approach to computational continuum mechanics using object-oriented techniques, Computers in physics 12 (6) (1998) 620–631.

[91] D. Pavarin, F. Ferri, M. Manente, A. Lucca Fabris, F. Trezzolani, M. Faenza, L. Tasinato, O. Tudisco, A. Loyan, Y. Protsan, *et al.*, Thruster development set-up for the Helicon Plasma Hydrazine COmbined Micro research project, in: 32^{nd} International Electric Propulsion Conference, no. IEPC-2011-241, Wiesbaden, DE, 2011.

[92] F. Trezzolani, F. J. Bosi, D. Melazzi, P. de Carlo, A. Selmo, M. Manente, S. Ferraris, M. Pessana, D. Pavarin, Experimental characterization of a kW-level radio-frequency plasma thruster for project SAPERE-STRONG, in: 5^{th} Space Propulsion Conference, no. SP2016-3125244, Roma, IT, 2016.

[93] T. Lafleur, C. Charles, R. W. Boswell, Characterization of a helicon plasma source in low diverging magnetic fields, Journal of Physics D: Applied Physics 44 (5) (2011) 055202.

[94] F. F. Chen, D. D. Blackwell, Upper limit to landau damping in helicon discharges, Physical review letters 82 (13) (1999) 2677–2680.

[95] M. M. Balkey, R. Boivin, J. L. Kline, E. E. Scime, Ion heating and density production in helicon sources near the lower hybrid frequency, Plasma Sources Science and Technology 10 (2) (2001) 284–294.

[96] J. Kline, E. Scime, Parametric decay instabilities in the helix helicon plasma source, Physics of Plasmas 10 (1) (2003) 135–144.

[97] I. D. Sudit, F. F. Chen, Discharge equilibrium of a helicon plasma, Plasma Sources Science and Technology 5 (1) (1996) 43–53.

[98] A. Fiala, L. C. Pitchford, J. P. Boeuf, Two-dimensional, hybrid model of low-pressure glow discharges, Physical Review E 49 (6) (1994) 5607–5622.

[99] G. Chen, L. L. Raja, Fluid modeling of electron heating in low-pressure, high-frequency capacitively coupled plasma discharges, Journal of Applied Physics 96 (11) (2004) 6073–6081.

[100] I. G. Mikellides, I. Katz, D. M. Goebel, J. E. Polk, Hollow cathode theory and experiment. ii. a two-dimensional theoretical model of the emitter region, Journal of Applied Physics 98 (11) (2005) 113303.

[101] J. Bukowski, D. Graves, P. Vitello, Two-dimensional fluid model of an inductively coupled plasma with comparison to experimental spatial profiles, Journal of Applied Physics 80 (5) (1996) 2614–2623.

[102] J. T. Gudmundsson, Notes on the electron excitation rate coefficients for argon and oxigen discharge, Tech. Rep. RH-21-2002, Science Institute Univesity of Iceland (2002).

[103] M. J. Kushner, Modeling of magnetically enhanced capacitively coupled plasma sources: Ar discharges, Journal of applied physics 94 (3) (2003) 1436–1447.

[104] R. S. Brokaw, Predicting transport properties of dilute gases, Industrial & Engineering Chemistry Process Design and Development 8 (2) (1969) 240–253.

[105] P. D. Neufeld, A. Janzen, R. Aziz, Empirical equations to calculate 16 of the transport collision integrals ω (l, s)* for the Lennard-Jones (12–6) potential, The Journal of Chemical Physics 57 (3) (1972) 1100–1102.

[106] G. Hagelaar, F. De Hoog, G. Kroesen, Boundary conditions in fluid models of gas discharges, Physical Review E 62 (1) (2000) 1452–1454.

[107] G. Hagelaar, G. Kroesen, Speeding up fluid models for gas discharges by implicit treatment of the electron energy source term, Journal of Computational Physics 159 (1) (2000) 1–12.

[108] M. Abdollahzadeh, J. C. Pascoa, P. J. Oliveira, Implementation of the classical plasma–fluid model for simulation of dielectric barrier discharge (DBD) actuators in OpenFOAM, Computers & Fluids 128 (2016) 77–90.

[109] F. Moukalled, L. Mangani, M. Darwish, *et al.*, The finite volume method in computational fluid dynamics, Springer, Cham, DE, 2016.

[110] OpenFOAM official website, https://www.openfoam.com/, accessed: 2018-09-19.

[111] Official COMSOL website, https://www.comsol.it/, accessed: 2018-09-19.

[112] Y. Coudière, C. Pierre, Stability and convergence of a finite volume method for two systems of reaction-diffusion equations in electro-cardiology, Nonlinear analysis: real world applications 7 (4) (2006) 916–935.

[113] T. H. Stix, The theory of plasma waves, McGraw-Hill, New York NY, USA, 1962.

[114] C. Charles, R. Boswell, M. Lieberman, Energy balance in a low pressure capacitive discharge driven by a double-saddle antenna, physics of plasmas 10 (3) (2003) 891–899.

[115] D. J. Griffiths, Introduction to electrodynamics, 4th Edition, Pearson Education, Ltd., Harlow, UK, 2005.

[116] D. G. Miljak, F. F. Chen, Helicon wave excitation with rotating antenna fields, Plasma Sources Science and Technology 7 (1) (1998) 61–74.

[117] D. Melazzi, V. Lancellotti, A comparative study of radiofrequency antennas for helicon plasma sources, Plasma Sources Science and Technology 24 (2015) 025024.

[118] S. M. Tysk, C. M. Denning, J. E. Scharer, K. Akhtar, Optical, wave measurements, and modeling of helicon plasmas for a wide range of magnetic fields, Physics of Plasmas 11 (3) (2004) 878–887.

[119] D. G. Miljak, F. F. Chen, Density limit in helicon discharges, Plasma Sources Science and Technology 7 (4) (1998) 537–549.

[120] M. Krämer, B. Lorenz, B. Clarenbach, Helicon sources with m= 1 and m= 2 helical antenna coupling, Plasma Sources Science and Technology 11 (3A) (2002) A120–A130.

[121] H. J. Leiter, R. Killinger, H. Bassner, J. Müller, R. Kukies, Development of the radio frequeny ion thruster RIT XT – A status report, in: 27^{th} International Electric Propulsion Conferce, no. IEPC-2001-104, Pasadena CA, USA, 2001.

[122] F. Cannat, T. Lafleur, J. Jarrige, P. Chabert, P. Q. Elias, D. Packan, Optimization of a coaxial electron cyclotron resonance plasma thruster with an analytical model, Physics of Plasmas 22 (5) (2015) 053503.

[123] ISO/IEC GUIDE 98-3:2008(E) (GUM,1995), https://www.iso.org/standard/50461.html, accessed: 2018-09-19.

[124] J. Jarrige, P. Thobois, C. Blanchard, P.-Q. Elias, D. Packan, L. Fallerini, G. Noci, Thrust measurements of the gaia mission flight-model cold gas thrusters, Journal of Propulsion and Power 30 (4) (2014) 934–943.

[125] S-helicon antenna, international PCT/IB2016/050199 15.01.2016, Italian patent number VR2015A000007 del 16.01.2015.

[126] Peek material properties, https://www.curbellplastics.com/Research-Solutions/Materials/PEEK, accessed: 2018-09-19.

[127] K. A. Polzin, J. F. Seixal, S. L. Mauro, A. O. Burt, A. Martinez, A. K. Matin, The iodine satellite (isat) propellant feed system - design and development, in: 35^{th} International Electric Propulsion Conference, no. IEPC-2017-11, Atlanta GA, USA, 2017.

[128] D. Pavarin, F. Ferri, M. Manente, D. Curreli, D. Melazzi, D. Rondini, A. Cardinali, Development of plasma codes for the design of mini-helicon thrusters, in: 32^{nd} International Electric Propulsion Conference, no. IEPC-2011-240, Weisbaden, DE, 2011.

[129] D. Melazzi, P. De Carlo, F. Trezzolani, V. Lancellotti, M. Manente, D. Pavarin, F. Rigobello, A.-D. Capobianco, First experimental characterization of a gaseous plasma antenna in the uhf band, in: Antennas and Propagation (EUCAP), 2017 11th European Conference on, IEEE, 2017, pp. 3213–3217.